HAL
open science

New exotic nanostructured materials : Theoretical predictions and experimental verifications

Fatme Jardali

To cite this version:

Fatme Jardali. New exotic nanostructured materials : Theoretical predictions and experimental verifications. Materials Science [cond-mat.mtrl-sci]. Université Paris Saclay (COmUE), 2017. English. NNT : 2017SACLX022 . tel-02303039

HAL Id: tel-02303039

https://pastel.hal.science/tel-02303039v2

Submitted on 2 Oct 2019

HAL is a multi-disciplinary open access archive for the deposit and dissemination of scientific research documents, whether they are published or not. The documents may come from teaching and research institutions in France or abroad, or from public or private research centers.

L'archive ouverte pluridisciplinaire **HAL**, est destinée au dépôt et à la diffusion de documents scientifiques de niveau recherche, publiés ou non, émanant des établissements d'enseignement et de recherche français ou étrangers, des laboratoires publics ou privés.

NNT : 2017SACLX022

Thèse de doctorat de l'Université Paris-Saclay préparée à l'Ecole Polytechnique

Ecole doctorale n°573
Interfaces : approches interdisciplinaires, fondements, applications et innovation
Spécialité de doctorat : Physique
par

Mlle. Fatme Jardali

Nouveaux matériaux exotiques nanostructurés : Prévisions théoriques et vérifications expérimentales

Thèse présentée et soutenue à "Palaiseau", le 10 Mai 2017.

Composition du Jury :

M.	Philippe BARANEK	Ingénieur de Recherche EDF R&D-IRDEP	(Président)
M.	Thierry BELMONTE	Directeur de Recherche Université Lorraine	(Rapporteur)
M.	Laifa BOUFENDI	Professeur Université Orléans	(Rapporteur)
Mme.	Claudine CRÉPIN-GILBERT	Directrice de Recherche Université Paris-Sud 11	(Examinatrice)
M.	Khaled HASSOUNI	Professeur Université Paris 13	(Examinateur)
M.	Gilles H. PESLHERBE	Professeur Université Concordia	(Examinateur)
M.	Holger VACH	Directeur de Recherche Ecole Polytechnique	(Directeur de thèse)

Abstract

This thesis is devoted to the study of advanced, exotic forms of nanostructured materials that could lead to the next big advance for nanodevices. Two distinct topics have been considered. The first one is related to plasma-born aromatic silicon nanoclusters (SiNCs), while the second is dedicated to two-dimensional silicon and germanium materials. Based on molecular dynamics simulations and *ab initio* calculations, as well as, on experimental investigations, we explore a variety of intriguing properties of those exotic materials that are expected to be far superior to those of their conventional counterparts.

In the first part of the thesis, we begin with theoretical studies and show that it is possible to obtain aromatic behavior in simple hydrogenated SiNCs with size of ∼1nm. We demonstrate that low-temperature silane/hydrogen plasmas close to dust formation present the ideal environment to exploit the natural tendency of silicon to over-coordination for the construction of structures with electron-deficient bonds. Those nanoclusters form spontaneously by self-assembly in plasmas, do not possess tetrahedral structures, are more stable than any other known SiNCs of this size, and have strong aromatic-like properties due to their high electron delocalization. We demonstrate that non-tetrahedral SiNCs exhibit metallic-like bonding schemes that strongly resemble the one of a homogeneous electron gas in small metal clusters. Standard tetrahedral SiNCs of this size can absorb light only in the ultraviolet, while our calculations have shown that pure, but over-coordinated SiNCs absorb light in the ultraviolet, visible, and infrared spectral region. In this thesis, we present first experimental evidence that supports our theoretical predictions. Using incoherent broadband cavity enhanced absorption spectroscopy, we have measured the absorption of SiNCs, *in situ*, in a plasma reactor and found that they do absorb light in the visible region. In addition, our absorption measurements in the presence of an applied electric field have provided clear evidence that aromatic SiNCs possess a permanent dipole moment, and we have measured it to be between 2.0 and 2.5 Debye, in excellent agreement to prior *ab initio* calculations. Finally, our transmission electron microscopy images of such SiNCs, after their deposition under optimized plasma conditions, have revealed the presence of another exotic form of silicon with a primitive hexagonal structure. Such a structure usually forms after exposing diamond-cubic silicon to extremely high pressures. We tentatively claim that those conditions were, actually, achieved in our experiments due to the "chemistry with a hammer".

In the second part of the thesis, we have undertaken in-depth theoretical and experimental studies on the growth of a new allotropic form of silicon and germanium: a single layer of silicon or germanium atoms, only one atom thick and packed in a hexagonal lattice that closely resembles the lattice of graphene, namely silicene and germanene. In order to rule out any intermixing between silicon or germanium atoms and the underneath substrate atoms, as it was the case for metallic substrates, and to maintain their promising features to be new Dirac materials, we have performed our depositions on a chemically inert graphite substrate. One of our crucial findings is that the silicene or germanene monolayers interact with the graphite substrate via van der Waals forces only. The van der Waals interaction is strong enough to stabilize the deposited monolayers even above room temperature, but weak enough to prevent any hybridization or alloying between silicon or germanium and carbon atoms. Consequently, the outstanding electronic properties of free-standing silicene and germanene, such as Dirac cones and massless electrons, are preserved even after their deposition on graphite surfaces.

Résumé

Cette thèse est consacrée à l'étude approfondie de formes exotiques de matériaux nano-structurés qui pourraient conduire à une avancée significative dans les nano-composants. Deux thèmes distincts ont été ainsi abordés. Le premier concerne les nano-clusters aromatiques de silicium synthétisés par plasma (SiNCs), tandis que le second est dédié aux structures silicium et germanium bi-dimensionnelles. Grâce à des simulations de type dynamique moléculaire et des calculs *ab initio*, ainsi que sur des recherches expérimentales, nous nous proposons d'explorer les propriétés intrigantes, mais à fort potentiel, de ces matériaux exotiques.

Dans la première partie, nous commençons par des études théoriques et montrons qu'il est possible d'obtenir un comportement aromatique pour des SiNCs hydrogénés ayant une taille de ∼1nm. Nous démontrons que les plasmas silane/hydrogène à basse température, proches de la formation de particules de poussière, présentent l'environnement idéal pour exploiter la tendance naturelle du silicium à la sur-coordination et donc pour la synthèse de structures à liaisons déficitaires en électrons. Ces nano-clusters qui se forment spontanément par auto-assemblage dans le plasma, ne possèdent pas de structure tétraédrique, sont plus stables que tous les autres SiNCs connus de cette taille et ont de fortes propriétés aromatiques dues à leur forte délocalisation électronique. Nous montrons également que les SiNCs non tétraédriques présentent des modes de liaison à caractère métallique qui ressemblent fortement à celui d'un gaz d'électrons homogène dans des nano-clusters de métaux. Les SiNCs tétraédriques standards de cette taille ne peuvent absorber que dans l'ultraviolet, alors que nos calculs ont montré que des SiNCs purs, mais sur-coordonnés, absorbent dans la région spectrale ultraviolette, mais aussi dans le visible et l'infrarouge. Nous présentons ensuite une première preuve expérimentale pour nos prédictions théoriques. Nous avons mesuré *in situ*, dans un réacteur plasma l'absorption de la lumière visible des SiNCs. De plus, nos mesures réalisées en présence d'un champ électrique ont prouvées clairement que les SiNCs aromatiques possèdent un moment dipolaire permanent, que nous avons estimé entre 2,0 et 2,5 Debye, en excellent accord avec les calculs *ab initio*. Enfin, nos images de microscopie électronique à transmission des SiNCs, déposés dans des conditions de plasma optimisées, ont révélé la présence d'une autre forme exotique de silicium à structure hexagonale. Une telle structure se forme habituellement à des pressions extrêmement élevées appliquées sur des structures cubiques (diamant) de silicium. Nous souhaitons affirmer que c'est grâce à la "chimie au marteau" que ces conditions ont été atteintes.

Dans la seconde partie, nous avons entrepris des études théoriques et expérimentales approfondies sur la croissance d'une nouvelle forme allotropique de silicium et de germanium: le silicène et le germanène, à savoir, une mono-couche d'atomes intégrée dans un réseau hexagonal qui ressemble fortement au graphène. Afin d'exclure tout mélange entre les atomes de silicium ou de germanium avec le substrat et de conserver leurs caractéristiques prometteuses comme de nouveaux matériaux de Dirac, nous avons effectué nos dépôts, sur un substrat de graphite chimiquement inerte. Une de nos découvertes cruciales est que les mono-couches de silicène ou de germanène interagissent avec le substrat de graphite uniquement via des forces de van der Waals. Cette interaction est suffisamment forte pour stabiliser les mono-couches, déposées même au-dessus de la température ambiante, mais suffisamment faible pour empêcher toute hybridation ou alliage entre le silicium ou le germanium et les atomes de carbone du substrat. Par conséquent, les propriétés électroniques exceptionnelles du silicène et du germanène, tels que les cônes de Dirac et les électrons sans masse, sont préservées même après leur dépôt sur les surfaces de graphite.

Acknowledgements

Looking back, I cannot remember where the years went. I had the best years and met so many amazing people. I would like to thank all of them for their kind and generous help.
Holger Vach, my thesis director and supervisor, there is so much I need to thank you for and I am not sure it will fit here, but hopefully you know how grateful and overwhelmed I am. I am grateful for and awed at how masterfully you managed that dual role as both my amazing teacher and my wonderful friend! Thank you for teaching me that research should first and foremost be fun. Thank you for your trust, your encouragement, and your pleasant disposition. With your persistent optimism and creativity, I have learnt that there is always a solution for any problem encountered. Holger, thank you from the bottom of my heart...
To my doctoral dissertation committee: Dr. Claudine Crépin-Gilbert, Prof. Laïfa Boufendi, Prof. Khaled Hassouni, Prof. Gilles Peslherbe, Dr. Thierry Belmonte, and Dr. Philippe Baranek. I gratefully acknowledge your detailed review of the manuscript, your great support, insightful comments, and fruitful suggestions.
I would like to thank Isabelle Berbezier, Maurizio De Crescenzi, Luca Persichetti, Elena Ivanova, Qadir Timerghazin, and Elyse Johnson. It has been a wonderful pleasure working with you and learning from you. It gives me immense pleasure to thank you, Marie Hénault, for your rewarding discussions and your valuable guidance and insight you provided during the plasma-related work. The intense collaboration with Andy Ruth and Bryan Keary has been very fruitful and has lead to outstanding results. Thank you for your time, effort, and your ideas. A thousand thanks, Yvan Bonnassieux, for always sharing your knowledge and constantly motivating me to strive for greater heights in life! I would also like to acknowledge and extend my heartfelt gratitude and special "thank you"to Jean-Charles Vanel and François Silva.
Ileana Florea, I cannot express enough my sincere love and adoration to you. I will forever be grateful to you and everything you have done. Mariam Ezzedine, I promise I will forever cherish our friendship. Thanks for always being by my side and for never asking for reasons or explanations when all I wanted was a long hug and a few laughs.
Lots of thanks to all members of LPICM: Pere Roca i Cabarrocas, Erik Johnson, Fatima Bouanis, Gaël Zucchi, Enric Garcia Caurel, Tatiana Novikova, Martin Foldyna, Jean-Luc Maurice, Jean Rehbinder, Denis Tondelier, Eric Paillassa, Frédéric Liege, Jérôme Charlic, Cyril Jadaud, Jean-Eric Bouree, Stanislas Deby, Rasha Khoury, Salomé Forel, Christoph Lechner, Jejune Park and all other current and former colleagues. It is marvelous to belong to a laboratory with such a great cooperation and social atmosphere. The gratification, knowledge, and joy I got from you were the highlight of my graduate years!
I very much thank Laurence Gérot, Gabriela Medina, and Jean-Luc Moncel at LPICM and the administrative staff at Ecole Polytechnique, as well as the user support team at IDRIS for all their great help. I would like to convey my hearty thanks to Hariri Foundation for Sustainable Human Development; Mrs. Bahia Hariri, the president, for the scholarship awarded to me and for opening a whole new world for me, Mrs. Dima El Hassan and Hiba Hneine for always being there for me.
Last but certainly not least, many thanks and warm thoughts go to everyone in my family who provided me love and encouragement from overseas.

Contents

Abstract iii

Acknowledgements v

List of Figures xi

List of Tables xv

1 Introduction 1
- 1.1 Exotic forms of silicon . . . 1
  - 1.1.1 Silicon with a variety of three-dimensional crystal structures . . . 1
  - 1.1.2 Silicon with a two-dimensional crystal structure . . . 2
  - 1.1.3 Silicon with multiple bonds . . . 3
- 1.2 Aromaticity . . . 3
  - 1.2.1 Silicon goes aromatic . . . 3
- 1.3 Objectives and outline of the thesis . . . 4

I Plasma-Born Aromatic Silicon Nanoclusters 7

2 Introduction 9
- 2.1 Electron-deficiency aromaticity in silicon nanoclusters . . . 9
- 2.2 Dusty plasma formation and detection . . . 11
  - 2.2.1 Detection of dust particles . . . 12
  - 2.2.2 Life stages of dust particles . . . 13
- 2.3 Outline of Part I . . . 13

3 Model and Methods 15
- 3.1 Molecular dynamics simulations . . . 15
- 3.2 Geometrical and electronic structure optimizations . . . 15
- 3.3 Magnetically-induced ring current calculations . . . 16
- 3.4 Electron localization function . . . 17
- 3.5 Nudged elastic band method . . . 18
- 3.6 Calculation of the absorption spectra . . . 19

4 Theoretical Results and Discussions 21
- 4.1 Properties of aromatic silicon nanoclusters . . . 21
  - 4.1.1 Toward global minimum energy structures . . . 21
    - 4.1.1.1 Stability of different nontetrahedral $Si_{19}H_{12}$ isomers . . . 22
  - 4.1.2 Electron-deficiency in silicon nanoclusters . . . 23
  - 4.1.3 Magnetically induced ring current . . . 23
  - 4.1.4 Electron localization function . . . 24

4.1.4.1 Two dimensional ELF plots of isomer A in comparison with C_6H_6 24
4.1.4.2 Two-dimensional ELF plots of isomer D 26
4.1.4.3 Two-dimensional ELF plots of isomer D in comparison with small metal clusters 26
4.1.5 Nudged elastic band calculations 27
4.1.6 Calculated absorption spectra 28
4.2 Silicon cluster band gap engineering 29
4.3 Conclusion 31

5 Applied Experimental Techniques: An Overview 35
5.1 Capacitively coupled discharge 35
5.1.1 Plasma enhanced chemical vapor deposition 37
5.1.2 Pulsed excitation 37
5.1.3 How does the temperature affect the growth of nanoparticles? 38
5.1.4 After-glow forces acting on particles 39
5.2 Optical Absorption Spectroscopy 39
5.2.1 Incoherent broadband cavity enhanced absorption spectroscopy 40
5.2.1.1 IBBCEAS measurement principle 41

6 Performed Experiments and Diagnostics 43
6.1 Experimental setup 43
6.1.1 Plasma reactor 43
6.1.2 Cavity-enhanced absorption setup 44
6.1.3 Mirror reflectivity calibration 45
6.1.4 Experiment synchronization 45

7 Experimental Results and Discussions 47
7.1 Extinction measurements 47
7.1.1 Investigation of the spectral range 575-665 nm 47
7.1.2 Investigation of the spectral range 655-745 nm 48
7.1.3 Effect of the gate delay time 49
7.2 Effect of an applied DC electric field 50
7.2.1 Permanent dipole moment 50
7.2.1.1 Polar molecules in a DC electric field 51
7.2.2 Experiment synchronization 52
7.2.3 Extinction measurements with a 120V DC bias 52
7.2.4 How does the extinction change as a function of the applied DC bias? . . 54
7.3 DC electric field simulations 55
7.3.1 Dipole forces acting on the nanoclusters 57
7.4 Distribution of the nanoclusters from trajectory simulations 61
7.5 Estimation of the permanent dipole moment 62
7.6 Characterization of deposited silicon nanoparticles 63
7.6.1 Structure of deposited silicon nanoparticles 63
7.7 Conclusion 65

II Two-Dimensional Materials 67

8 Introduction 69
8.1 Classification of materials based on dimensions 69
8.2 Graphene: The father of 2D materials 70
8.2.1 Hybridization of atomic orbitals 71
8.3 Silicene and germanene: novel 2D materials 73
8.3.1 The crystal structure 73

8.3.2 A brief history . . . 74
8.3.3 Our attempts to grow genuine silicene and germanene . . . 75
8.4 Outline of Part II . . . 75

9 Formation of Silicene Nanosheets on Graphite 77
9.1 Theoretical results . . . 77
9.1.1 Si atoms on a Ag(111) surface . . . 77
9.1.2 Silicene nanosheets on HOPG . . . 80
9.1.2.1 Silicene/HOPG structure optimizations . . . 80
9.1.2.2 Electonic band structure calculations . . . 81
9.1.3 Molecular dynamics simulations . . . 82
9.1.3.1 Thermal stability of a silicene sheet on HOPG . . . 82
9.1.3.2 Growth of a silicene sheet on HOPG . . . 84
9.2 Experimental results . . . 86
9.2.1 STM measurements . . . 86
9.2.2 STS measurements . . . 89
9.2.3 XPS measurements . . . 90
9.2.4 AFM measurements . . . 91
9.3 Conclusion . . . 92

10 Van der Waals Heteroepitaxy of Germanene Islands on Graphite 93
10.1 Theoretical results . . . 93
10.1.1 Germanene/HOPG structure optimisations . . . 93
10.1.2 Electronic band structure calculations . . . 94
10.2 Experimental results . . . 95
10.2.1 STM measurements . . . 96
10.2.1.1 Bare HOPG . . . 96
10.2.1.2 Germanene islands on HOPG . . . 97
10.2.2 STS measurements . . . 99
10.3 Conclusion . . . 99

11 Conclusions and Perspectives 101

A Molecular Dynamics Simulations 105
A.1 The basic idea . . . 105
A.1.1 Numerical integration of the equations of motion . . . 106
A.2 Classical *vs ab initio* molecular dynamics simulations . . . 107

B Density Functional Theory 109
B.1 The Schrödinger equation . . . 109
B.1.1 Born-Oppenheimer approximation . . . 110
B.2 Kohn-Sham density functional theory . . . 111
B.2.1 Exchange-correlation functionals . . . 112
B.2.2 Basis sets . . . 114
B.2.2.1 Localized basis sets . . . 114
B.2.2.2 Planewaves and pseudopotentials . . . 115
B.2.3 Dispersion interactions in DFT . . . 116
B.3 Structure optimization . . . 116

C Time-dependent Density Functional Theory 119
C.1 Time-dependent density functional theory . . . 119
C.1.1 Linear response TD-DFT . . . 120

D What is a supercontinuum light source? 123

E Basic Concepts in Solid State Systems 129
E.1 Basic concepts in crystallography 129
E.1.1 The hexagonal lattice 131
E.2 Electrons in a periodic potential 132
E.2.1 The Bloch function and the band structure 132
E.3 Density of states 133
E.4 Kpoint sampling 133
E.5 Periodic boundary conditions 134

F Experimental Techniques 137
F.1 Scanning tunneling microscopy/spectroscopy 137
F.2 Atomic force microscopy 139
F.3 X-ray photoelectron spectroscopy 139

Bibliography 141

List of Publications 147

List of Figures

1.1 Silicon phases obtained from high pressure treatments. 2
1.2 Silicene: A 2D allotrope of silicon. 3
1.3 Structure of a tricyclic aromatic isomer of hexasilabenzene. 4

2.1 The geometrical structure of $Si_{19}H_{12}$ (isomerA). 10
2.2 Calculated absorption spectra of a tetrahedral ($Si_{20}H_{20}$) *vs* a non-tetrahedral ($Si_{19}H_{12}$) nanocluster. 11
2.3 Time evolution of the amplitude of the third harmonic of the discharge current in a silane-based dust forming plasma. 12
2.4 Different stages of the growth of dust particles in a plasma reactor 13

3.1 Schematic illustration of induced magnetic field lines and induced ring currents . 16
3.2 Schematic illustration of the NEB method 18

4.1 The geometrical structure of different isomers of $Si_{19}H_{12}$ 22
4.2 Signed modulus of the magnetically induced current densities of isomer D of the $Si_{19}H_{12}$. 24
4.3 Magnetically induced current lines for benzene C_6H_6 in comparison with those for the highly-symmetric $Si_{19}H_{12}$ isomer A. 25
4.4 ELF plots in different planes for the $Si_{19}H_{12}$ nanocrystal (isomer A) and for C_6H_6. 26
4.5 ELF plots in different planes for the presently most stable isomer D. 27
4.6 ELF plots for three small metal clusters in comparison with isomer D. 28
4.7 $Si_{19}H_{12}$ scaffold resulting from a Nudged Elastic Band calculation between the initial $Si_{19}H_{12}$ nanocrystal, isomer A, and isomer D. 29
4.8 Absorption spectra calculated for two isomers of the $Si_{19}H_{12}$ nanocluster. 30
4.9 Absorption spectrum calculated for the active solar cell layer. 31

5.1 A typical capacitively coupled plasma setup. 36
5.2 Scheme of an RF discharge in a parallel-plate reactor with capacitive coupling of the RF generator. 37
5.3 Pulsed excitation parameters. 38
5.4 Time evolution of the amplitude of the third harmonics for different gas temperatures. 38
5.5 Schematic illustration of light passing through an optical cavity in IBBCEAS . . 40

6.1 Schematics of the experimental setup. 44
6.2 Typical trigger sequence to synchronize the iCCD with the RF power supply. . . 46

7.1 Extinction measured using the 610 nm mirrors. 48
7.2 Extinction measured using the 700 nm mirrors. 49
7.3 Extinction measured using the 610 nm mirrors for a range of gate delay times. . 50
7.4 Electric dipole moment 51
7.5 Polar molecule in an electric field. 51
7.6 Trigger sequence with an applied DC bias. 52

7.7 Extinction measurements with and without an applied bias of 120V. 53
7.8 Fractional difference between the measured extinction with and without an applied DC bias of 120V. 53
7.9 A set of extinction measurements with and without applied DC bias. 54
7.10 Reduction in the measured absorption as function of the applied DC bias. 55
7.11 A schematic representation of the reactor chamber. 56
7.12 Cross-sectional view of the electric field simulations. 57
7.13 Dipole forces acting on the nanoclusters in the z-direction. 58
7.14 A comparison of the different forces acting on a spherical nanoparticle as a function of its diameter. 59
7.15 The gradient of E_r along the polar axis with θ=0 for the different applied biases. 60
7.16 Three-dimensional representation of the gradient of E_r calculated for a 240V bias. 60
7.17 Schematic illustration of the distribution of particles on a plane. 62
7.18 Reduction in the measured absorption and calculated particle density as a function of the applied DC bias. 63
7.19 HRTEM images of silicon nanoparticles obtained after different deposition times. 64
7.20 HRTEM images of crystalline silicon nanoparticles. 65

8.1 Band structure and ball-and-stick model of graphene. 71
8.2 Hybridization of atomic orbitals. 72
8.3 Free-standing silicene and germanene. 73

9.1 AIMD snapshots of 6 Si atoms on Ag(111). 78
9.2 Typical AIMD snapshots of 12 Si atoms on Ag(111). 79
9.3 Mean square displacement of the top Ag atoms averaged over several MD steps as function of Si coverage investigated separately for Si monomers, dimers and trimers. 80
9.4 Atomic structure model of the silicene on HOPG system. 81
9.5 The electronic band structure calculated from DFT. 82
9.6 AIMD snapshots of a silicene sheet on HOPG. 83
9.7 Typical snapshots from AIMD simulations of the epitaxial growth of a silicene monolayer on HOPG at RT. 85
9.8 Scanning tunneling microscopy images of one monolayer silicon deposited on HOPG at room temperature. 87
9.9 Scanning tunneling microscopy image of the bare HOPG substrate. 88
9.10 Scanning tunneling microscopy image of one monolayer of Si deposited on HOPG at room temperature. 89
9.11 Scanning tunneling spectroscopy measurement. 90
9.12 Xray photoemission spectra and atomic force microscopy images. 91

10.1 Atomic structure model of the germanene on HOPG system. 95
10.2 Electronic band structure of germanene/HOPG by DFT calculation. 96
10.3 Atomic-resolution STM images of the bare graphite surface used as a template for the germanene growth. 97
10.4 STM images showing 2D islands formed after Ge deposition at room temperature and subsequent annealing to 350°C. 98
10.5 Scanning tunneling spectroscopy measurements and density of states calculations. 100

D.1 Demonstration of self-phase modulation in a laser pulse 127

E.1 The unit cell and Wigner-Seitz cell. 130
E.2 Real space lattice and Brillouin zone of graphene. 131
E.3 Brillouin zone sampling. 134
E.4 2D representation of PBC. 135
E.5 Schematic representation of a slab model. 135

F.1 Schematic illustration of scanning tunneling microscopy. 138
F.2 Schematic illustration of atomic force microscopy. 139
F.3 Principle of Xray photoelectron spectroscopy. 140

List of Tables

4.1 Summary of the skeleton energies for different hydrogenated silicon clusters. . . . 23
4.2 Summary of the optical gaps for different hydrogenated silicon clusters. 30

Chapter 1

Introduction

Silicon, an element that is everywhere

Silicon, an abundant and nontoxic element, has become a technologically paramount material in the last century. Silicon lies at the heart of our modern technology as the material for integrated circuits and solar cells. In short, silicon is to technology as carbon is to biology. Thanks to the favorable properties of its amorphous and diamond-cubic lattice structures; such as stability at high temperature, ability to be both p and n doped, and ability to grow an oxide surface layer, that silicon has gained such a technological supremacy. Fortunately, silicon possesses a rich and complex free energy landscape, with many local energy minima, allowing for the formation of a variety of unusual new structures. The so far discovered exotic structures of silicon have shown to exhibit desirable properties so that one or more of those structures could become the basis for the next revolution in nanotechnological devices.

1.1 Exotic forms of silicon

1.1.1 Silicon with a variety of three-dimensional crystal structures

Several exotic allotropes of Si were formed under the application of **extremely high pressure** using different methods.[1] At high pressure, Si takes on numerous dense structures with *increasing coordination* and tends to favor a metallic behaviour. Under the compression of the standard 4-fold coordinated diamond-cubic Si (referred to as Si-I) to ∼12 GPa, it undergoes metallization into Si-II (body centred tetragonal) and becomes 6-fold coordinated.[2] Above ∼13 Gpa, Si-II distorts into a body-centred orthorhombic structure.[3] Yet, with the application of more pressure, this polymorph transforms into an 8-fold coordinated simple hexagonal structure (Si-V) at ∼16 GPa.[4] Another orthorhombic structure (Si-VI) is found at ∼38 GPa, with a mixture of 10- and 11-fold coordination.[4, 5] Compression to ∼42 GPa yields the 12-fold coordinated hexagonal close-packed structure (Si-VII).[4] Finally, the face-centred cubic structure (Si-X) forms at ∼79

GPa.[6] Most of the obtained structures are stable only at high pressures, but some structures are found to be stable at ambient temperature and pressure. Under slow pressure release starting from Si-II, the rhombohedral R8 phase is obtained at ∼8 GPa, followed by a transition to bc8 (Si-III) at ∼2GPa. Si-III remains stable at ambient conditions. Subsequent thermal annealing of Si-III leads to the formation of a stable hexagonal diamond, Si-IV (see Figure 1.1).[1, 7]

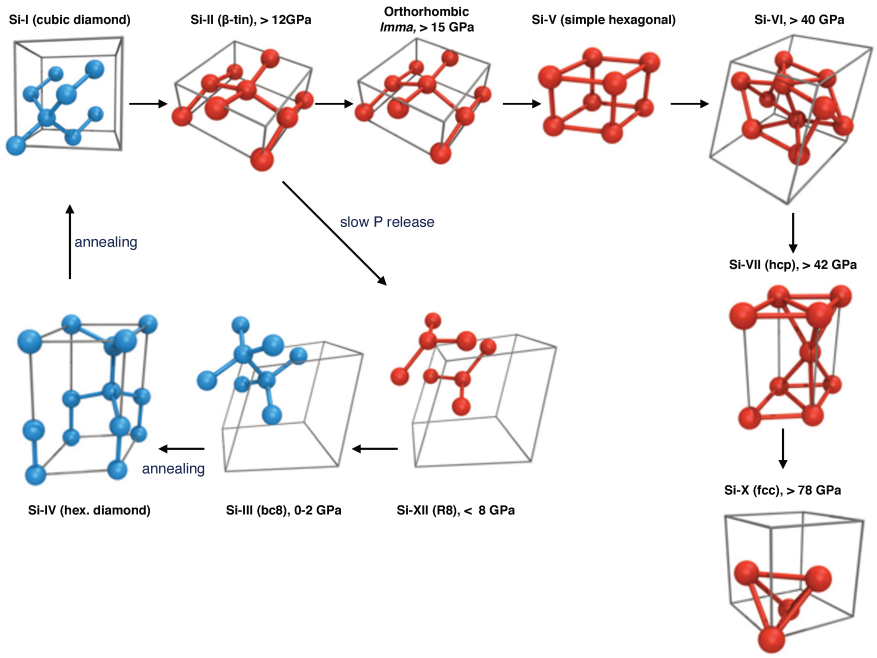

Figure 1.1: Silicon phases obtained from high pressure treatment.[7]

1.1.2 Silicon with a two-dimensional crystal structure

Not only it has shown to form a variety of three-dimensional (3D) crystal structures with different chemical bonding schemes, silicon has also proved to form a two-dimensional (2D) crystal structure. This new synthetic form, named sililcene, has a hexagonal lattice structure that resembles, to a great extent, the structure of graphene[1] (see Figure 1.2). Interestingly, silicene shares similar electronic properties as graphene: near the Dirac point, where valence and conduction bands meet, the electronic band structure is linear. However, unlike graphene that can be isolated from its parent crystal graphite, silicene does not exist naturally and needs to be synthesized on suitable substrates.

[1] Silicene is one part of the thesis work. It will be discussed in detail in Part II.

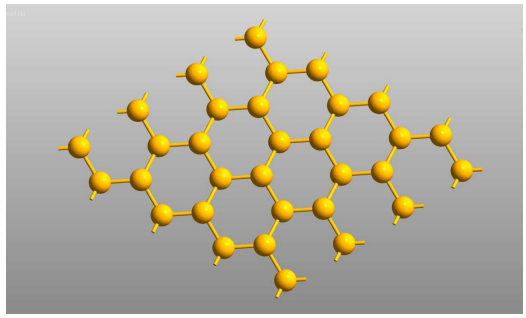

Figure 1.2: Silicene: A 2D allotrope of silicon.

1.1.3 Silicon with multiple bonds

A different, yet exotic, form of silicon was realized by West *et al.* in the early 1980s when they succeeded in stablizing a compound containing a Si-Si **double bond**, tetramesityl**disilene**.[8] There work was, by itself, a major breakthrough and had proved controversial to the "double bond-rule". According to this rule, multiple bonds become less stable for second- and third-row elements; it was justified to be the result of the large radii of these atoms, leading to poor overlap between adjacent p orbitals. The secret for their success was the kinetic stabilization by protecting the molecule's reactive sites with bulky substituents that form a protective shell around the highly reactive Si-Si double bond. Since then, about 100 disilenes[9] as well as compounds with a Si-Si **triple bond** have been isolated.[10]

1.2 Aromaticity

The concept of aromaticity has fascinated chemists since the 1860s when the *architect of chemistry*, August Kekulé, first introduced the term aromaticity in his famous papers,[11–13] and explained the particular stability and low reactivity of a class of molecules related to benzene and its derivatives. In 1931, Hückel formulated his famous $4n+2$ rule.[14, 15] It states that if an unsaturated monocyclic hydrocarbon molecule has the right number of π-electrons obeying this rule, then the molecule is aromatic and has high stability and low reactivity. Aromaticity was primarily limited to the branch of organic chemistry. However, with the high-level theoretical treatments and advances in experimental techniques to create novel molecules and clusters, the concepts of aromaticity have found wider applicability far beyond benzene.[16, 17]

1.2.1 Silicon goes aromatic

As a consequence of the π bonding capability of Si and the crucial role of benzene in the field of aromatic chemistry, aromaticity in compounds involving Si shifted into focus. Considerable research interests have been directed toward the synthesis and characterization of aromatic Si

compounds. Such unconventional structures have proved to be stable. However, their stability relies on an extremely complicated atomic structure.[18] A tricyclic aromatic isomer of hexasilabenzene, was recently reported by Scheschkewitz *et al.* The structure they had obtained had six mobile electrons cyclically delocalized over four cenrtal Si atoms (see Figure 1.3). Theoretical analyses have revealed that the mobile electrons were of π-, σ- and non-bonding type electrons, in contrast to the renowned six π-electrons of Hückel aromatic systems. The attachment of highly bulky molecules (see the "Tip"in Figure 1.3) is inevitable to give the structure the kinetic and thermodynamic stability. Such a discovery, by its very nature, brings with it the amelioration to the field of aromaticity. However, the cumbersome structure of those synthetic aromatic Si compounds prevents their use as building blocks for the construction of bigger structures, as it is the case in organic chemistry.

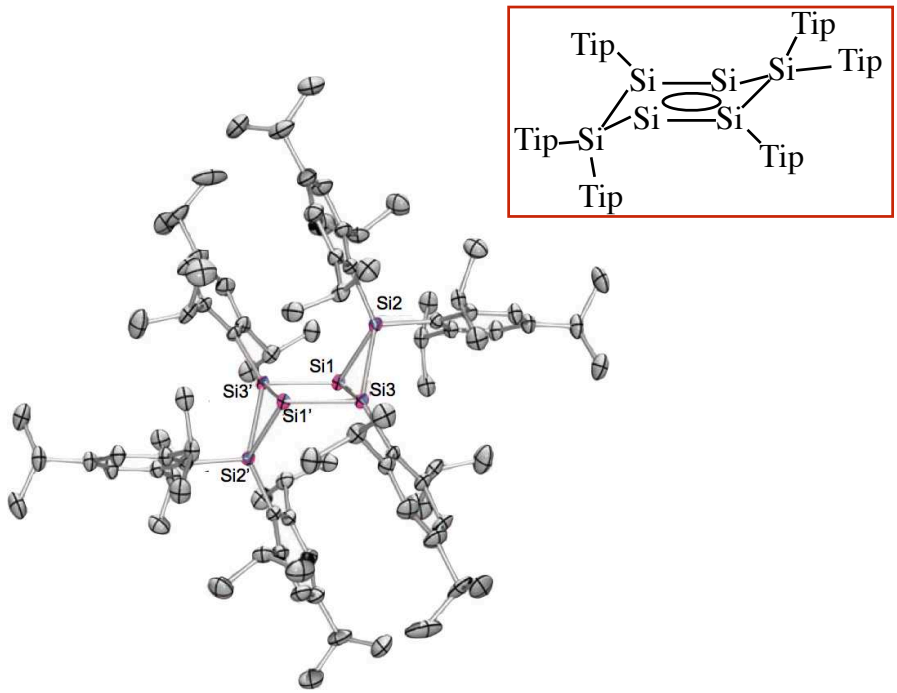

Figure 1.3: Structure of a tricyclic aromatic isomer of hexasilabenzene. The hexasilabenzene isomer **3a** crystallizes as a naphthalene solvate (**3a**·2 $C_{10}H_8$). The inset shows hexasilabenzene isomer **3a** (Tip, 2,4,6-triisopropylphenyl) for clarity.[18]

1.3 Objectives and outline of the thesis

After we have shed some light on distinctive forms of silicon, now it is time to present our work on some of its new exotic allotropes. The thesis is divided into two parts and its goals can be summarized as follows: In Part I, (i) in-depth theoretical studies on plasma-born hydrogenated silicon clusters with a new allotropic form of silicon. Those nanoclusters form spontaneously

by self-assembly under appropriate experimental conditions, they exhibit nontetrahedral structures and are ultrastable. They are found to have an inner over-coordinated Si atom exhibiting electron-deficient bonds which induce high electron delocalization and, thus, possess aromatic properties. (ii) Measurements of their absorption spectra in the visible region, *in situ*, in a plasma reactor using incoherent broadband cavity enhanced absorption spectroscopy. (iii) Proof that those nanoclusters possess a permanent dipole moment and an estimation of its value. (iv) Structural characterization of deposited nanoclusters. In Part II, silicene, that has attracted a lot of interest recently, but has been mostly synthesized on metal substrates, has triggered some fierce controversy since Si atoms of the silicene layer seem to become interchanged with the metal atoms of the substrate. (v) In-depth theoretical and experimental studies of silicene, as well as germanene, deposited on a chemically inert graphite substrate are performed to prove the existence of genuine, alloy-free, two-dimensional, graphene-like silicon and germanium materials with extraordinary electronic properties.

The thesis is organized in the following way:

Part I starts with an introduction, presented in Chapter 2, which gives an overview of (a) electron-deficiency aromaticity of plasma-born silicon nanoclusters based on theoretical studies found in the literature; (b) growth of silicon nanoclusters in a silane-based plasma reactor based on previous experimental studies. Chapters 3 and 4 are related to the theoretical work of the thesis. The former presents the methods and models used to investigate different properties of the isomer scaffold of hydrogenated silicon clusters with a $Si_{19}H_{12}$ stoichiometry. The latter highlights the theoretical results and discussions, while Chapters 5, 6, and 7 present the experimental aspects related to this work. In Chapter 5, a short overview of several experimental techniques is presented and in Chapter 6, the experiments and the diagnostics related to the thesis work are detailed. Finally, the promising results are demonstrated in Chapter 7.
Part II is devoted to the studies of silicene and germanene materials. Chapter 8 provides an introduction to 2D materials with a review of the current literature on silicene and germanene. Chapter 9 investigates the growth of silicene on a graphite surface done for the first time. Based on combined theoretical and experimental studies, the structural and electronic properties are discussed with the aim of providing a proof of the formation of genuine silicene sheets with remarkable electronic properties. Similarly, Chapter 10 discusses the successful growth of flat 2D sheets of germanium on graphite with electronic properties very different from any other known germanium-based nanostructure.

The conclusions of this thesis and suggestions for future work are presented in Chapter 11. Thereafter, six Appendices are given, followed by a bibliography. The three Appendices, A, B and C, detail the theoretical background (molecular dynamics simulations, density functional theory, time-dependent density functional theory), Appendix D explains briefly the generation of a supercontinuum light source, Appendix E describes basic concepts in solid state systems, and Appendix F explains briefly the experimental techniques used in Part II.

Most of the results of this thesis are presented by means of papers that have been published in peer-reviewed journals (a list is provided at the end of this thesis), while the remaining results are under preparation for publication. We hope that we have succeeded in presenting our work in a comprehensive and attractive way and that you will enjoy reading this thesis.

At this point, we would like to take the opportunity and clarify that the research work was carried out collaboratively as follows:

- All experiments in Part I of the thesis were performed by us in LPICM. The cavity enhanced absorption measurements were the result of a successful collaboration with experts in this field of research, Andy Ruth and Bryan Keary from University College Cork (UCC), Cork, Ireland. We combined our plasma reactor with their cavity enhanced absorption set-up and performed the absorption measurements together.
- Nudged elastic band calculations in Part I of the thesis were performed by L. Ivanova and Q. Timerghazin in Marquette University, Milwaukee, USA.
- All other theoretical calculations and simulations have been accomplished by us at LPICM.
- All experiments in Part II of the thesis were performed by several research teams from different institutions in France and Europe: 1) Aix-Marseille University, IM2NP-CNRS Campus de St. Jérome, Marseille, France directed by Isabelle Berbezier, 2) University di Roma "Tor Vergata", Roma Italy directed by Maurizio De Crescenzi, 3) Department of Materials, ETH Zurich, Switzerland directed by Luca Persichetti. Those measurements and our simulations turned out to be highly symbiotic; *i.e.* sometimes our simulations helped to interpret the experimental results and sometimes they guided the experimental teams to explore yet another aspect.

Part I

Plasma-Born Aromatic Silicon Nanoclusters

Chapter 2

Introduction

2.1 Electron-deficiency aromaticity in silicon nanoclusters

In 2012, Vach introduced a new concept of aromaticity, namely "electron-deficiency aromaticity". [19] In his work, Vach had shown the possibility of obtaining aromatic-like behavior with very simple and extremely stable systems. Unlike other strategies that rely on the formation of multiple bonds in order to achieve aromaticity in Si compounds, and that become impossible without binding the Si atoms to bulky stabilizing molecules (see Figure 1.3), the systems that Vach found are composed of only Si and H atoms and have a size of ∼1nm. In his approach, Vach had exploited the natural tendency of Si to **overcoordination** for the formation of electron-deficient systems in a silane-based plasma. Overcoordination of Si does not only appear in systems subjected to extremely high pressure, yet it has also shown to occur in liquid Si where the first nearest-neighbor atomic coordination number is found to be 5.5-6.[20] The deficiency of electrons in the bonds between Si atoms will induce extensive electron delocalization and will, in turn, provide enhanced stability to the system, as well as other aromatic properties. This novel phenomenon was the outcome of extensive studies on the nucleation and growth of hydrogenated silicon (Si_mH_n) nanoclusters in a plasma based on a variety of theoretical methods.[21–23]

The growth of Si_mH_n nanoclusters in a silane plasma was investigated using first-principles molecular dynamics simulations.[21] First, fluid model calculations provided a realistic description of the low-temperature silane plasma, such as the relative density of the different plasma species, their temperature, and their collision interval times.[23] Using the obtained data as input parameters for the molecular dynamics simulations, the dynamics of the cluster growth, as a result of the consecutive capture of plasma molecules and radicals (SiH_4, SiH_3, SiH_2), was followed. The simulations have always shown the *spontaneous* organization of Si atoms around one central Si atom leading to overcoordinated amorphous clusters. Moreover, simulations have revealed the crucial role of atomic and molecular hydrogen fluxes. The interaction of the growing cluster with hydrogen atoms and molecules determines its final structure; *i.e.*, chemical reactions with hydrogen atoms heat the growing clusters permitting the atoms to overcome local energy barriers and attain new positions, while the collisions with hydrogen molecules cool the cluster

down and fix the cluster atoms in their new positions. Therefore, the resulting overcoordinated cluster could either become crystalline or remain amorphous.[21]

The properties of those *self-assembled* crystalline (symmetric) and amorphous (asymmetric) **nontetrahedral** nanoclusters were studied at a high-level of theory: using *ab initio* methods. Among the reported nanoclusters, we will focus here on one precise example that combines overcoordination with highly symmetrical ring structures, $Si_{19}H_{12}$ (isomerA) shown in Figure 2.1. A natural bond orbital analysis revealed that most Si-Si bonds are *poor* in electrons: 1.64 electrons per bond in the Si-Si bonds of the central hexagon, 1.84 electrons per bond in the bonds between the next-neighbor Si atoms belonging to an external and the central hexagon, and 1.00 electron per bond in the six bonds between the central Si atom and its 6 nearest-neighbors. Furthermore, the sum of all stabilization energies due to electron delocalization in $Si_{19}H_{12}$ was found to be about 12 times higher than in benzene. The highly delocalized nature of the electrons provide the structure with a great stability. In contrast to the extrastability in convential aromatic structures, such as benzene, which originates from the excess number of electrons in a single bond, the ultrastability in the present case originates from the deficiency in the number of electrons to form single bonds between neighboring atoms. Consequently, electrons in both situations will be highly delocalized providing stability to the structures.[19]

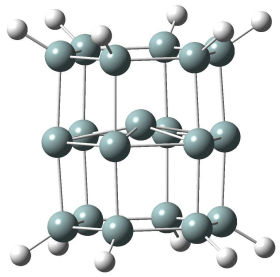

Figure 2.1: The geometrical structure of $Si_{19}H_{12}$ (isomer A).

Interestingly, a detailed analysis of the electron density calculations have shown that the non-tetrahedral nanoclusters possess a **permanent dipole moment**. Isomer A, for instance, has a permanent dipole moment of ∼2 Debye. The dipole moment stems from the way the charges are distributed and from the shape of the nanocluster; the relative high density of charges in the vicinity of the inner overcoordinated Si atom and its non-central position, result in a permanent dipole moment. Furthermore, calculations on the magnetic shielding and the magnetically induced ring currents have shown that this nontetrahedral silicon nanocluster acquires some aromatic properties that are 3 times stronger than that of benzene.[22]

Indeed, Si manifests remarkable changes in its optical and electronic properties when its size approximates the exciton Bohr radius. Those particular properties derive from the quantum confinement effect. Under quantum confinement conditions, the band gap becomes size-dependent, increasing as the size decreases. Therefore, tuning the absorption and emission spectra, by

changing the size of nanoclusters, has attracted the interest of many researchers. So far, however, the absorption spectra of pure tetrahedral Si nanoclusters is limited to the ultraviolet (UV) region. Hence, the clusters are often doped with expensive and toxic metal atoms to extend their response to the visible and infrared (IR) regions. In contrast, first-principles calculations have shown that structure-induced electron-deficient pure Si_mH_n nanoclusters can absorb, not only in the UV, but also in the visible and IR spectral regions. Figure 2.2 compares the calculated absorption spectra of a tetrahedral and a nontetrahedral nanocluster, having comparable sizes.

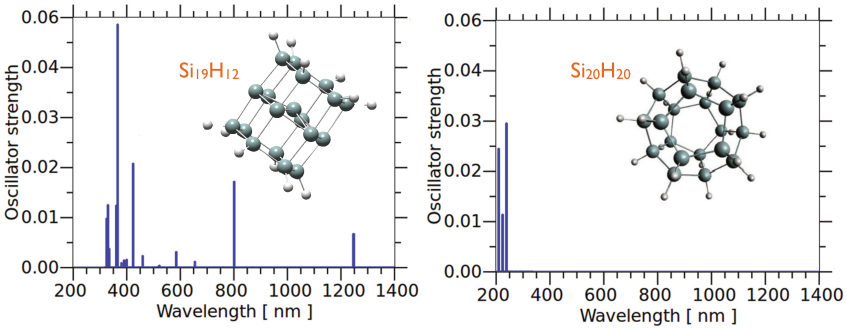

Figure 2.2: Calculated absorption spectra of a tetrahedral ($Si_{20}H_{20}$) *vs* a nontetrahedral ($Si_{19}H_{12}$) nanoclusters. *Left*: The absorption of the nontetrahedral nanocluster extends from the UV until the IR spectral region. *Right*: The absorption of the tetrahadral nanocluster is confined to the UV region.

Finally, the wealth in the properties of nontetrahedral Si_mH_n nanoclusters, that form by self-assembly in a plasma reactor and that have a size of ∼1 nm, have intrigued us to deeply delve in search of even more fascinating properties.

2.2 Dusty plasma formation and detection

In the last three decades, the experimental community have performed extensive investigations on the nucleation and growth of nanoparticles in a low-pressure radio frequency (RF) silane-based plasma. Their work was stimulated by the ubiquitous presence of dust particles in a plasma environment. The existence of dust particles was a curse for certain applications and a blessing for others. In the former case, dust particles are deemed as unwanted in the microelectronics manufacturing processes. Those dust particles can be deposited on a wafer during a plasma operation which will influence the device topography, performance and reliability. In the latter case, the incorporation of nanocrystals, that form in a plasma operating near dust conditions, in the intrinsic amorphous hydrogenated silicon layer (a-Si:H) can readily enhance the performance of photovoltaic devices.[24, 25] Due to their various technological implications, understanding the kinetics of the particle nucleation and growth as well as the ability to control their size is crucial. Substantial and indispensable experimental studies were done by Boufendi and his

coworkers to detect and follow the growth of dust particles in the plasma gas phase using a variety of methods.[26]

2.2.1 Detection of dust particles

The laser light scattering technique was used in the first place to detect and size the nanoparticles while they were growing. However, this technique was limited to nanoparticle sizes down to 20 nm due to the very low scattering cross-section which depends on the sixth power of the particle radius.[27] In order to detect much smaller particles, Boufendi *et al.* developed a method based on the use of the discharge and plasma physical characteristics. Since the plasma impedance is drastically modified due to the particle formation and growth, Boufendi *et al.* have used an electrical diagnostic tool based on the time evolution of the amplitude of the third harmonic (3H) of the discharge current, the amplitude of the self-bias (V_{DC}), and the electron density that are correlated with all events occurring in a plasma gas phase.

Figure (2.3) shows how the time evolution of the amplitude of 3H of the discharge current for a room temperature (RT) silane plasma discharge is affected. As soon as we turn on the plasma, a very steep increase in the amplitude of the discharge current takes place. In the few 100 ms, thereafter, the change is very small, indicating that most of the nanoparticles are neutral and this change is due to a modification of the electron collision frequency. Here, the formation and accumulation of nanocrystallites (with a size of ∼2 nm) takes place. The slight increase at the end of this part (blue circle) is an indication of the beginning of the agglomeration phase. The second drastic drop is due to the electron attachment on the particles. The amplitude of 3H reaches a constant value at about 4 s indicating the termination of the agglomeration phase. Particles then continue to grow by molecular radical sticking on their surface. Particles were collected at different stages and analyzed by electron microscopy.[26]

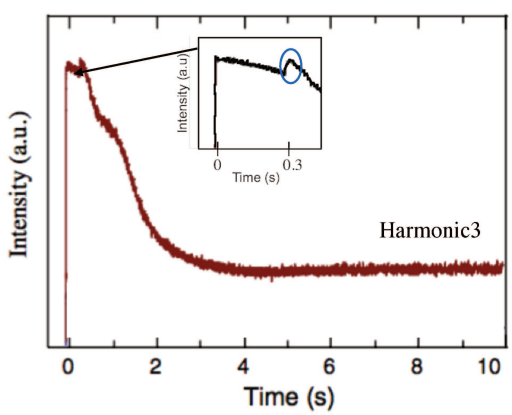

Figure 2.3: Time evolution of the amplitude of the third harmonic of the discharge current in a silane-based dust forming plasma. Inset: A zoom into the vicinity of the first stage and the beginning of agglomeration stage.[26]

2.2.2 Life stages of dust particles

Boufendi *et al.* found that the dust particle formation and growth in a low-pressure RF discharge is divided into a three-stage process.[28] An illustration of the growth process is given in Fig (2.4) where the first two columns correspond to the first stage:

1. Formation and accumulation phase, *i.e.* a conversion process from gas species to particles. This process is stimulated by the fast silane molecule and radical interactions with negative ion clusters. The size of those **first-generation particles** is about 2nm. When the concentration of those particles increases up to a critical value (10^{10}-10^{11} cm^{-3}), which corresponds to a mean distance between the nanoparticles of about 1μm, the new-particle formation terminates. At this stage, the electron temperature remains about 2eV.

2. Agglomeration phase. A fast agglomeration process takes place leading to large (50 nm) dust particles. During the agglomeration process, a critical phenomenon, so called α - γ' transition, takes place. It is characterized by a strong decrease of the free electron concentration and a significant increase of their energy. After the α - γ' transition, the electron temperature increases up to 8 eV while the electron concentration falls ten times.

3. Further growth of the dust particles takes place by the attachment of radicals on their surface until micrometer sized dust particles are obtained.

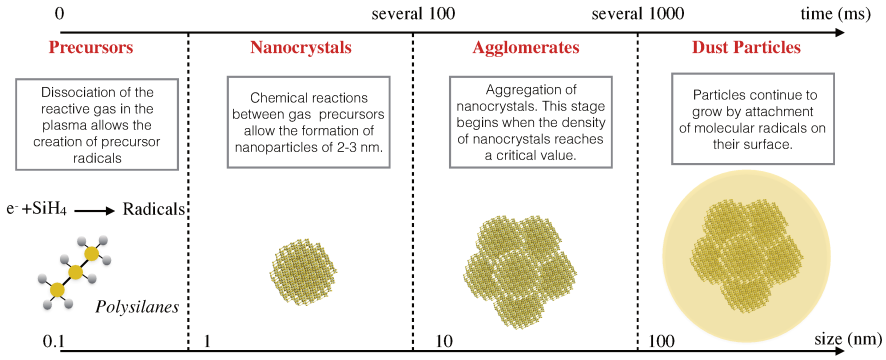

Figure 2.4: Different stages of the growth of dust particles in a plasma reactor.

2.3 Outline of Part I

In the following, we present our work on plasma-born aromatic silicon nanoclusters based on theoretical and experimental studies. In our theoretical investigations, we focus on one isomer with a $Si_{19}H_{12}$ stoichiometry and with an asymmetric configuration. We present in Chapter [3] the different methods used in our study and in Chapter [4] the obtained results. We start

our experimental part in Chapter [5] with an overview of capacitively coupled plasma (CCP) processes and the principles of cavity-enhanced absorption spectroscopy. In Chapter [6], we describe our experiments and diagnostics. In Chapter [7], we present the experimental results along with discussions.

Chapter 3

Model and Methods

This chapter describes the computational methods used throughout our study on aromatic silicon nanoclusters, focusing on one isomer with a $Si_{19}H_{12}$ stoichiometry and with an asymmetric configuration. We will refer to it as isomer D in the text. A theoretical background covering molecular dynamics simulations, density functional theory (DFT) and time-dependent DFT (TD-DFT) is presented in Appendices A, B, and C, respectively.

3.1 Molecular dynamics simulations

Ab initio molecular dynamics (AIMD) simulations were performed with the Vienna Ab initio Simulation Package (VASP-5.3.5)[29] using a projector-augmented wave (PAW) pseudopotential[30] in conjunction with the Perdew-Burke-Ernzerhof (PBE)[31] exchange-correlation functional. The planewave basis set was restricted to a cut-off energy of 500 eV and the time-step was 0.1 femtoseconds. The convergence criterion for the electronic iterations was chosen to be 10^{-5} eV.

3.2 Geometrical and electronic structure optimizations

The geometrical and electronic structure optimizations of the hydrogenated silicon nanocluster under study[1] were systematically performed with DFT using the hybrid, non-local exchange and correlation functional (B3LYP) with the Gaussian 09 software.[32] The 6-311++G (d,p) basis set with diffuse and polarisation functions was used for both Si and H atoms. We have used an open shell system to optimize the structures for different multiplicities and found that the lowest energy structures are obtained for the singlet state that can well be described as a closed shell system. In all cases, a frequency analysis was performed to verify vacuum stability.

[1] Structure optimizations were also done with plane-wave basis sets using VASP leading to essentially identical results as with atom-centred basis sets. Quasi identical results based on different methods and functionals underlines the reliability of the calculations.

3.3 Magnetically-induced ring current calculations

Aromatic ring currents can be induced in aromatic systems, *i.e.* structures exhibiting delocalized electrons. When such a molecular system is exposed to an external magnetic field, its electrons are forced to move around parts or the entire structure since the electrons involved are "free"rather than being localized in bonds. Consequently, a ring current is induced which is a direct consequence of Ampere's law. In quantum systems, however, spatially separated magnetically induced currents might simultaneously flow in the classical direction (diatropic current) and in the nonclassical direction (paratropic current) (Figure 3.1). The ring current will induce a secondary magnetic field which in paratropic regions enhances the external magnetic field and in diatropic regions opposes the external field.[33]

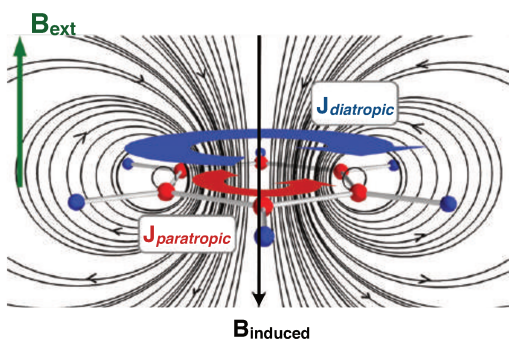

Figure 3.1: Schematic illustration of induced magnetic field lines and induced ring currents. A distinction between the classical (diatropic) and nonclassical (paratropic) directions of the induced current flow relative to the applied external magnetic field using the benzene molecule as an example.[33]

Quantum mechanical approaches use perturbation theory to study the linear change in the magnitude of the current density with respect to the strength of the external magnetic field, leading to the *induced current density susceptibility*. Analyzing current densities provides information about the electron delocalization in the investigated system. One can perform visual inspections of the current density susceptibility in selected planes, for example parallel to molecular rings at a given distance, or in three dimensions. Visualization inspections provide qualitative information about the current density and current pathways. Alternatively, one can perform integration to obtain quantitative values for the strength of the current flow passing through defined cross section areas in molecular systems. The total net current strength will be the sum of the diatropic and paratropic contributions.

The gauge-including magnetically induced current (GIMIC)[34, 35] and the CFOUR[36] program packages were used to calculate first the unperturbed atomic-orbital (AO) density matrix as well as the three magnetically perturbed AO density matrices on a Møller-Plesset (MP2[2])/6-31G* level of theory.

[2]Møller-Plesset perturbation theory is one of several post Hartree-Fock *ab initio* methods. This method adds electron correlation effects by means of Rayleigh-Schrödinger perturbation theory to the second order.[37]

3.4 Electron localization function

The Electron localization function (ELF) has emerged as a powerful tool to understand in a qualitative way the behavior of electrons in a nuclei system. It is possible to explain a great variety of bonding situations ranging from the most standard covalent bond to the metallic bond. In 1990, Becke and Edgecombe[38] introduced the ELF as a "simple measure of electron localization in atomic and molecular systems". They associated the localization of an electron with the probability density for finding a second like-spin electron near a reference point

$$D(\mathbf{r}) = \sum_i |\nabla \phi_i(\mathbf{r})|^2 - \frac{1}{4}\frac{|\nabla \rho(\mathbf{r})|^2}{\rho(\mathbf{r})} \tag{3.1}$$

For small probability densities, $D(\mathbf{r})$ is also small and the electron is more localized. Becke and Edgecombe proposed two additional scaling rules.

1) The homogeneous electron gas is used as a reference, the kinetic density of which is given by

$$D_0(\mathbf{r}) = \frac{3}{10}(3\pi^2)^{2/3}\rho(\mathbf{r})^{5/3} \tag{3.2}$$

2) For numerical convenience the function is mapped to one; *i.e.* the ELF is defined between 0 and 1. Hence, they proposed the following ELF:

$$ELF = \frac{1}{(1+\chi^2)} \tag{3.3}$$

where

$$\chi = \frac{D}{D_0} \tag{3.4}$$

Becke and Edgecombe attributed the ratio χ to a dimensionless localization index, calibrated with respect to the uniform electron gas. In this way, the following inequality is obeyed

$$0 \leq ELF \leq 1 \tag{3.5}$$

and a value of the ELF close to 1 corresponds to a region in space where there is a high probability of finding electron localization, whereas an ELF value close to one-half corresponds to a region of electron gas-like behavior.[39] Moreover, local ELF maxima are entitled "attractors". In this sense, covalent bonds can normally be identified by ELF attractors in between the two corresponding atoms.

ELF Plots: The ELFs were plotted using the Multiwfn program[40] using a color-filled map. This type of map uses different colors to present real space function value in different regions. By default, if the function value exceeds lower (upper) limit of color scale, then the region will be filled by black (white).

3.5 Nudged elastic band method

For most chemical reaction to occur, an **energy barrier**, also known as activation energy, has to be overcome so that the reaction proceeds. Although one knows the *initial* and *final* states of the reaction, reaction intermediates often remain anonymous. The nudged elastic band (NEB) is a method employed for finding saddle points and minimum energy paths (MEP) between two energy minima, *i.e.* the initial and final states. The working mechanism for this method comprises; 1) linear interpolation of a set of images between the two minima, 2) connection of these images together with springs (forming an elastic band), and 3) minimization of the energy of each image. Each image corresponds to a specific geometry of the atoms on their way from the initial to the final state, a snapshot along the reaction path. Thus, once the energy of this string of images has been minimized, the true MEP is revealed.
Obviously, the spring constant has a strong effect on the result. That is why the "nudged"method has been developed to enhance the traditional elastic band method. The NEB method introduces a force projection scheme to project out the perpendicular component of the spring force and the parallel component of the true potential force. Then, the competitive relation between the spring force and the true potential force is eliminated. Now, the total force on each image in the NEB method is the sum of the true potential force perpendicular to the local tangent and the spring force along the local tangent (Figure 3.2). Once the energies of these interpolated images are minimized; *i.e.*, the artificial elastic forces are equal to zero, the mimicked elastic band is the true MEP.[41]

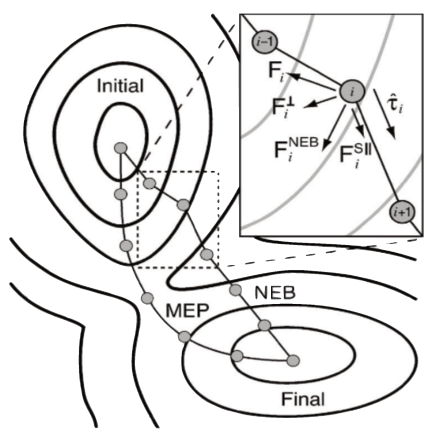

Figure 3.2: Schematic illustration of the NEB method Two components make up the nudged elastic band force $\mathbf{F}^{NEB}$: the spring force $\mathbf{F}_i^{S||}$, along the tangent τ_i, and the perpendicular force due to the potential $\mathbf{F}_i^{\perp}$. The unprojected force due to the potential $\mathbf{F}_i$ is also shown for completeness.[41]

The NEB method[42] was implemented in the DL-FIND code[43] using an in-house interface with the Gaussian program to split NEB image calculations across the nodes of the computational cluster. The same method, functional, and basis set that were used in the electronic structure

optimizations were also used in NEB calculations. The chemical nature of all transition states was confirmed by intrinsic reaction coordinate (IRC) reaction path calculations.[44, 45]

3.6 Calculation of the absorption spectra

The absorption spectra of nanoclusters is characterized by the vertical excitation energies, according to the Franck-Condon principle. The Franck-Condon principle states that, because nuclear masses are so much larger than the mass of an electron, an electronic transition occurs within a stationary nuclear framework. As a result, the nuclear locations remain unchanged during the actual transition, but then readjust once the electrons have adopted their final distribution.[46] The vertical excitation energies correspond to the energy difference between the excited state and the ground state potential energy curves at the minimum point of the ground state geometry.

The **oscillator strength**, *f*, expresses the probability of light absorption in electronic transitions between the energy levels of an atom or molecule. From *Fermi's golden rule*, within the *dipole approximation*, the oscillator strength of an electronic transition is

$$f = \frac{2}{3}\frac{m_e}{\hbar^2}(E_f - E_i)|\mu|^2 \tag{3.6}$$

where m_e is the mass of the electron, (E_f - E_i) is the electronic excitation energy, and μ is the transition dipole moment. The total transition dipole moment of an electronic transition from an initial state to a final state, within the Franck-Condon and Born-Oppenheimer approximations, is:

$$\mu =< \Psi_f^e|\mu_e|\Psi_i^e >< v_f|v_i > \tag{3.7}$$

where $<{\Psi_f}^e|\mu_e|{\Psi_i}^e>$ is the electronic transition dipole moment; v_i and v_f are the nuclear vibrational wave functions of the initial and final states, respectively; and $<v_f|v_i>$ is the Franck-Condon factor.

The simulation of the absorption spectra of nanoclusters usually involves two steps:

- Perform a structural optimization to obtain the minimum energy geometry of the system at a given level of theory.
- Calculate the vertical electronic excitation energies and the corresponding oscillator strengths using the TD-DFT method at the same level of theory .

The B3LYP functional was used with the same basis set for TD-DFT calculations for the absorption spectra.[32] The reported optical gaps correspond to the excitation energies for the first allowed transition.

Chapter 4

Theoretical Results and Discussions

4.1 Properties of aromatic silicon nanoclusters

4.1.1 Toward global minimum energy structures

A plasma operating close to dusty particle formation is, in general, not expected to yield global minimum energy structures.[47] From AIMD simulations of the silicon cluster growth in low temperature silane/hydrogen plasmas, the self-assembly of the highly-symmetric *metastable* $Si_{19}H_{12}$ isomer A (see Figure 2.1) was observed.[21, 22] Although being metastable, its local minimum energy configuration survives even after heating the structure to extremely high temperatures exceeding 1000K. Indeed, the origin of this astonishing stability of these clusters, is attributed to electron delocalization induced by electron-deficient bonds.

Simulations have shown the transformation of metastable plasma-born silicon nanoclusters to extremely stable, also over-coordinated, but *irregular* ones (as for instance, isomer C of $Si_{19}H_{12}$, shown in Figure 4.1) under the influence of atomic and molecular hydrogen.[21, 48] In the present work, we present another highly stable structure with a $Si_{19}H_{12}$ stoichiometry, obtained using a different technique. The symmetric $Si_{19}H_{12}$ cluster (isomer A) was heated using a thermostat until it became liquid then it was cooled down to zero Kelvin. Finally, the structure was optimized at high-levels of theory as described in Chapter [3]. The resulting isomer D (see Figure 4.1) is 3.52 eV more stable than the symmetric, nontetrahedral nanocrystal, isomer A. At this instant, we would like to insist that isomer D, *the presently most stable structure*, does not necessarily correspond to a global minimum energy structure; *i.e.*, there might be still more stable isomers yet to be explored.

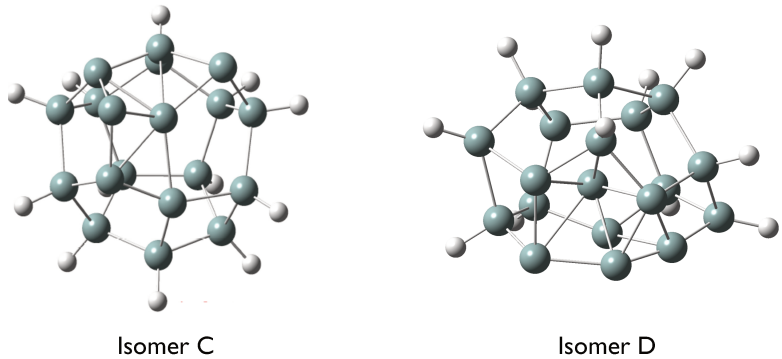

Figure 4.1: The geometrical structure of different isomers of $Si_{19}H_{12}$. *Left*: Isomer C obtained after heating isomer A through exposure to hydrogen atoms and subsequent cooling with hydrogen molecules, and then optimizing the final structure.[47] *Right*: Isomer D obtained after heating isomer A by means of a thermostat, then slowly cooling down to zero Kelvin and optimizing the final structure.

4.1.1.1 Stability of different nontetrahedral $Si_{19}H_{12}$ isomers

In the following, we compare the stability of different nontetrahedral $Si_{19}H_{12}$ isomers to the extremely over-coordinated $Si_{21}H_{12}$ nanocrystal[47] and to two nearly perfectly tetrahedral clusters: the $Si_{20}H_{20}$ fullerene and the experimentally synthesized and patented $Si_{29}H_{24}$ nanocluster.[49–52] To compare the stability of hydrogenated silicon clusters with different stoichiometries, we define a cohesive skeleton energy, $E_{coh,sk}$, that is based on the method proposed by Zdetsis[53] and that includes the influence of zero-point energies for the H atoms:[54]

$$E_{coh,sk} = \frac{[BE(Si_nH_m) + m \cdot \mu(H) - m \cdot ZPE(H)]}{n} \tag{4.1}$$

where $BE(Si_nH_m)$ is the total binding energy or atomization energy of the hydrogenated silicon cluster. The chemical potential for hydrogen, μ *(H)*, is chosen to be the negative value of the Si-H binding energy calculated as one-quarter of the silane molecule binding energy;[53] that is, -3.27 eV per H atom at the MP2/6-311++G(d,p) level of theory. Northrup estimated the zero-point energy, ZPE(H), to be 0.21eV per H atom.[55]
Table (4.1) shows that isomer D is the presently most stable structure. All the investigated structures turn out to be more stable than the $Si_{20}H_{20}$ fullerene and there are only two of the investigated over-coordinated $Si_{19}H_{12}$ isomers that are slightly less stable than the perfectly tetrahedral $Si_{29}H_{24}$ cluster despite its considerably larger size.

Table 4.1: Summary of the skeleton energies for different hydrogenated silicon clusters.

Cluster	$\mathbf{E}_{coh,sk}$[eV/atom]
$Si_{19}H_{12}$ **Isomer A**	2.9587[47]
$Si_{19}H_{12}$ **Isomer B**	3.0282[47]
$Si_{19}H_{12}$ **Isomer C**	3.1043[47]
$Si_{19}H_{12}$ **Isomer D**	3.1439
$Si_{21}H_{12}$	3.0742
$Si_{29}H_{24}$	3.0565
$Si_{20}H_{20}$	2.8481

4.1.2 Electron-deficiency in silicon nanoclusters

A detailed NBO analysis of isomer D at the MP2/6-311++g(d,p) level of theory reveals:

- Severely electron-deficient bonds (down to 1.46 electrons per bond)
- Different hybridization states (between sp^2 and sp^{28})
- Strong stabilization energies (up to 62 kcal mol^{-1})

4.1.3 Magnetically induced ring current

Isomer D shows a high net diamagnetic aromatic ring current of 41.6 nAT^{-1} (see Figure 4.2) which is quite comparable to the one of the symmetric nanocrystal (isomer A) of 42.0 nAT^{-1}, while the corresponding value for benzene is only 12.9 nAT^{-1}, Figure 4.3. It is worth noting that relatively strong electric currents of isomer D can be induced for any arbitrary orientation of the nanocluster relative to the magnetic field; *i.e.*, contrary to benzene, it is no longer necessary to have a magnetic field perpendicular to a given molecular plane. Figure 4.3 also demonstrates the similitude between the magnetically induced current lines for benzene and those for the $Si_{19}H_{12}$ (isomer A). Moreover, isomer D shows high magnetic shielding values (NICS) up to -27 ppm similar to the NICS values of isomer A that exceed those of benzene by a factor of about three.[19]

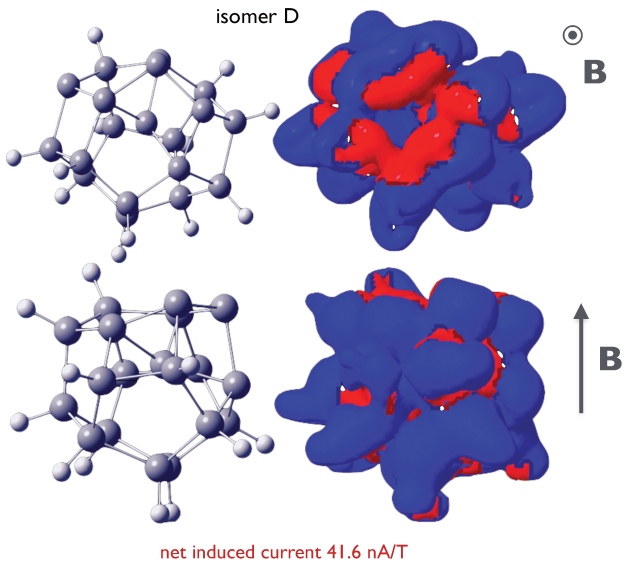

Figure 4.2: Signed modulus of the magnetically induced current densities of isomer D of the $Si_{19}H_{12}$. Top and side views are shown. Diatropic currents are depicted in blue and paratropic currents in red. For the top view images, the applied magnetic field is normal to the image plane, while it is in the image plane pointing to the top for the side view of the bottom images. Despite some apparently unruly mixing of para- and diamagnetic components in space, integration over all currents yields a net diamagnetic aromatic ring current of 41.6 nA/T.

4.1.4 Electron localization function

In the following, we would like to visualize in which regions of the nanocluster the electron delocalization becomes dominant.

4.1.4.1 Two dimensional ELF plots of isomer A in comparison with C_6H_6

As can be seen in Figure 4.4, the ELF for the top hexagon plane of the $Si_{19}H_{12}$ nanocrystal shown in Figure 4.4-b (that looks quite identical to the one of the bottom hexagon which is not depicted here) bears some resemblance to the ELF of the benzene molecule in Figure 4.4-a. For the former, however, the electrons between adjacent Si atoms appear to be more localized and there is less delocalization all over. For the central hexagon shown in Figure 4.4-c, however, the apparent delocalization as expressed by the ELF already exceeds the one of benzene. In the plane just between this central hexagon and the endohedral Si atom, the delocalization becomes yet more important (see Figure 4.4-d). This trend continues when going to the plane of the endohedral Si atom where the ELF becomes similar to the one of a homogeneous electron-gas (*i.e.* about 0.5, see Figure 4.4-e).

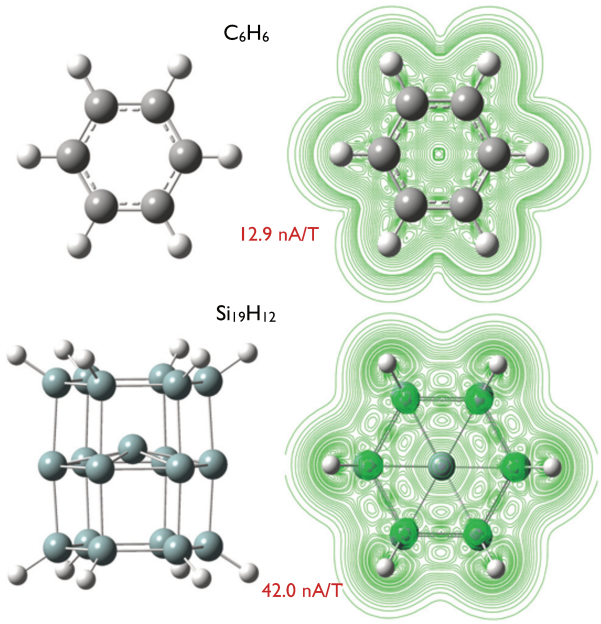

Figure 4.3: Magnetically induced current lines for benzene C_6H_6 in comparison with those for the highly-symmetric $Si_{19}H_{12}$ isomer A. Note that the latter ones were recorded 1 Bohr below the nanocrystal.

The conclusion that the electron delocalization in the $Si_{19}H_{12}$ nanocrystal becomes dominant around the endohedral Si atom is in excellent agreement to the stabilization energies that become most pronounced for bonds involving the overcoordinated endohedral Si atom.[19] We would also like to remark that there are no obvious ELF attractors between the endohedral Si atom and its neighbor atoms demonstrating how loosely this atom is bound enabling its usage in THz nano-oscillators.[56] Finally, the extreme electron delocalization as visualized with ELFs helps us to understand better how the sum of stabilization energies can be so much higher for the $Si_{19}H_{12}$ nanocrystal than for benzene. Therefore, we like to suggest that "ultrastability" induced by electron-deficient bonds can cause a much larger extend of stabilizing electron delocalization than "extrastability"of the classical multibond aromaticity.

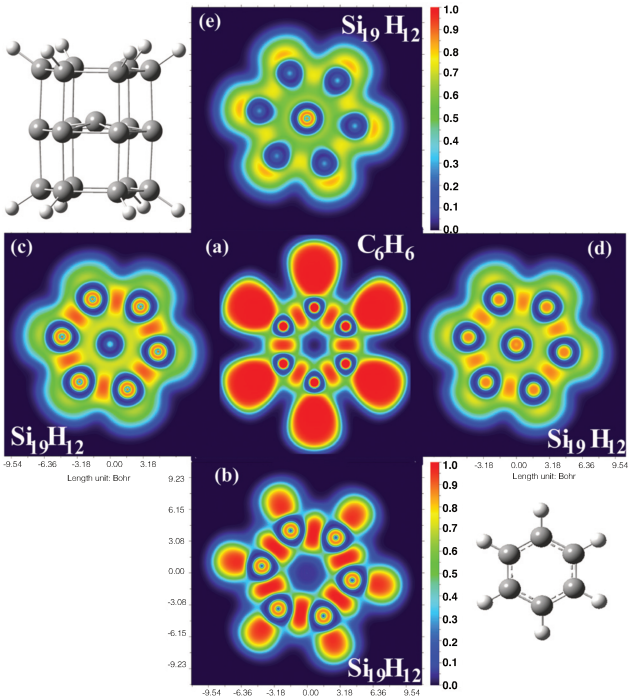

Figure 4.4: ELF plots in different planes for the $Si_{19}H_{12}$ nanocrystal (isomer A) and for C_6H_6. (a) for benzene as a reference molecule; (b) in the top hexagon; (c) in the center hexagon; (d) in the plane between the central hexagon and the endohedral Si atom; and (e) in the plane of the endohedral Si atom of the highly-symmetric $Si_{19}H_{12}$ cluster.

4.1.4.2 Two-dimensional ELF plots of isomer D

In analogy to our ELF analysis of above for the symmetric $Si_{19}H_{12}$ nanocrystal, we explored electron delocalization for isomer D and summarized our findings in Figure 4.5. In the shown examples, there are only a few Si atoms that are held together with fully localized electrons (dark red color), but often several Si atoms share electrons that are better described as being in the state of a homogeneous electron gas (green-blue). All of these results nicely support our previous conclusion based on the high magnetically induced ring currents that the electrons of isomer D are strongly delocalized and that this isomer can be considered as highly aromatic in the sense of electron-deficiency aromaticity[19] despite its ill-defined structure.

4.1.4.3 Two-dimensional ELF plots of isomer D in comparison with small metal clusters

Due to the electron deficient nature and the extensive electron delocalization demonstrated above for $Si_{19}H_{12}$ clusters, we like to present here a comparison between their ELF plots and those of some typical small metal clusters. As can be seen in Figure 4.6, the most noble of the chosen metal clusters is clearly the pyramidal gold cluster, Au_{20}, since it does not exhibit any ELF attractors

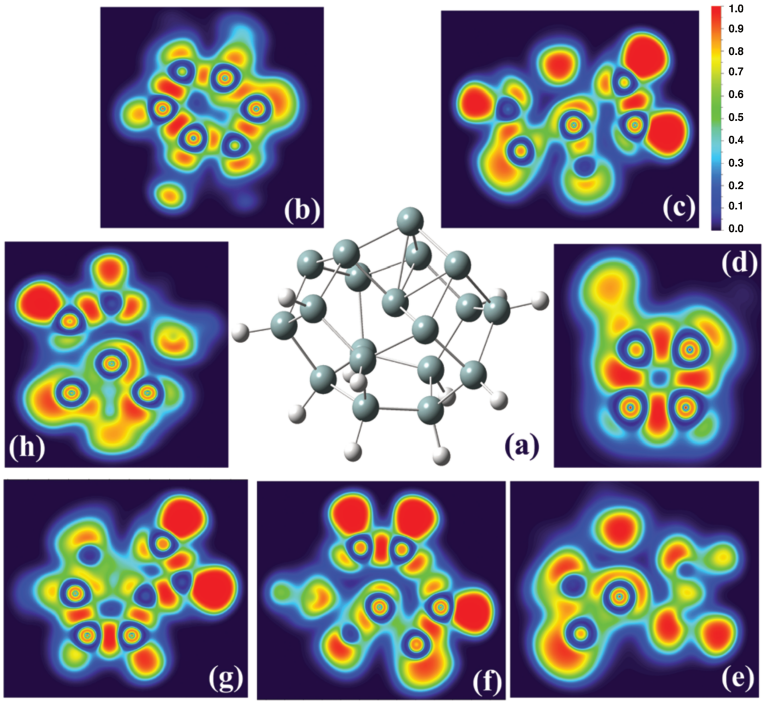

Figure 4.5: ELF plots in different planes for the presently most stable isomer D. (a) Structure of isomer D. Note that relatively few Si-Si bonds in those examples can be characterized by a fully localized-electron bounding scheme corresponding to an ELF value of 1.0 (dark red) as for example one bond in (c) and one in (f); often the ELF values do not exceed 0.5 between neighbor Si atoms as for example in (e), (f), (g), and (h).

between adjacent gold atoms at all.[57, 58] As in the bulk material, we readily recognize where the image of an "electron sea"comes from. For the lead cluster,[59] however, the appearance of green color in between the atoms; *i.e.* an ELF value of about 0.5, indicates a behavior comparable to a homogeneous electron gas. The same observation holds for the symmetric $Si_{19}H_{12}$ nanocrystal (see for instance Figure 4.4-e). For the lithium cluster,[60] the electron localization scheme looks quite comparable to the one of isomer D; *i.e.*, the electrons between only few Si atoms are highly localized as they are in silicon bulk materials whereas most bonds can be characterized by much less localized electrons showing strong resemblance especially with the non-noble metal clusters. The latter bonding scheme seems to be more pronounced in asymmetric hydrogenated silicon clusters explaining their superior stabilities over the highly symmetric ones.

4.1.5 Nudged elastic band calculations

Since all $Si_{19}H_{12}$ isomers studied seem to exhibit quite similar characteristics, we used NEB calculations to map out the potential energy profile between the symmetric nanocrystal, isomer A, and isomer D. The result is displayed in Figure 4.7 and clearly shows the wealth of possible asymmetric isomers that are more stable than the initial nanocrystal.

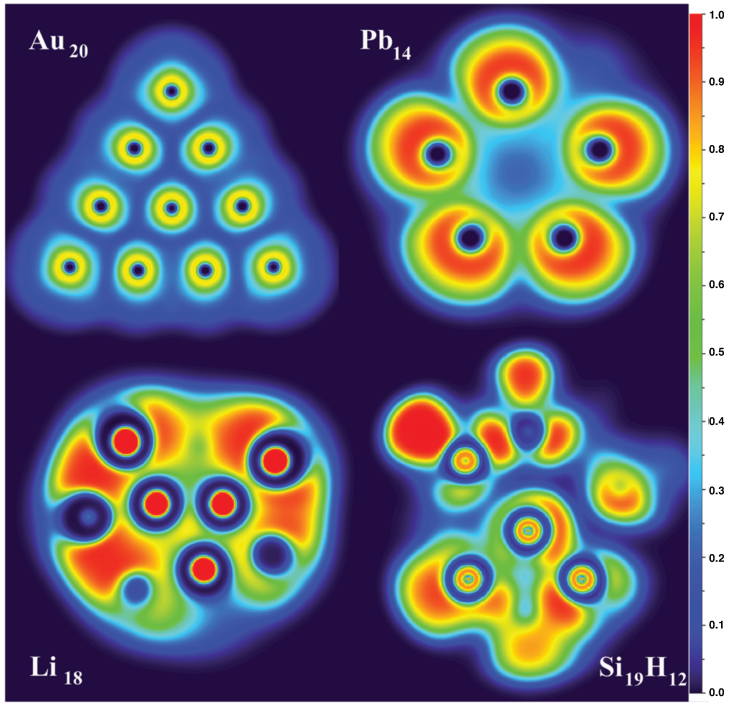

Figure 4.6: ELF plots for three small metal clusters in comparison with isomer D.

The height of the first transition state as displayed in Figure 4.7 shows that once isomer A is formed in the reactor, it can survive in the plasma a sufficiently long time for applications since all particles in the plasma only possess thermal energies (*i.e.* around 0.026 eV).[23] Nevertheless, the transition states of 0.28 eV and 0.83 eV might actually overestimate the barrier height for the highly symmetric nanocrystal to lose its structure since in previous AIMD simulations the initial structure was lost at temperatures above 1000 K and the phase transition to the liquid state happened at about 1550 K which is quite close to the melting point for bulk silicon of 1687 K. Those temperatures are very high, but yet considerably lower than the transition state estimates. This finding is also confirmed by previous semi-emperical PM3 molecular dynamics simulations which proved that only at temperatures between 1000 K and 2000 K, the symmetric structure is lost starting by the breaking apart of the central Si hexagon.[21]

4.1.6 Calculated absorption spectra

In Figure 4.8, we show the calculated absorption spectrum of isomer D and one other member of the $Si_{19}H_{12}$ scaffold. In contrast to the absorption spectrum of the classical tetrahedral cluster, the $Si_{20}H_{20}$ fullerene, that only absorbs in the UV region (Figure 2.2), both isomers extend their absorption spectrum from the UV to the visible until the IR spectral regions. This optical characteristic can readily be explained by the delocalized nature of their electronic structures. Delocalized electrons are less tightly bonded to their chemical structure than localized ones.

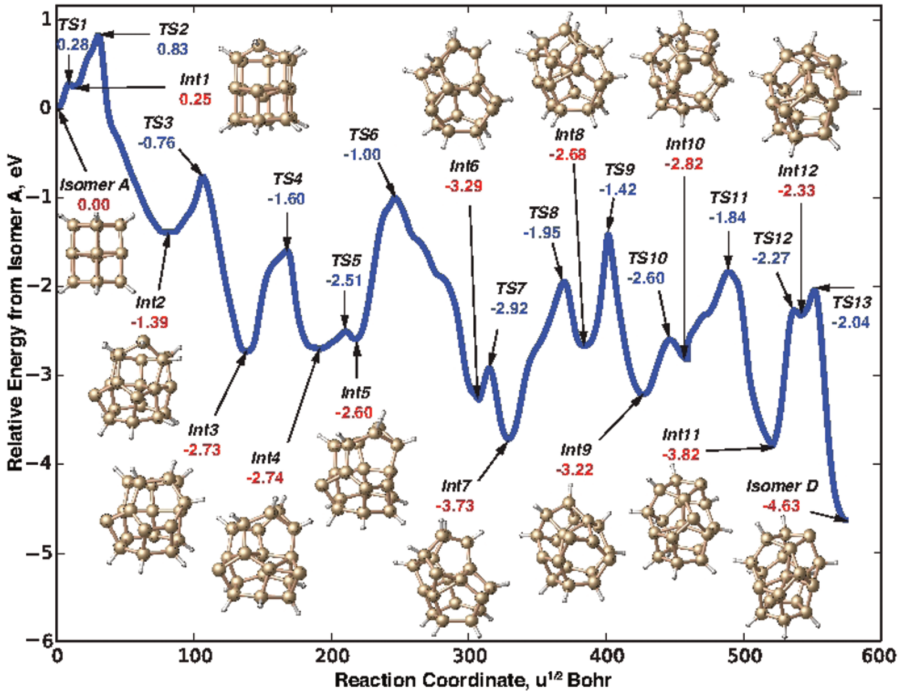

Figure 4.7: $Si_{19}H_{12}$ scaffold resulting from a Nudged Elastic Band calculation between the initial $Si_{19}H_{12}$ nanocrystal, isomer A, and isomer D. Red and blue numbers show the energies of stable isomers and transition state structures, respectively, relative to isomer A.

Therefore, it is well known that the absorption spectra of chemical compounds shift to longer wavelengths as their degree of aromaticity increases.[61]

At this point, we would like to note that the calculated absorption spectra of different hydrogenated silicon clusters with comparable sizes have shown huge changes in the optical gap between 1.0 eV and 5.2 eV (see Table (4.2)) as a result of minor changes in the geometrical structure and/or the degree of hydrogenation, permitting the absorption of photons of most of the solar spectrum.

4.2 Silicon cluster band gap engineering

Detailed inspection of the images in Figure 4.7 reveals that all local minimum energy structures possess highly electron-deficient bonds, high magnetic shielding, and strong magnetically induced aromatic ring currents; *i.e.*, all shown $Si_{19}H_{12}$ isomers are ultrastable and aromatic. In fact, it does not really matter which one of those isomers is the very most stable one since all of them are sufficiently stable for applications. Those applications are far reaching since all members of this new family of semiconductor nanoclusters have astonishing new features due to their delocalized electrons, their extremely long Si-Si bonds, and their metallic-like bonding schemes. While all

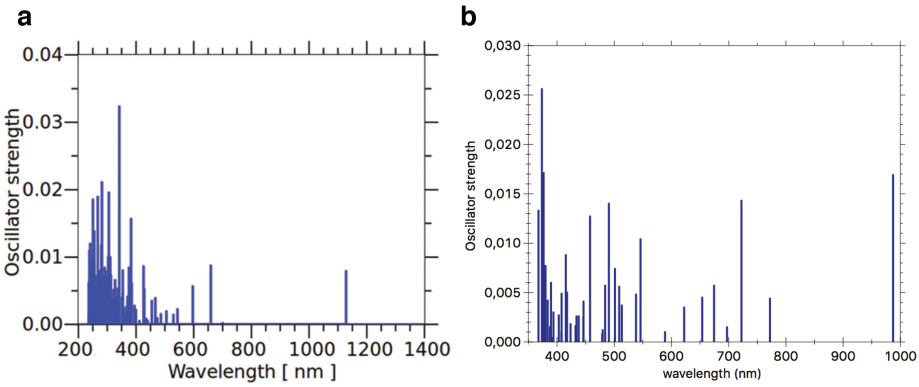

Figure 4.8: Absorption spectra calculated for two isomers of the $Si_{19}H_{12}$ nanocluster. (a) isomer D and (b) one other member of the $Si_{19}H_{12}$ scaffold.

Table 4.2: Summary of the optical gaps for different hydrogenated silicon clusters.

Cluster	**Optical Gap (eV)**
$Si_{19}H_{12}$ **Isomer A**	0.993[47]
$Si_{19}H_{12}$ **Isomer B**	1.610[47]
$Si_{19}H_{12}$ **Isomer C**	1.468[47]
$Si_{19}H_{12}$ **Isomer D**	1.098
$Si_{21}H_{12}$	1.121
$Si_{29}H_{24}$	3.588
$Si_{20}H_{20}$	5.150

presented isomers have quite comparable characteristics, their precise quantitative properties; as optical gaps and dipole moments, vary sufficiently to make them ideal candidates for efficient, non-toxic, and inexpensive bandgap engineering.

As an example, we demonstrate in Figure 4.9 how the wavelength-dependent absorption in the active layer of photovoltaic devices can be improved by the incorporation of non-tetrahedral hydrogenated silicon clusters. To this end, we have added aromatic clusters, as the ones discussed above, to the a-Si:H layer of a standard solar cell. For the modeling of the transparent conductive oxide (TCO) electrode, we have considered the optical transmittance of a ZnO:Al thin film with a thickness of 547 nm. While Figure 4.9 is simply based on a random selection of aromatic clusters with different structures, the precise shape of the resulting absorption curve can be tailored to specific needs through the appropriate choice of specific clusters, their respective densities, and the employed electrode.

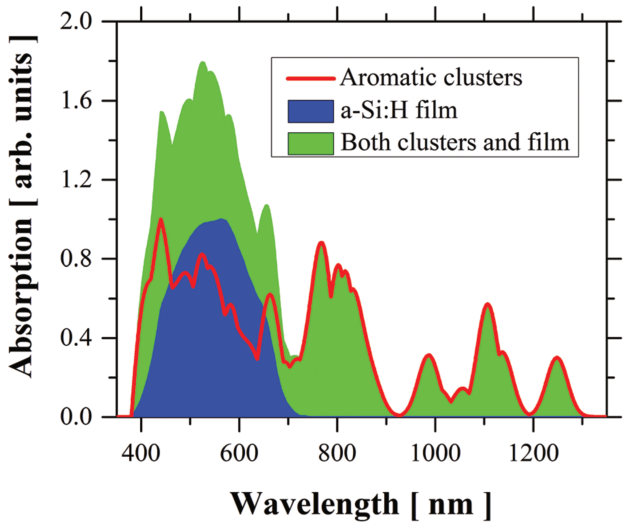

Figure 4.9: Absorption spectrum calculated for the active solar cell layer. Enhancement of the spectral absorption in the active solar cell layer based on the addition of self-assembled aromatic Si nanoclusters to the amorphous silicon (a-Si:H) layer of a standard solar cell with a TCO electrode.

4.3 Conclusion

Based on AIMD simulations, we have shown that small nanoclusters of about 1 nm size spontaneously generated in a low-temperature silane plasma do not possess tetrahedral structures, but are ultrastable. Apparently small differences in the cluster structure result in substantial modifications in their electric, magnetic, and optical properties, without the need for any dopants. Their nontetrahedral geometries notably lead to electron deficient bonds that introduce efficient electron delocalization that strongly resembles the one of a homogeneous electron gas leading to metallic-like bonding within a semiconductor nanocrystal. As a result, pure hydrogenated silicon clusters that form by self-assembly in a plasma reactor possess optical gaps covering most of the solar spectrum from 1.0 eV to 5.2 eV depending simply on their structure and, in turn, on their degree of electron delocalization. This feature makes them ideal candidates for future bandgap engineering not only for photovoltaics, but also for many nano-electronic devices employing nothing else but Si and H atoms.

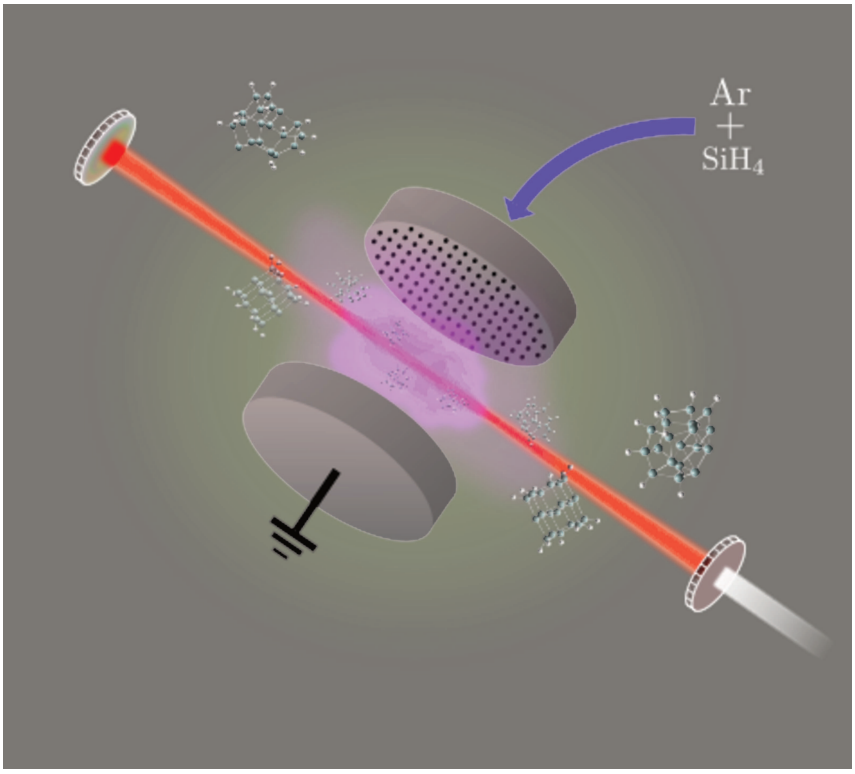
Ar
+
SiH4

Chapter 5

Applied Experimental Techniques: An Overview

Experimental studies were performed to measure the optical absorption of plasma-born aromatic silicon nanoclusters *in situ*, to investigate their permanent dipole moment character and to study the structure of deposited nanoclusters. We start the experimental section by providing a short overview of the capacitively coupled discharge and cavity enhanced absorption spectroscopy in order to guide the reader through the different topics treated in the following chapters.

5.1 Capacitively coupled discharge

A plasma is a partially ionized gas with a combination of free electrons, ions, radicals, and neutral species. Plasmas are often called the fourth state of matter. In nature, a plasma is formed when gas is exposed to high temperatures or subjected to high energy radiation such that the atoms decompose into freely moving charged particles.[62] However, to create and sustain a plasma in the laboratory, energy input is required. Generally, this energy is transferred *via* coupling of an external electromagnetic field to the gas. Different coupling methods generate plasmas with different characteristics.

One of the widely used coupling methods is the one for capacitively coupled plasmas (CCP). A CCP system consists of two parallel plate electrodes separated by a small distance and embedded in a vacuum chamber as illustrated in Figure 5.1. The gap between the electrodes is filled with gas. The vacuum chamber and one of the electrodes are electrically grounded while the other electrode is powered *via* an impedance matching network. The energy is supplied as a voltage difference between the cathode and the grounded plate in a time-varying manner. Most commonly, a RF voltage is applied to the plates with an operation frequency of 13.56 MHz.[1] Electrons play a significant role in RF discharges. The electrical energy supplied by the

[1] 13.56 MHz is a band reserved for the Industrial Scientific and Medical Frequencies (ISM) which does not interfere with radio and television broadcasting bands. The authorities in charge of the management frequency ranges are the "Authority of Regulation of Telecommunications"and "European Radiocommunications Office".

generator is converted by the electrons into chemical reactions, such as excitation, ionization, and dissociation of gas molecules, creating the plasma. The matching network guarantees an efficient power coupling into the plasma by matching the impedance of the discharge setup to the output impedance of the RF voltage generator; *i.e.* it minimizes the reflected power, ensures an optimal energy transfer to the plasma, and protects the generator.

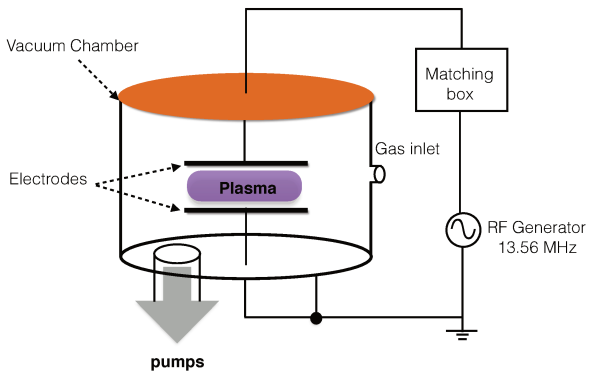

Figure 5.1: A typical capacitively coupled plasma setup.

As soon as the plasma is ignited, a positive net charge region emerges at the interface between the plasma bulk and the surfaces of the electrodes, the so-called *sheath* region (see Figure 5.2). The sheath results from the difference in thermal motion of electrons and ions. Electrons have smaller mass and higher mobility compared to ions and, thus, a significantly higher thermal flux. So, in a very short time-scale, the electrons will flow quickly to the electrode and form a negative charge on the surface leaving behind a layer of positive ions. In order to satisfy the condition of a zero-net flux at the surfaces, the plasma potential rises relative to the surfaces. The potential drop across the sheath slows down the electrons to reduce their flux. The resulting potential difference between the electrodes and the plasma creates an intense electric field pointing from the plasma to the electrodes that would accelerate the positive ions across the sheath potential drop to the surface of electrodes.[62] In practice, the discharge is not ideally symmetric and its symmetry is generally determined by the electrode surface areas. The grounded surface is typically larger than the powered one, since apart from the *real* electrodes, all other surfaces exposed to the plasma are grounded. This creates a highly asymmetric discharge with a larger voltage drop between the plasma and the powered electrode. Consequently, a DC self-bias voltage, V_b, develops at the powered electrode with respect to the ground, as illustrated in Figure 5.2. It is important to point out here that the bias voltage is also due to the blocking capacitor placed in the matching box. The bias voltage is mainly negative resulting in an enhanced ion impact on the powered electrode.

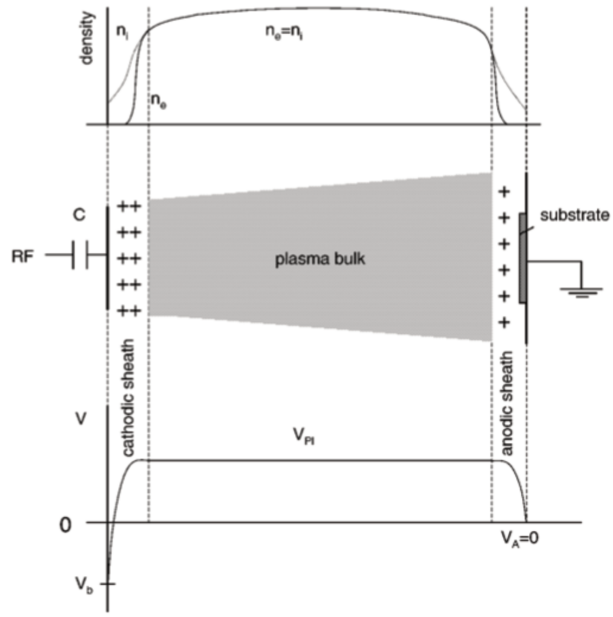

Figure 5.2: Scheme of an RF discharge in a parallel-plate reactor with capacitive coupling of the RF generator. The spatial distributions of the potential V (plasma potential V_{pl}, bias voltage V_b, and anode voltage V_A) and electron and ion densities (n_e, n_i) are also shown.[63]

5.1.1 Plasma enhanced chemical vapor deposition

Plasma enhanced chemical vapor deposition (PECVD) is a standard deposition method, based on a CCP process, and is widely applied by industrial amorphous hydrogenated silicon solar module producers, for example. In a PECVD method, the produced gas precursors contribute to the growth of a thin film on a chosen substrate. Major steps of a PECVD process include the source gas diffusion, electron impact dissociation, gas-phase chemical reactions, and radical diffusion and deposition. Indeed, the film growth and the resulting deposited material properties are highly dependent on the plasma characteristics, such as the power density, the gas flow, the deposition pressure, the excitation frequency, *etc.*[64]

5.1.2 Pulsed excitation

Studies have shown that the modulation of the RF signal of PECVD systems has very important effects on both particle formation in the gas phase and the deposition process.[65] The discharge can be modulated by a square-wave frequency variable ranging from 10^{-1} to 10^4 Hz. Under such conditions, the plasma periodically switches, between on and off, at the specified frequency. The modulation parameters will be the pulse period (the time between two successive plasma

ignitions) or the corresponding pulse frequency, and the duty cycle which indicates the percentage of the period in which the plasma is switched on, as illustrated in Figure 5.3.

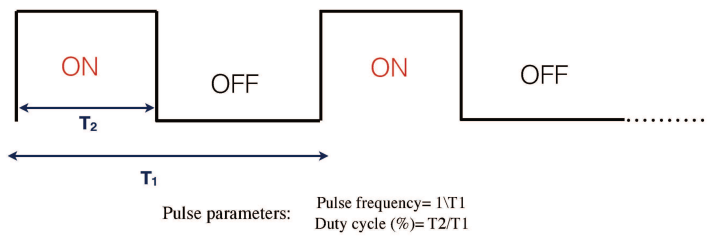

Figure 5.3: Pulsed excitation parameters. The pulse frequency and the duty cycle.

5.1.3 How does the temperature affect the growth of nanoparticles?

Experimental studies have shown that the gas temperature plays a significant role during the different growth stages of the particles.[26] Increased temperature slows down the growth kinetics; especially the first phase (formation and accumulation of nanocrystallites) becomes *longer*. Figure 5.4 shows how the agglomeration phase that started after 100 ms at RT is delayed to 6 s at 150°C. Fridman *et al.*[66] explained this delay with temperature increase as follows: The generation of the first supersmall particles begins with SiH_3^- negative-ion formation by dissociative attachment.[67] Then, the negatively charged growth proceeds with ion-molecular reactions, such as $SiH_3^- + SiH_4 \rightarrow Si_2H_5^- + H_2$, $Si_2H_5^- + SiH_4 \rightarrow Si_3H_7^- + H_2$, and so on. This chain of reactions, after $Si_5H_{11}^-$, is activated by the vibrational excitation of silane molecules in a plasma. However, when the temperature of the gas is increased, relaxation (from vibrational to translational excitation) will take place. For this reason, a small increase in the gas temperature results in reduction of the vibrational excitation level of the silane molecules, and makes all the reactions necessary for cluster growth much slower.

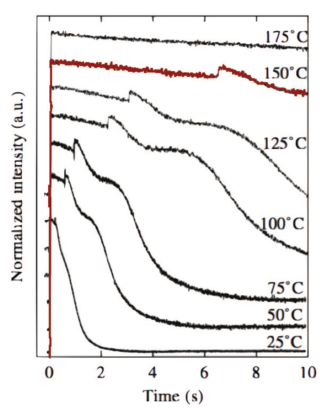

Figure 5.4: Time evolution of the amplitude of the third harmonics for different gas temperatures.[26]

The selection of the gas temperature is, thus, crucial in our experiments for the following reasons: (i) we want to generate silicon nanoclusters of ∼1nm only, and (ii) we want to ensure that all the optical absorption measurements are done before the agglomeration phase begins.

5.1.4 After-glow forces acting on particles

When a plasma is switched off, particles will no longer remain trapped in the discharge by the confining electric fields. Different forces will act on the particles affecting their dynamics:[68]

- Gravitational force

$$F_g = \frac{4}{3}\pi r_p^3 \rho g \tag{5.1}$$

  where ρ and r_p are the mass density and radius of a particle, respectively.

- Neutral drag force (Gas flow)

$$F_{nd} = -\frac{4}{3}\pi r_p^2 m_n n_n v_{th} \left(1 + \alpha\frac{\pi}{8}\right)(\mathbf{v}_p - \mathbf{v}_n) \tag{5.2}$$

  where m_n, n_n, $v_{th} = \sqrt{8k_B T_n/\pi m_n}$ are the mass, density and thermal speed of neutrals (T_n being the gas temperature), respectively; v_p is the particle velocity; v_n is the neutral mean speed; and α is the accommodation coefficient.

- Thermophoresis forces pushing particles away from hot surfaces

$$F_T = -\frac{32}{15} r_p^2 \frac{k_{tr}}{v_{th}} \nabla T \tag{5.3}$$

  where k_{tr} is the translational part of the thermal conductivity and ∇T is the temperature gradient.

5.2 Optical Absorption Spectroscopy

When light is transmitted through a medium (solid, liquid, or gas), it experiences attenuation due to absorption and scattering; the former being the dominant loss contribution in many cases. This is the basic principle behind most absorption spectroscopy techniques: illuminate a sample with a light source of known intensity and measure the amount of light transmitted through the sample to a detector on the far side. The difference in intensity between the incident light intensity, I_0, and transmitted light intensity, I (x, λ), yields the absorbed light, ΔI = I_0 - I (x, λ), which Beer's law relates to the absorbance of the sample, α (λ), as:[69]

$$I(x, \lambda) = I_0 e^{-\alpha(\lambda)x} \tag{5.4}$$

where λ is the wavelength and x is the path length. The absorption coefficient α (λ) is related to the molecular concentration of the target sample, C, and the extinction coefficient, ϵ (λ), namely, α (λ) = $C\epsilon$ (λ).

When employing absorption spectroscopy, it is important to ensure *sensitivity*. Sensitivity can be quantified as a minimum detectable absorption loss, *i.e.* the normalized standard deviation of the smallest detectable change in absorption. The minimum detectable absorption is reached when the transmitted light intensity change due to absorption is smaller than the intensity fluctuations inherent to the light source. Equation (5.4) shows that the absorption is intensity dependent and its sensitivity linearly depends on the optical path length. This is often the reason to use optical cavities with high reflective mirrors inside them; *i.e.* the cavity enhanced absorption method. This method enlarges the path length of the light, increasing the possibility of matter-light interaction and thus the measured signal. A variety of cavity enhanced absorption methods are used in absorption spectroscopy, as for instance, integrated cavity output spectroscopy, incoherent broadband cavity enhanced absorption spectroscopy (IBBCEAS), continuous wave cavity ring-down spectroscopy, and so on. All of the above mentioned methods utilize light reflection by mirrors to enhance the optical path length and increase the sensitivity while maintaining a small resonator size.

5.2.1 Incoherent broadband cavity enhanced absorption spectroscopy

A basic IBBCEAS setup consists of an incoherent light source (*e.g.* a Xenon arc lamp, a light emitting diode, or a supercontinuum source[2]), collimation optics, an optical cavity, the absorber of interest, and a detector.[70] Light is passively coupled into a stable optical cavity, of length $\boldsymbol{d}$, formed by two identical high reflectivity mirrors (R_1=R_2=$\mathbf{R}$ > 99.9%) with losses L (see Figure 5.5). The incoherent source is spectrally *filtered* to match the bandwidth of the high reflectivity cavity mirrors. Due to the high reflectivity of the mirrors, effective absorption path lengths can reach a few *kilometers*. Light transmitted through the cavity is detected using a monochromator-charge coupled device (CCD) combination interfaced with a computer[3].

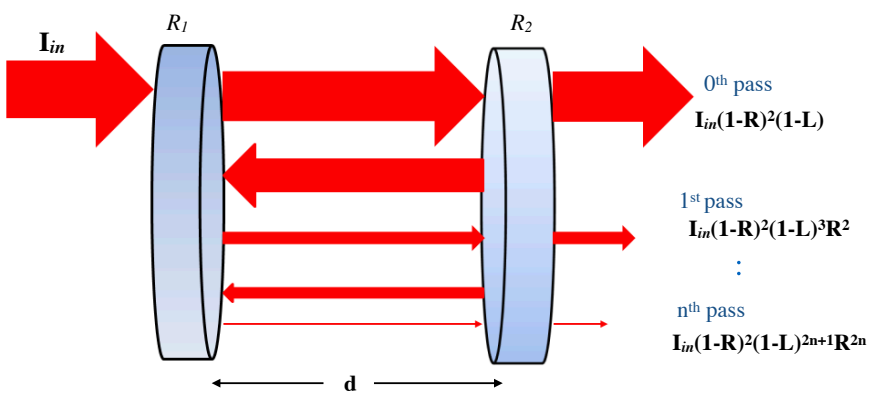

Figure 5.5: Schematic illustration of light passing through an optical cavity in IBBCEAS. Our cavity having a length **d** of 1m approximately could create an effective path length of 10 km due to the high reflectivity mirrors.

[2]A brief introduction to the supercontinuum light source is presented in Appendix D.
[3]A full description of our experimental setup is presented in Chapter [6].

5.2.1.1 IBBCEAS measurement principle

Consider an optically stable cavity continuously excited with incoherent light of intensity I_{in} (Figure 5.5). Apart from the losses $(1-R)$ due to imperfect mirror reflectivities, it is assumed that the cavity is subject to additional losses $(1-L)$ per pass. The intensity of the light transmitted by the cavity, I, can then be described by the superposition of the light after an *odd* number of passes, n, leading to the following infinite sum[70]:

$$I = I_{in}(1-R)^2(1-L)\sum_{n=0}^{\infty} R^{2n}(1-L)^{2n} \tag{5.5}$$

Since $R<1$ and $L<1$, the geometric series converges and Eq. (5.5) can be written in the form

$$I = I_{in}\frac{(1-R)^2(1-L)}{1-R^2(1-L)^2} \tag{5.6}$$

For an empty resonator with $L=0$, the time integrated transmitted intensity I_0 is given by

$$I_0 = I_{in}\frac{1-R}{1+R} \tag{5.7}$$

Assuming the losses per pass to be solely due to Lambert-Beer attenuation and after applying some approximations[4], the absorption coefficient, ϵ, can finally be expressed by the following equation:

$$\epsilon(\lambda) = \frac{(1-R(\lambda))}{d}\left[\frac{I_0(\lambda)}{I(\lambda)} - 1\right] \tag{5.8}$$

where the absorption coefficient $\epsilon(\lambda)$ [cm^{-1}] is sometimes referred to as extinction coefficient as one cannot distinguish between absorption and scattering losses; $I_0(\lambda)$ and $I(\lambda)$ are the intensity of light transmitted by the cavity **without** and **with** a sample in the cavity, respectively.

The reflectivity of the mirrors, $R(\lambda)$, are accurately determined. This is usually accomplished by measuring the reflectivity as a function of wavelength using known concentrations of a *calibration sample*.

[4] Assuming small losses per pass, $L\rightarrow 0$, and high reflectivity mirrors, $R\rightarrow 1$.

Chapter 6

Performed Experiments and Diagnostics

Due to the expectedly broad absorption features of silicon nanoclusters in the visible wavelength region of interest, and the potentially low concentration of particles in the sample region of the reactor, IBBCEAS is an optimum technique to detect the extinction in the chamber.

6.1 Experimental setup

In our experiment, a CCP reactor for the production of hydrogenated silicon nanoclusters was combined with a cavity enhanced absorption setup as a diagnostic tool. The components of the setup are shown schematically in Figure 6.1. The general experimental conditions and procedures are described below.

6.1.1 Plasma reactor

Inside a ~ 0.02 m^3 vacuum chamber, an RF (13.56 MHz) CCP discharge was generated (Cesar 133 RF power supply) at low pressure between a grounded and a powered electrode. The circular electrode surfaces had a diameter of 7 cm and were separated by 4 cm. The shower-head shape of the powered electrode allowed the injection of a gas mixture of silane (2%) in argon (98%) directly between the electrodes, in order to produce hydrogenated silicon nanoclusters in a pulsed discharge. The flow rate of the SiH_4/Ar mixture was controlled by a mass flow controller (MFC-Bronkhorst F-201DV, Low-ΔP-Flow), which was operated at a typical flow rate of 10 sccm. A primary pump, which was connected to the chamber through an electronically controlled butterfly valve, was used to continuously remove the gas mixture from the chamber and maintain a constant low pressure of typically 0.12 mbar in the reactor. Under these conditions, the time required to fully remove residual nanoclusters from the sample region between the electrodes after a discharge pulse was estimated to be $\sim$1.5 s. This duration determined the typical time interval

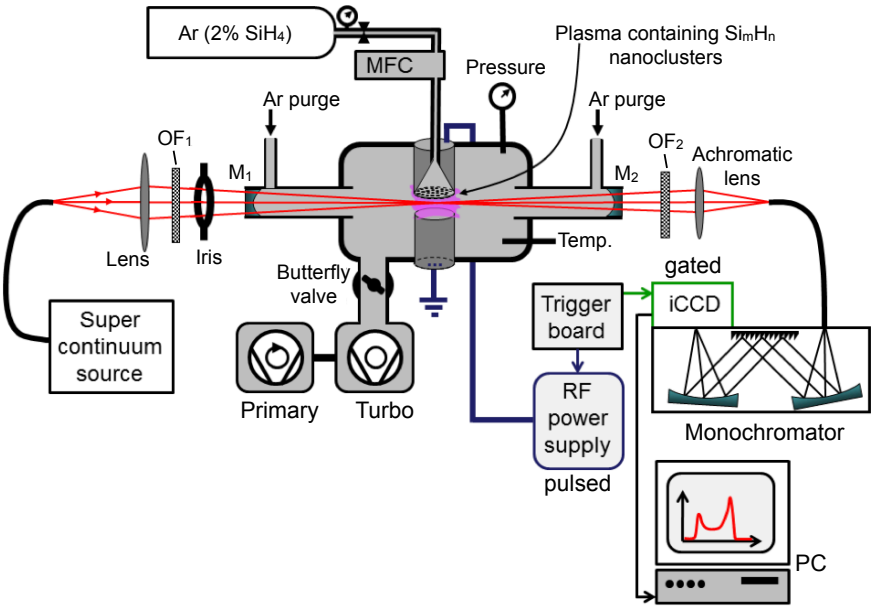

Figure 6.1: Schematics of the experimental setup. M_1, M_2: high reflectivity (HR) mirrors (R>0.9999). OF_1 and OF_2: combination of optical bandwidth and cut-off/on filters. The HR mirrors were purged with high-grade argon (99.999%).

of 6 seconds between plasma discharge trigger pulses, which were generated by a specifically designed trigger board. A more detailed description of the trigger system is given below (also cf. Figure 6.2).

We heated the gas to typically 150°C. At such a gas temperature, we ensure that the formation and accumulation of "first-generation" nanoparticles takes about 6 seconds before they start agglomerating. The discharge on-time was generally set to 2 s[1]. Before experiments were performed, the chamber was fully pumped by a turbo pump overnight to a base pressure of $\sim 10^{-6}$ mbar while maintaining the chamber at 150°C. The secondary pumping was done to clean the chamber and remove potential impurities.

6.1.2 Cavity-enhanced absorption setup

The light source used in the absorption measurements was a spatially coherent supercontinuum light (Fianium SC450) with a total output power of 5 W. It delivered pulses with a duration of ~5 ps and was operated at a repetition rate of 50 MHz. Its emission covered a broad spectral range from ~450 to 1800 nm; therefore appropriate combinations of long- and short-pass filters and/or bandpass filters were used to select an appropriate spectral region where the cavity mirrors are highly reflecting ($\Delta\lambda \approx \pm 30$ nm around the central wavelength). The light was coupled on-axis into the optical cavity for which the mirrors were connected to the reactor by vacuum flanges

[1]The discharge on-time was also varied between lower and higher values in a number of experiments to measure the absorption of nanoclusters during their growth. Those experiments are not presented in this thesis, but will be the focus of future studies.

(see Figure 6.1). The cavity was formed by two plano-concave high-reflectivity (HR) mirrors (diameter 25 mm, radius of curvature -2 m) with a manufacturer-specified reflectivity of R > 0.9999. The separation of the cavity mirrors was 152 cm. This cavity length was chosen to maximize the distance between the discharge region and the mirrors in order to protect the mirrors from degradation due to interaction with highly reactive species formed in the plasma. Additionally, the mirrors were purged with a small argon flow at a rate of typically 10 sccm. Whenever the mirrors were not in use, they were isolated from the plasma reactor through large diameter gate valves.

Two different sets of mirrors were used, with HR regions centred at 610 and 700 nm, respectively. The light transmitted through the cavity was focused with an achromatic lens (f = 3 cm) onto the 1 mm entrance aperture of a circular-to-rectangular multi-core fiber bundle. The fiber bundle was connected to the entrance slit of a monochromator (Shamrock 303i), which was used to disperse the light with a blazed diffraction grating of 600 lines/mm (corresponding to a spectral resolution of 0.65 nm). The light exiting the monochromator was detected with a gated iCCD (Andor iStar, DH740-18 mm). An optical filter after the cavity was used to protect the iCCD from exposure to excessive near infrared radiation.

6.1.3 Mirror reflectivity calibration

The wavelength-dependence of the reflectivity of the mirrors, R(λ) in Eq. (5.8), was established *independently* in the University College Cork laboratory using the method described in Ref [71]. R(λ) was determined based on the Rayleigh scattering cross-sections, α_{Ray}, of helium and carbon dioxide gases as described in Eq. (6.1):

$$\frac{1-R(\lambda)}{d} = \frac{(\frac{I_{CO_2}}{I_{He}})\alpha_{Ray}^{CO_2}(\lambda) - \alpha_{Ray}^{He}(\lambda)}{1-\frac{I_{CO_2}}{I_{He}}} \tag{6.1}$$

I_{CO_2} and I_{He} represent the light intensities through a cavity filled to 1 atmosphere with CO_2 and filled to the same pressure with helium gas, respectively. The main issue with the reflectivity measurements is that they are alignment-sensitive. It was very challenging to replicate the exact alignment used during the experiments of the extinction measurements carried out in the LPICM.

6.1.4 Experiment synchronization

A trigger board synchronized the plasma discharge with the gated detector. As shown schematically in Figure 6.2, the trigger board generated three trigger pulses. The *initial* trigger pulse determined the start and the duration of the plasma discharge (indicated by blue arrows in Figure 6.2). The falling edge of the initial pulse triggered two subsequent trigger pulses for the iCCD (indicated by green arrows in Figure 6.2). The *first* of these two pulses is generated immediately on the falling edge of the "plasma pulse" and was used to record the cavity transmission with the sample ($I(\lambda)$ in Eq. (5.8)) shortly after the end of the discharge plasma, the *second* one was always generated 3.5 s later and triggered the measurement of the cavity transmission without the sample ($I_0(\lambda)$ in Eq. (5.8)), *i.e.* without silicon nanoclusters. The two pulses for

the detector triggered a digital delay and a gate generator of the iCCD. The delay time and gate width (=integration time) could be freely chosen (vertical dashed lines in Figure 6.2), but are the same for the measurements of I and I_0. The gate width was 10 ms in all cases. The gate delay, however, was varied for different experiments between ~ 1 and ~ 200 ms. The time difference of 3.5 s between the two pulses for the iCCD (green pulses) was sufficiently long to ensure that any residual nanoclusters were pumped out of the reactor between recording the sample (I) and the background (I_0) transmission. Typical spectra were averaged over 100 to 1000 plasma pulses.

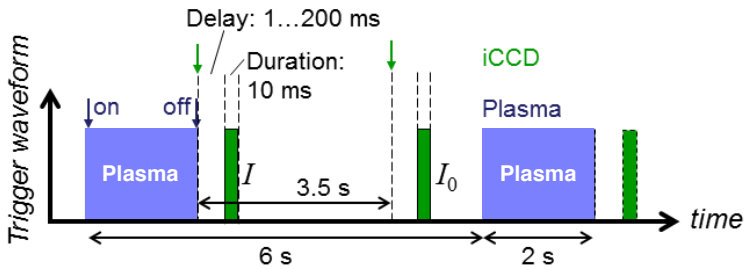

Figure 6.2: Typical trigger sequence to synchronize the iCCD with the RF power supply. Blue: plasma triggers, green: iCCD triggers.

We stress here that our technique in measuring I and I_0 alternatingly between plasma pulses, rather than subsequently at the end of the total number of pulses, has the advantage that systematic errors, such as light source fluctuations, variations in residual optical losses due to scattering, very gradual misalignment effects or mirror drifts, and slow and small pressure variations, are effectively reduced due to the short time separation between the respective measurements of I and I_0.

Chapter 7

Experimental Results and Discussions

This chapter covers our experimental results concerning the aromatic silicon nanoclusters. In the first place, we present the extinction or absorption spectra of plasma-born aromatic silicon nanoclusters in the visible region using the experimental setup and synchronization presented in Chapter 6. Second, we exploit the absorption measurements performed in conjunction with an applied DC electric field (to be described in details hereafter) and provide a proof that those nanoclusters possess a permanent dipole moment. An estimation of the dipole moment is made using the absorption measurements combined with a theoretical study. Finally, we present a structural characterization of deposited aromatic silicon nanoclusters based on high-resolution transmission electron microscopy measurements.

7.1 Extinction measurements

7.1.1 Investigation of the spectral range 575-665 nm

The following measurements were carried out using a set of mirrors centered at 610 nm covering a spectral range of 575 - 665 nm. In Figure 7.1, we show the measured extinction (units of cm^{-1}), according to Eq. (5.8). The light intensities transmitted through the cavity with and without plasma were measured for a gas pressure of 0.115 mbar and a temperature of 150°C. The plasma on-time was 2 s and the gate delay time (the time between the end of the RF pulse and the beginning of the acquisition measurement) was 100 ms. The spectrum was averaged over long times (1000 acquisitions). As can be seen from Figure 7.1, the spectrum shows an extinction peak in the visible around 645 nm and then, the signal decreases until around 670 nm.

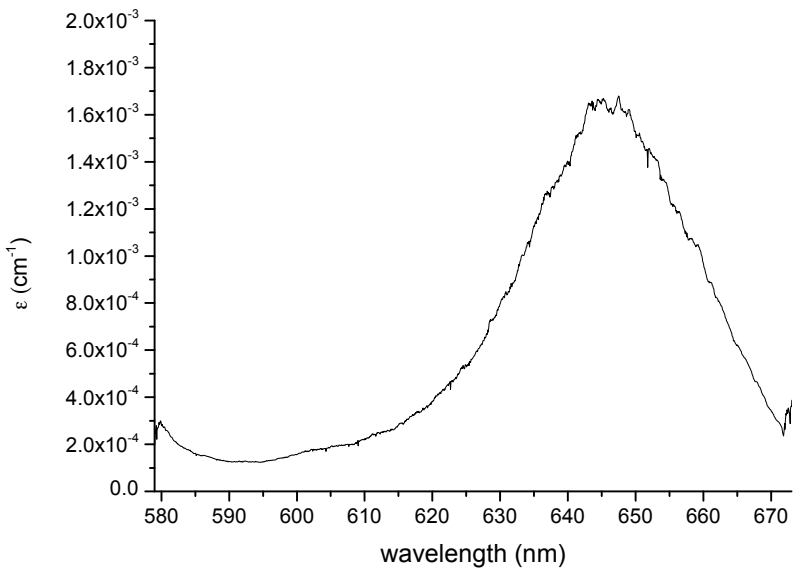

Figure 7.1: Extinction measured using the 610 nm mirrors. Plasma on-time is 2 s, gas mixture flow is 10 sccm, gate width and delay are 10 ms and 100 ms, respectively. Gas pressure and temperature are 0.115 mbar and 150°C, respectively.

7.1.2 Investigation of the spectral range 655-745 nm

In Figure 7.2, we show the measured extinction using the set of mirrors centered at 700 nm covering a spectral range of 655-745 nm. The measuring conditions were similar to the measurements done for the previous spectral range. Although the measured extinction is essentially flat in the high reflectivity range of the mirrors, the spectrum in Figure 7.2 looks coherent with respect to Figure 7.1, that is, the signal in the latter has a maximum around 645 nm and then decreases until 670 nm, while the signal in the former spectrum decreases from its beginning at about 655 nm until 700 nm and then increases again.

Taking a closer look at the calculated absorption spectra of $Si_{19}H_{12}$ nanoclusters at 0K, Figure 4.8, we notice a non-zero oscillator strength at about 650 nm, which is very close to the measured absorption peak at about 645 nm (Figure 7.1). Moreover, we find non-zero oscillator strengths at about 674 nm and 722 nm (see Figure 4.8-b). At these wavelengths, the measured spectrum using the 700 nm mirrors (Figure 7.2) shows some absorption features.
We would like to note that unlike the absorption measurements of single molecules where the absorption peaks always look sharp and well-defined, we do expect that the absorption peak of a single of nanocluster formed in a plasma reactor to be broad due to the thermal movement of the cluster atoms under the experimental conditions. In addition, considering that our plasma conditions will not lead to the creation of one single isomer of $Si_{19}H_{12}$, but rather to a wide

variety of similar silicon nanoclusters, the effective absorption over a relatively broad spectral region can readily be understood.

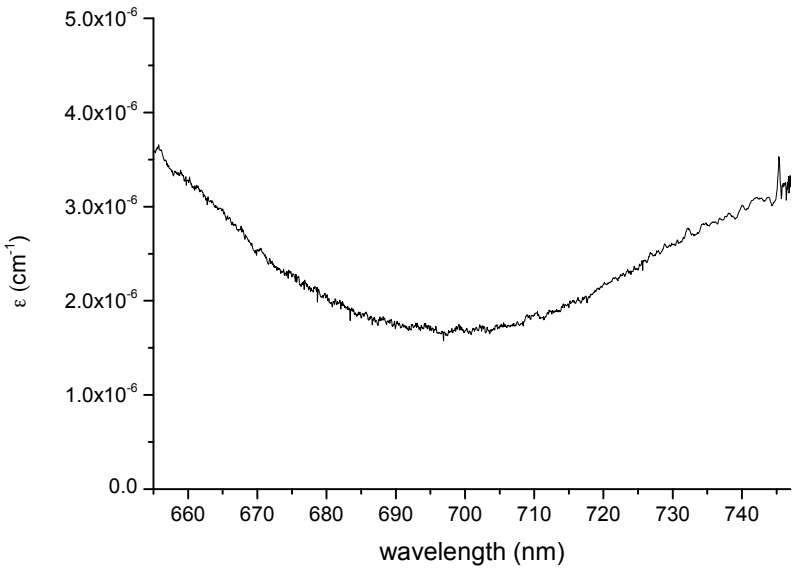

Figure 7.2: Extinction spectrum measured using the 700 nm mirrors. Plasma on-time is 2 s, gas mixture flow is 10 sccm, gate width and delay are 10 ms and 100 ms, respectively. Gas pressure and temperature are 0.115 mbar and 150°C, respectively.

7.1.3 Effect of the gate delay time

In Figure 7.3, we show a set of extinction measurements done with a range of gate delay times, between 1 ms and 250 ms, using the 610 nm mirrors. The measurements were performed with a plasma on-time of 2 s, gas pressure and temperature of 0.165 mbar and 150°C, respectively, a gate width of 10 ms, and a gas mixture flow of 10 sccm. We notice from Figure 7.3 that the intensity of the measured extinction varies with the delay time. The extinction increases with the increase in delay time until 150 ms and then rapidly decreases. This can be explained as follows: when we turn off the plasma, the absorbing nanoclusters, mainly located above the detection beam with the highest density near the shower head, move down swept by the gas flow. They cross the detection beam after a few milliseconds, with a maximum density of nanoclusters reaching the light beam at 150 ms. Waiting for a longer time (200 ms), we find a drop in the extinction indicating that most of the absorbing nanoclusters had already crossed.

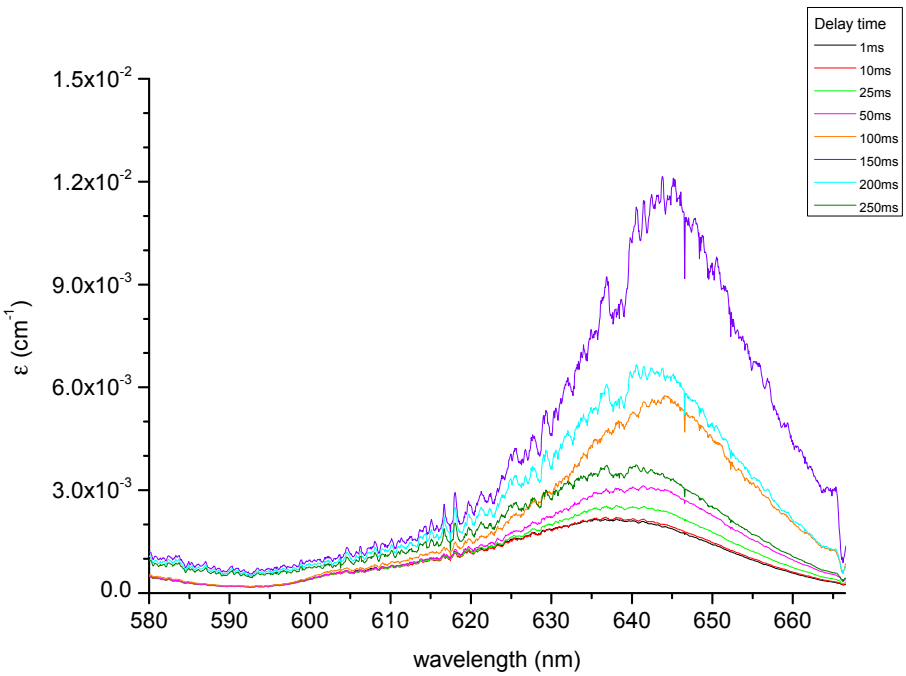

Figure 7.3: Extinction measured using the 610 nm mirrors for a range of gate delay times. Plasma on-time is 2 s, gas mixture flow is 10 sccm, and gate width is 10 ms. Gas pressure and temperature are 0.165 mbar and 150°C, respectively.

7.2 Effect of an applied DC electric field

Previous theoretical studies have shown that aromatic silicon nanoclusters possess a strong permanent dipole moment (see Section 2.1). In order to confirm and to explore such a characteristic quantitatively, we will examine the effect of an applied DC electric field on the measured absorption spectra. But first, what role does an electric field play on polar molecules? The next two subsections will clarify it.

7.2.1 Permanent dipole moment

In general, molecules are electrically neutral, but they can have an asymmetric charge distribution, as for example the water molecule. In other words, the centers of positive charge density and negative charge density do not coincide.[72] This charge separation leads to an electrical dipole moment and the molecule, then, is called a polar molecule. Classically, the dipole of a molecule can be viewed as one point charge $+q$ and one negative point charge $-q$ separated by a distance r (see Figure 7.4). The electric dipole moment, $\vec{p}$, defined as

$$\vec{p} = q\vec{r} \tag{7.1}$$

has a magnitude of $q|\ \vec{r}\ |$ (C·m in SI units)[1] and points from the negative to the positively charged region.

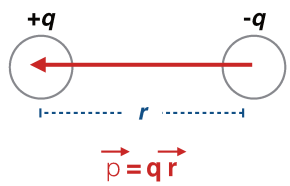

Figure 7.4: Electric dipole moment. p is equal to the magnitude of the charge multiplied by the distance between them with the direction being toward the positive charge.

7.2.1.1 Polar molecules in a DC electric field

What happens when a polar molecule is placed in a DC electric field? If the DC electric field is homogeneous, Figure 7.5-a, it will only provide a torque, $\vec{\tau}$, that orients the molecular dipole moment, $\vec{p}$, along the electric field lines. On the other hand, if the DC electric field is inhomogeneous, Figure 7.5-b, it will not only orient, but also exert a force on the polar molecule to displace it since the forces on the positive and negative charges of the dipole do not cancel each other exactly. Hence, the field provides an overall **translational force** on the molecule. The resultant force is defines as:

$$\vec{F} = p\nabla\vec{E} \tag{7.2}$$

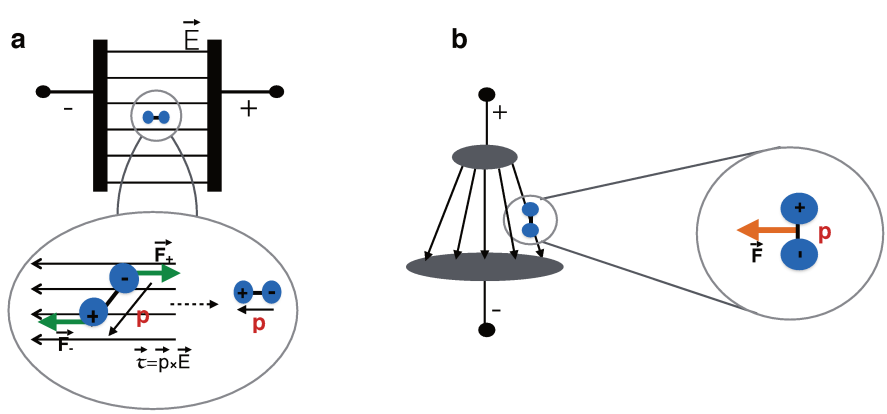

Figure 7.5: Polar molecule in an electric field (a) homogeneous and (b) inhomogeneous electric field.

[1]The SI unit for electric dipole moment is Coulomb-meter. Since, this is too large to be practical on the molecular scale, the dipole moments are commonly measured in Debye (1 Debye= 3.33564× 10^{-30} $C{\cdot}m$).

7.2.2 Experiment synchronization

In the following experiments, a DC bias was applied between the top and bottom electrodes when the plasma was turned off. To this end, one more trigger pulse was added to the trigger board to determine the start and stop of the applied DC bias. In order to eliminate any issues from drifting cavity alignment, these two measurements were carried out concurrently, *i.e.* the measurements alternated, shot-by-shot, between measuring the extinction with an applied bias, and measuring it without a bias (see Figure 7.6).

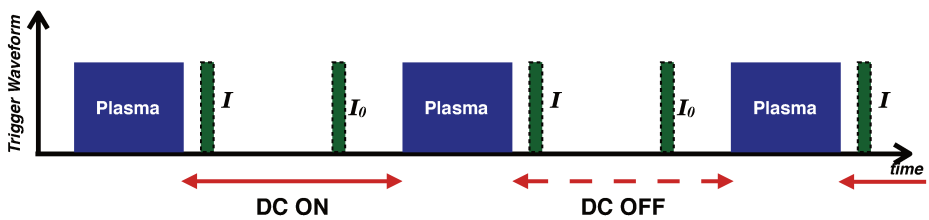

Figure 7.6: Trigger sequence with an applied DC bias.

7.2.3 Extinction measurements with a 120V DC bias

Figure (7.7) shows the extinction measured with an applied DC bias of 120V compared to the extinction measured without any bias, carried out using the 610 nm mirrors. The plasma duration was 2 s. The measurements were taken with a 10 ms gate after a 100 ms delay. The gas pressure and temperature were 0.115 mbar and 150°C, respectively, with a gas mixture (SiH_4/Ar) flow of 10 sccm. It is clear from Figure 7.7 that the absorption decreases in the presence of a DC bias (red curve). This is the first indication that the nanoclusters possess a permanent dipole moment. Since the electric field is inhomogeneous in the reactor chamber, the dipole forces acting on the nanoclusters affected their translation during their drift due to the gas flow, resulting in a change in the absorption signal.

The fractional difference between the two measurements, $\frac{\epsilon_{(0V)}}{\epsilon_{(120V)}}$, in Figure 7.8, shows how the change in extinction due to the applied bias is not uniform across the entire spectral measurement range. This finding supports our claim that the extinction peak centered at about 645 nm (see Figure 7.1) represents a true absorption peak.

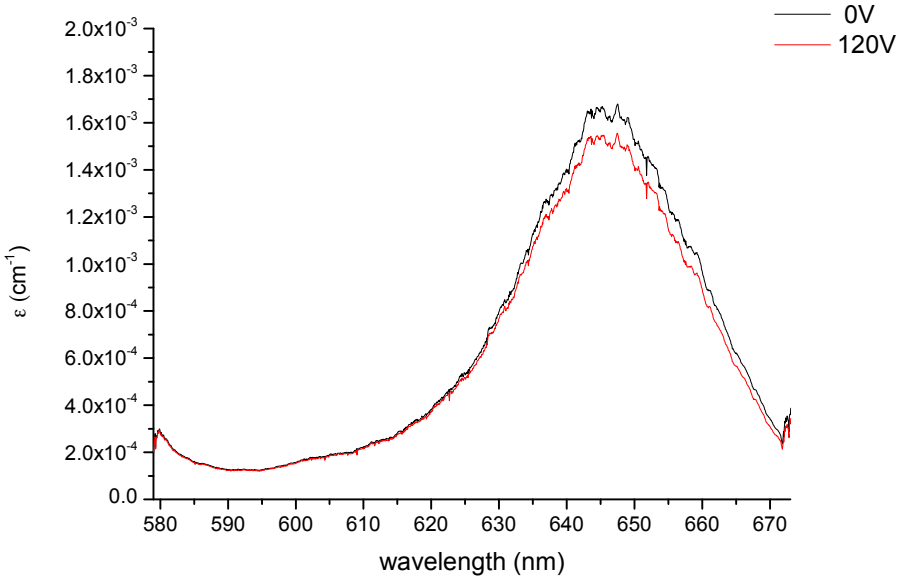

Figure 7.7: Extinction measurements with and without an applied bias of 120V. The extinction is measured using the 610 nm mirrors and an applied DC bias of 120V. The plasma duration is 2 s and the gate width and delay are 10 ms and 100 ms, respectively. The gas mixture flow is 10 sccm and the pressure and temperature of the gas are 0.115 mbar and 150°C, respectively.

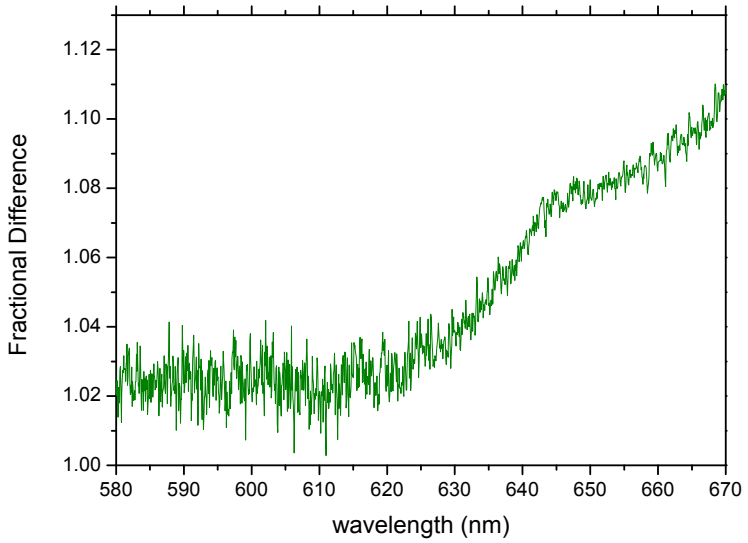

Figure 7.8: Fractional difference between the measured extinction with and without an applied DC bias of 120V.

7.2.4 How does the extinction change as a function of the applied DC bias?

We have performed a set of extinction measurements with and without an applied electric field for a range of DC biases (25V, 100V, 160V, and 240V) under the same experimental conditions indicated above. Figure 7.9 shows the extinctions measured with an applied bias compared to that without any bias for each experiment. In all our measurements, we find a decrease in the absorption signal in the presence of an applied electric field. However, the decrease of the absorption depends on the strength of the applied field and follows a certain trend. In order to clarify this dependence, we plot in Figure 7.10 the percentage of the *reduction* in the absorption ($\frac{\epsilon_{0V}-\epsilon_{DC}}{\epsilon_{0V}}\times 100$) as a function of the DC bias. Here, we notice that at 25V and 100V, there is only a slight decrease in the absorption. However, we find that the amount of reduction starts to increase linearly with higher DC bias to become about 10.7% and 19% at 160V and 240V, respectively.

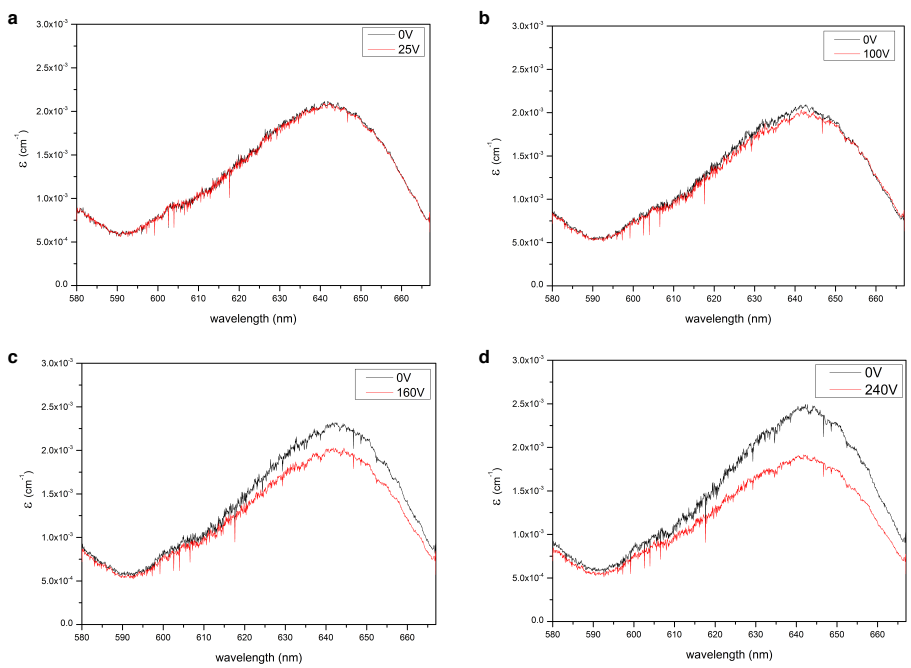

Figure 7.9: A set of extinction measurements with and without applied DC bias. Applied bias of : (a) 25V, (b) 100V, (c) 160V, and (d) 240V. The extinction is measured using the 610 nm mirrors. The plasma duration is 2 s and the gate width and delay are 10 ms and 100 ms, respectively. The gas mixture flow is 10 sccm and the pressure and temperature of the gas are 0.115 mbar and 15o°C, respectively.

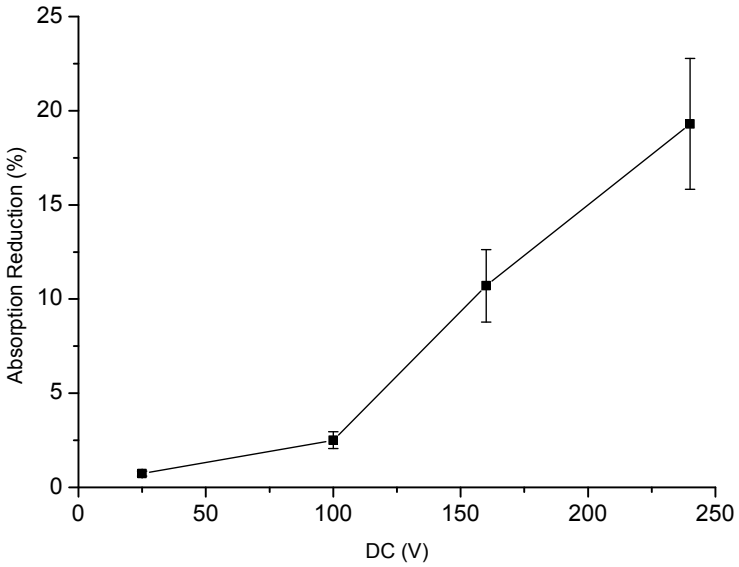

Figure 7.10: Reduction in the measured absorption as function of the applied DC bias. The error in the measured extinctions is due to systematic errors and noise.

How can we explain such a behavior? Can it be helpful in providing a quantitative estimation of the permanent dipole moment of aromatic silicon nanoclusters?

7.3 DC electric field simulations

In order to better understand the inhomogeneity of the electric field in the reactor chamber, simulations were the best way to give us a full demonstration. The simulations were done, thanks to François Silva, using the finite element methods with a 3D electrostatic solver. First, we designed our reactor chamber (see Figure 7.11 for a cross-sectional view) taking into account its exact configuration and dimensions. Thick blue lines marked in Figure 7.11 indicate the lines along which we calculate the different components of the electric field; L is a horizontal axis that, to a good approximation, represents the axis of the light beam, L_1 to L_{12} are several vertical axes taken from the top to the bottom electrode with lengths of 40 mm. The dipole forces are then calculated from the gradients of the electric fields.

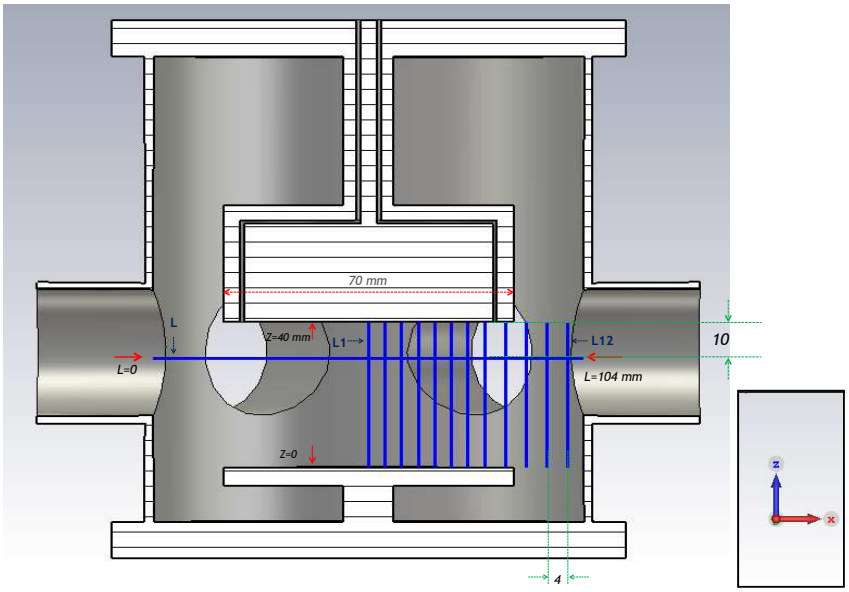

Figure 7.11: A schematic representation of the reactor chamber. L and L_n indicate the lines along which the simulations of the electric field were taken into consideration in our analysis: x-component of the electric field through the light beam along L, z-component of the electric field from the top to the bottom electrode along L_1 until L_{12}.

Figure 7.12 shows the potential and the electric field vector map after applying a 240V bias. It is clear from Figure 7.12-b that the the electric field is symmetric in the reactor, it is mostly homogeneous in the center (vertical arrows), and strongly inhomogeneous near the edges of the top electrode.

In the following, we track the behavior of the nanoclusters, under the influence of the dipole forces after we switch-off the plasma. In order to simplify our analysis, we separate between the dipole forces acting on the nanoclusters in the z-direction and those in the plane of the light beam. Since the reactor chamber has a perfect cylindrical configuration, we perform our analysis using cylindrical coordinates (r, θ, z). To this end, we calculate the non-zero components of the electric field ((E_r) and (E_z)) from which we find the gradients and the corresponding dipole forces.

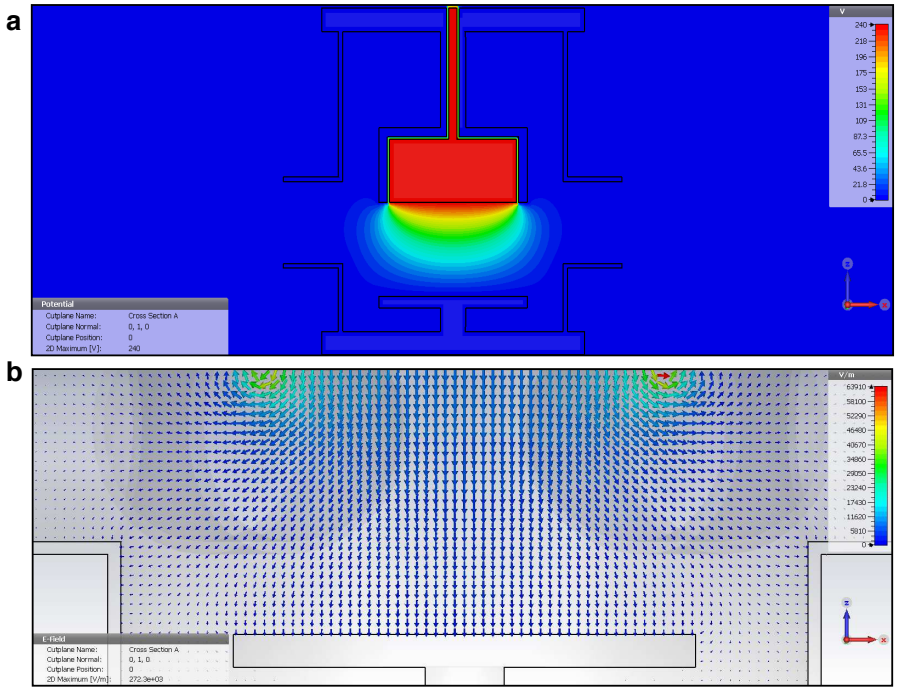

Figure 7.12: Cross-sectional view of the electric field simulations. Electric potential between the two electrodes (a) and electric field vector map (b) after applying a 240V bias.

7.3.1 Dipole forces acting on the nanoclusters

Along the z-axes:

The gradient of the z-component of the electric field (E_z), along say L_1 in Figure (7.11), gives the dipole force acting on the nanocluster in the z-direction. Figure 7.13 shows the dipole forces calculated along the different lines L_2 to L_{12} (see Figure 7.11), with an applied bias of **240 V**, and assuming that the nanoclusters possess a dipole moment of 2 Debye. We notice from Figure 7.13-a that the dipole forces in the region of interest (between the top electrode and the light beam, *i.e.* between 30 and 40 mm) are negative for lines L_1 to L_8, *i.e.* the forces are directed downwards towards the light beam. While Figures 7.13-b,c show that the dipole forces become mainly positive in this region for lines L_9 to L_{12}. Nevertheless, comparing the strength of the dipole forces with the *neutral drag force* acting on ∼1nm nanoclusters in the z-direction (see Figure 7.14),[73] we find that the calculated dipole forces are about four orders of magnitude weaker. All other forces acting on the nanoclusters (see Section 5.1.4), such as the gravitational force and the thermophoretic force, can be neglected in our case due to the very small size of the silicon nanoclusters and the absence of a significant temperature gradient in our reactor, respectively. Therefore, we conclude that the movement of the nanoclusters in the z-direction is mostly determined by the neutral drag force. Consequently, nanoclusters, initially located in the same horizontal plane, will reach the light beam at the same time.

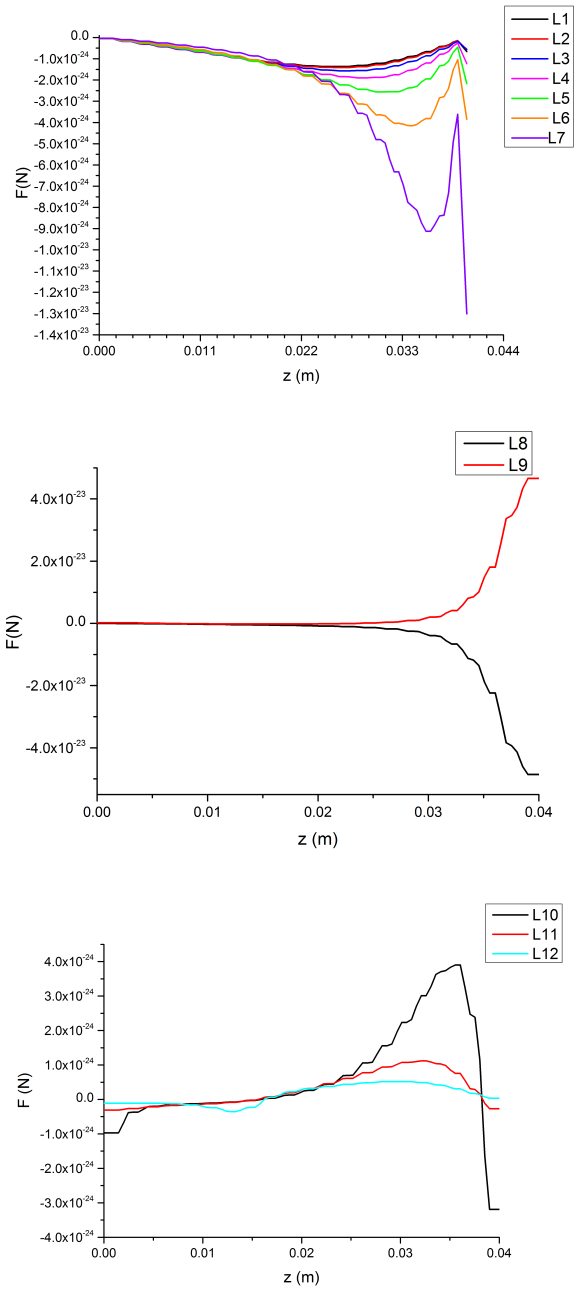

Figure 7.13: Dipole forces acting on the nanoclusters in the z-direction. The dipole forces are calculated assuming that the nanoclusters possess a permanent dipole moment of 2 Debye and for an applied DC bias of 240 V.

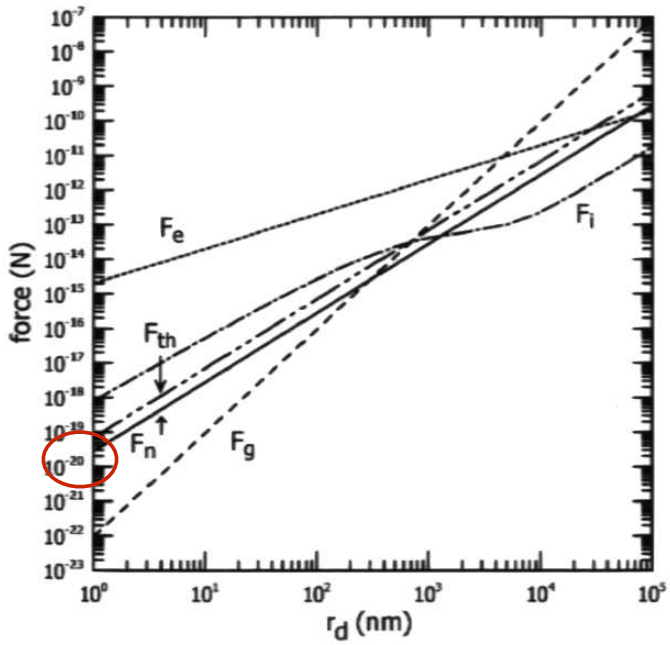

Figure 7.14: A comparison of the different forces acting on a spherical nanoparticle as a function of its diameter.[73] F_e is the electrostatic force exerted by the electric field on the particle in the discharge, F_i is the ion drag force, F_{th} is the thermophoretic force, F_n is the neutral drag force, and F_g is the gravitational force.

Along the polar axes:

At this point, we would like to demonstrate how the inhomogeneity of the electric field influences the movement of the nanoclusters and, hence, their distribution in the plane of the light beam. In Figure 7.15, we plot the gradient of E_r along the polar axis with θ=0 for a range of potentials (25V, 100V, 160V and 240V), which is similar to all rays with any theta in the polar system due to cylindrical symmetry (see Figure 7.16 for a 3D representation). One can notice from Figure 7.15 that the gradients of E_r, that correspond to the dipole forces, are positive in the center of the reactor and progressively increase until about 24 mm from the center. After that, the forces show a sudden drop and become negative around 30 mm. Then, they start to increase (with a negative sign) until around 36 mm (*i.e.* parallel to the edge of the electrode). Finally, the forces decrease again, keeping their negative sign, reaching the walls of the reactor. This means that the dipole forces act on the nanoclusters in such a way that, at some instants, they push them toward the rector walls (positive forces) and, at other instants, toward the center of the reactor (negative forces). Generally speaking, while the nanoclusters are being drifted from the top electrode toward the detection beam by the neutral drag force, they also spread out under the influence of those dipole forces. Consequently, the nanoclusters will change their planar distribution with respect to their initial distribution depending on the applied bias.

Does any change in the in-plane distribution of the nanoclusters affect the absorption measurements? Can we track the change in the distribution while the nanoclusters move from a region near the top electrode toward the detection beam?

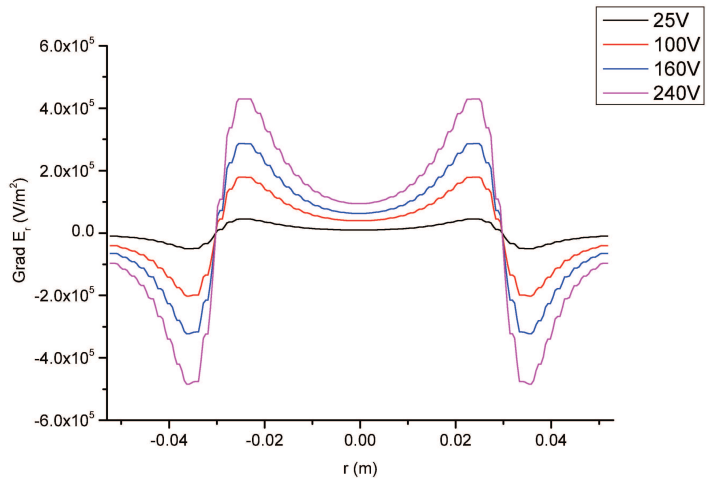

Figure 7.15: The gradient of E_r along the polar axis with θ=0 for the different applied biases. For clarity, we show the gradient of E_r from the left side to the right side of the reactor.

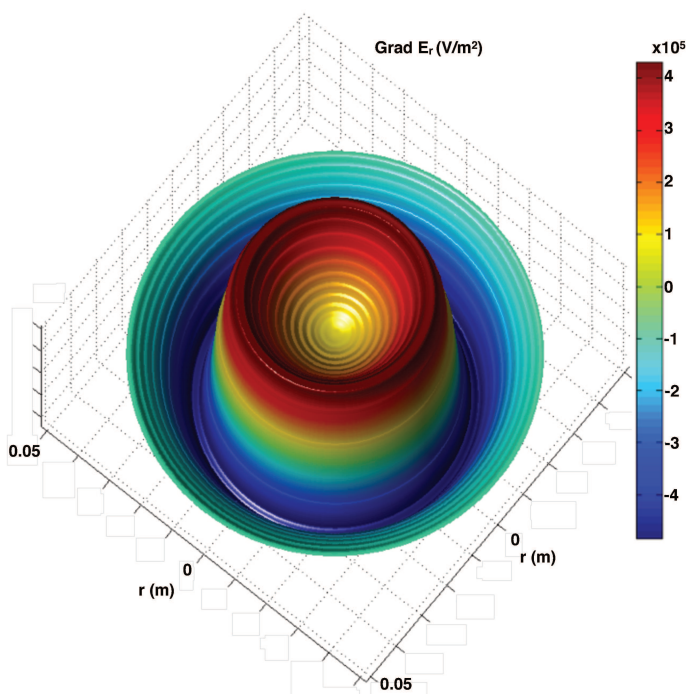

Figure 7.16: Three-dimensional representation of the gradient of E_r calculated for 240V bias.

In our experiments, we have measured the extinction (or the absorption), as follows:

$$\epsilon(\lambda) = \sum_i \sigma_i \int_0^d n_i(x)dx = \frac{1-R}{d}\left(\frac{I_0}{I} - 1\right) \tag{7.3}$$

where the sum i is over all relevant species, σ (cm^2 particles^{-1}) is the cross-section, and n is the number density (particles cm^{-3}). Therefore, equation 7.3 indicates that the measured absorption is proportional to the density of the nanoclusters in the volume of the light beam.

7.4 Distribution of the nanoclusters from trajectory simulations

While the nanoclusters are moving toward the detection beam in the presence of the applied inhomogeneous electric field, two phenomena are happening at the same time:

- The nanoclusters spread out under the influence of the dipole forces establishing a new distribution in the plane.
- This plane is shifted down to the plane of the detection beam.

In order to gain a deeper insight into the densities of the nanoclusters in the plane of the detection beam, we follow their trajectories from their initial positions in a region below the top electrode until they reach the light beam, where we obtain their new distribution.

Trajectories simulations

The simulations of the nanocluster trajectories were performed as follows:

- We start with an equal distribution (or density) of particles in each 1 mm ring section in a plane that is 5 mm below the top electrode (see Figure 7.17 for an illustration). The mass of the particle corresponds to the mass of a $Si_{19}H_{12}$ nanocluster (546 amu).
- Using Newton's equations of motion, we follow the trajectory of the particles under the influence of the dipole forces (calculated from the gradient of E_r) with a time step of 1 ms until they reach the plane of the detection beam. Thus, we obtain the final position of each particle on that plane.
- From the number of particles in each ring section, we find the new densities and, hence, the new distribution of particles.

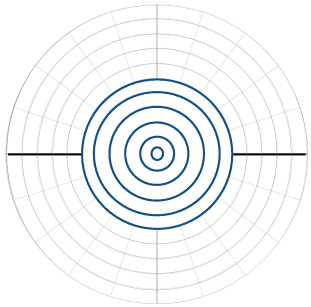

Figure 7.17: Schematic illustration of the distribution of particles on a plane. We start with an equal density of particles in each ring section.

7.5 Estimation of the permanent dipole moment

Following the same procedure applied for the absorption measurements (see Figure 7.10), we determine the percentage in the change in the average density of the nanoclusters, calculated in the plane of the detection beam, in the presence and absence of a DC bias.

At the instant we switch off the plasma, the nanoclusters are mainly equally distributed in a region under the powered electrode, so in the absence of any applied DC bias, the nanoclusters reach the detection beam plane, to a good approximation, keeping their initial distribution.[65] However, in the presence of a DC bias, they attain a new distribution which is obtained from our trajectory simulations. A comparison between those two situations have mainly shown a reduction in the average density of the nanoclusters in the presence of a DC bias which also depends on the DC field applied. We have performed the above analysis for three different cases: particles possessing a dipole moment of 1.5, 2.0, and 2.5 Debye, respectively.

Figure 7.18 shows the percentage in the reduction of the average density of particles as a function of the applied bias, for the different dipole moments, compared to the reduction in the absorption obtained from our experiments (values plotted in Figure 7.10). First, we notice that only for 25V, we obtain from our simulations a slight increase in the density of particles (∼2%) in the presence of applied bias (instead of a slight decrease) for the three dipole moment cases. This is due to the confinement of some particles in a certain region that is parallel to the edge of the top electrode. However, for all other DC biases, we find a reduction in the calculated density that depends on the applied bias, *i.e.* on the strength of the dipole forces acting on the particles, and thus on the way and the number of particles that participate in the redistribution in the different rings on the plane of the detection beam. Interestingly, we find that the reduction in the density of particles possessing a dipole moment of 2.0 Debye and 2.5 Debye, well matches the reduction in the measured absorption and follows the same trend. For instance, we obtain a density reduction of 2.3%, 9.2%, and 15.9% in the 2.0 Debye case and 5.3%, 10.8%, and 17.6% in the 2.5 Debye case, while the measured absorption reduction is 2.5%, 10.7%, and 19%, for the 100V, 160V, and 240V, respectively. On the other hand, the values corresponding to the 1.5 Debye case are relatively far from the experimental values.

Therefore, based on this combined theoretical and experimental analysis, we now have a direct

proof that aromatic silicon nanoclusters with a size of ∼1nm possess a permanent dipole moment between 2.0 and 2.5 Debye. This result is in perfect agreement with previous estimations of the dipole moment of the $Si_{19}H_{12}$ isomers, based on *ab initio* calculations.[47]

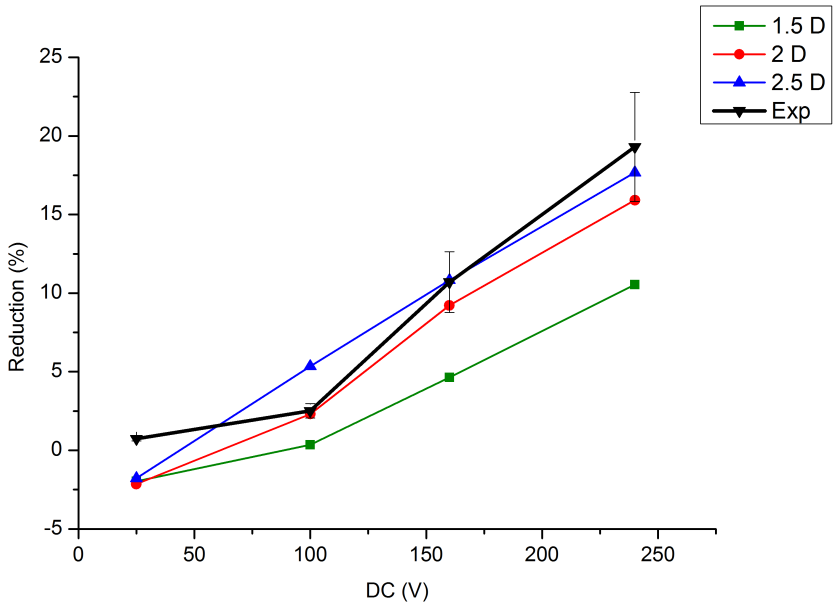

Figure 7.18: Reduction in the measured absorption and calculated particle density as a function of the applied DC bias.

7.6 Characterization of deposited silicon nanoparticles

7.6.1 Structure of deposited silicon nanoparticles

We performed further experiments in order to analyze the structure of deposited silicon nanoclusters using a high-resolution transmission electron microscope (HRTEM). In this study, three samples were prepared with similar plasma conditions, but with a different deposition time; 2 min, 5 min and 20 min. The plasma was pulsed with a frequency of 1 Hz and a duty cycle of 10%. The RF power was 10 W and the gas temperature and pressure were 160°C and 0.11 mbar, respectively. A TEM grid with a hole membrane covered by a 15 nm carbon layer, to avoid particle charging during electron beam irradiation, was placed on the bottom electrode to collect the deposited nanoparticles. The HRTEM analysis was performed *ex situ* using the NanoMAX microscope of LPICM which has a resolution of about 1Å.

Figure (7.19) shows TEM images for the three samples. After 20 min deposition, we obtained agglomerates with the smallest between 15 and 30 nm (see Figure 7.19-a). When we decreased the deposition time to 5 min, we obtained smaller agglomerates, with sizes ranging between 10

and 15 nm (Figure 7.19-b). Then, we decreased the deposition time to 2 minutes. The smallest agglomerates of silicon nanoclusters were found to have sizes ranging between 2 and 10 nm (Figure 7.19-c). At first view, all agglomerates seem to have an amorphous structure.

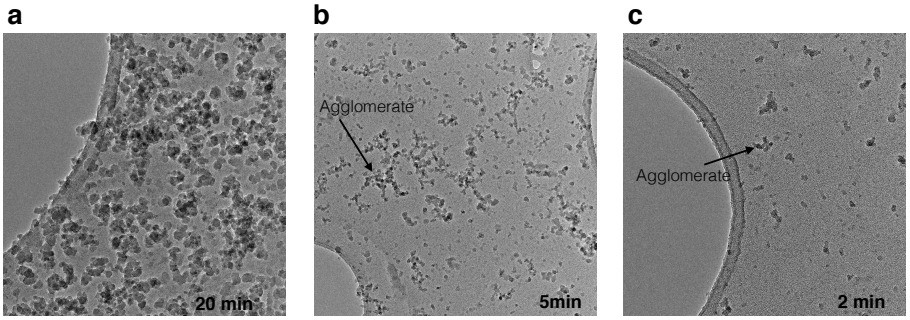

Figure 7.19: HRTEM images of silicon nanoparticles obtained after different deposition times. (a) 20 min (b) 5 min and (c) 2 min.

Then, we took a closer look and performed a careful analysis on the sample obtained after 2 min deposition. Here, the HRTEM images reveal the existence of nanoparticles with a well-defined crystalline structure different from the diamond structure of silicon. Figure (7.20) shows a HRTEM image of an area on the surface with crystalline nanoparticles. Their size ranges between 2.0 and 3.5 nm. A Fourier transform analysis indicated an interplanar spacing (d) of $\sim$ 2.1 Å for the three investigated nanoparticles. A similar interplanar distance in the (100) plane was found for the **primitive hexagonal** silicon structure (Space group P6/mmm), with lattice constants a= 2.463 Å and c=2.326 Å, which was obtained from the compression of silicon bulk at about 36 GPa.[6]

Interestingly, silicon nanoparticles ($<$ 5 nm) with ordered structures, formed in silane-based RF plasmas, having crystalline lattices other than the diamond-cubic are reported in the literature, as for instance the cubic (bcc and bc8) structures[74] or the hexagonal-close-packed structure.[75] Although those phases have mainly been reported as possible high-pressure phases of silicon, they have also shown to exist in nanostructured silicon obtained from a RF plasma. There can be several explanations for the formation of different phases, although it is not well understood yet: first, it is accepted that the diamond structure is not the most stable structure for small nanoparticles. Veprek *et al.*[76] reported on diamond-structured nanocrystals formed in different chemistries and claimed that 3 nm represents the lower limit size for their stability. Several factors related to the process of particle formation by RF plasma such as the process of temperature, pressure, and the inert gas dilution, may play an important role in the construction of the particle structure.[74] On the other hand, the formation of an uncommon phase of silicon can be attributed to the "chemistry with a hammer" mechanism. This phenomenon explains why reactions that are normally observed only at extremely high reactant pressures, can be carried out in low-pressure, ultra-high vacuum conditions where the collision energy of the incident particle on a surface is a key factor in determining the observed chemistry of unexpected reactions.[77] If a charged nanocluster escapes from our plasma bulk, it will collide with high impact energy on

the hard surface, such that extreme conditions of pressure and temperature are experienced by the atoms inside the cluster. At the same time, the atoms cannot easily "escape" since they are sterically confined by the surrounding cluster atoms. Consequently, unusual chemical reactions between the concerned atoms can take place that otherwise would only become possible at extremely high pressures and temperatures.[78, 79]

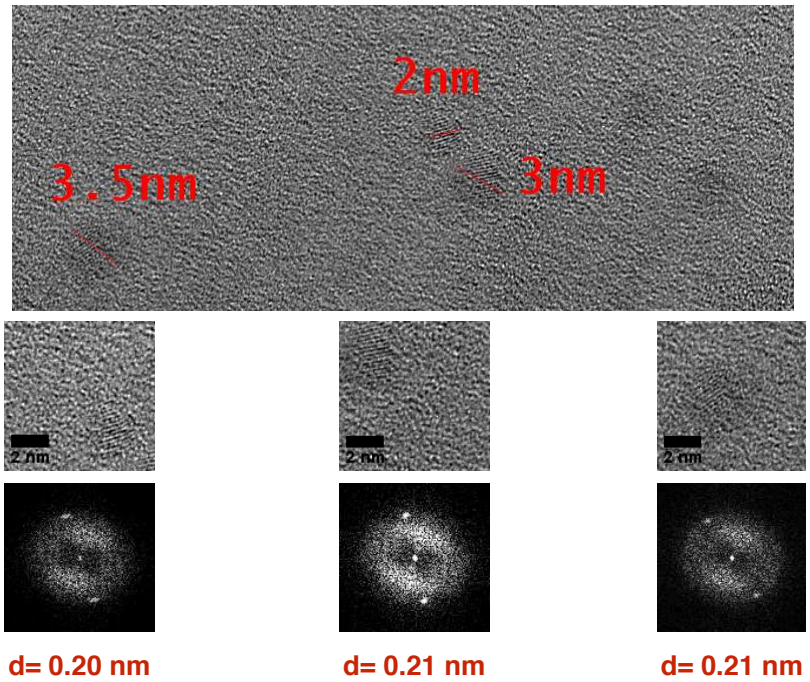

Figure 7.20: HRTEM images of crystalline silicon nanoparticles. Fourier transform analysis has been used for three different nanoparticles to explore their crystalline structure. "d" corresponds to the interplanar distance calculated from the different Fourier transforms of the HRTEM images.

7.7 Conclusion

An experiment was designed, built and performed to study the absorption of aromatic silicon nanoclusters in the visible region, *in situ*, in a plasma reactor using IBBCEAS. A plasma reactor for the generation of Si_mH_n nanoclusters was combined with a cavity enhanced absorption setup as a diagnostic tool. The plasma parameters were optimized such that only ∼1nm particles were formed. We synchronized the absorption measurements with the nanocluster production and we measured the transmitted light intensities, with and without the absorbing species, alternatingly between plasma pulses. Using a spatially coherent supercontinuum light source, several filters, and two sets of highly reflecting mirrors, covering two spectral ranges between 575-665 nm and between 655-745 nm, respectively, we found an extinction peak in the visible around 645 nm while standard tetrahedral silicon nanoclusters of this size can only absorb in the ultraviolet.

The experiments have also demonstrated that our aromatic silicon nanoclusters possess a permanent dipole moment. This property was deduced from the decrease in the measured extinction in the presence of an applied DC bias. The decrease in the absorption was a consequence of the inhomogeneity of the electric field in the reactor chamber, so that the dipole forces influenced the movement of nanoclusters. Moreover, measurements have shown that the change in the absorption signal has a unique dependence on the strength of the applied electric field. Simulations of the electric field helped us to understand the behavior of the nanoclusters under the influence of the dipole forces. We obtained a coherence between the simulations of the density of nanoclusters in the plane of the detection beam and the measured extinction for different applied bias voltages. Now, we have a compelling evidence that aromatic silicon nanoclusters possess a permanent dipole moment between 2.0 and 2.5 Debye!

We were eager to perform additional studies on the nanoclusters but, after their deposition. To this end, we performed HRTEM measurements on samples with different deposition times, but with similar optimized plasma conditions. Our HRTEM analysis on selected areas have shown the presence of some crystalline nanopartcles along with amorphous ones. We found that some of the 2.0 to 3.5 nm crystalline nanoparticles attain a primitive hexagonal structure. This indicates that exotic forms of silicon can be produced by a RF plasma and not only under extreme conditions.

Part II

Two-Dimensional Materials

Chapter 8

Introduction

In 1959, Richard P. Feynman gave a lecture titled "There's plenty of room at the bottom. *An invitation to enter a new field of physics*," at the American Physical Society meeting in Caltech.[80] There, Feynman raised several questions, such as *What could we do with layered structures with just the right layers? What would the properties of materials be if we could really arrange the atoms the way we want them?* His inspiring talk motivated generations of scientists to discover new low-dimensional materials. In 1966, Frindt isolated a single crystal of MoS_2, only several molecular layers thick, by using the scotch tape method.[81] Materials science had a major scientific breakthrough in 2004 when Konstantin Novoselov, Andre Geim, and their colleagues isolated a single layer of carbon, graphene, again through the scotch tape exfoliation of graphite and measured its electronic transport properties.[82] The importance of this achievement was sealed in 2010, when the Nobel prize was awarded to both researchers. The freestanding 2D nature of graphene gave rise to some of its exotic and favorable aspects that are lacking in its bulk counterpart, graphite. Since then, the 2D materials library has been greatly expanding to include transition metal chalcogenides (MoS_2, MoO_3, $MoSe_2$, WS_2, WSe_2),[83–85] hexagonal boron nitride, and other elemental p-block materials such as silicene, germanene, phosphorene and so on.[86–89] Interestingly, more than half a century after Feynman's lecture, researchers are now able to synthesize monolayers of various types and to stack layers of different materials on top of each other in desired orientations. Thereby, researchers are able to engineer novel 3D solids with unprecedented properties.[90, 91]

8.1 Classification of materials based on dimensions

The shrinkage of the dimensions of materials to the nanometer range has an enormous impact and industrial potential deriving from the fact that new and fascinating properties emerge at the nanoscale due to quantum effects. Nanostructured materials are low-dimensional materials comprising of building units of a nanoscale size (<100 nm) at least in one direction. Hundreds of novel nanostructured materials have been obtained in the past two decades, and the need in their classification is ripened.[92, 93] The classification is based on the number of dimensions

which are not confined to the nanoscale range, such as zero-dimensional (0D) quantum dots, one-dimensional (1D) nanowires, and 2D layers or sheets. Those different nanostructured materials exhibit dimension-tunable electronic and optical properties, which are important attributes in nano-device applications. Therefore, dimensionality is a major feature that discriminates various types of nanostructures; not only it defines the atomic structure of a material, but it also determines its properties to a significant degree. Consequently, the same chemical element or compound can exhibit different properties in different dimensions.

8.2 Graphene: The father of 2D materials

During the first decades of the twentieth century, the existence of 2D materials was a highly debated issue in the physics community. According to Landau and Pierls, 2D materials are thermodynamically unstable at any finite temperature due to thermal lattice fluctuations which would most likely decompose the crystal.[94, 95] Later on, this argument was expanded by Mermin[96] and it was supported by experimental observations that the melting temperature of thin films rapidly reduces with decreasing film thickness.[97] Only the successful isolation of graphene from its mother crystal graphite in 2004 ruled out the doubts on the possible stability of 2D materials.

Graphene is a single, tightly packed layer of carbon atoms that are bonded together in a hexagonal honeycomb lattice, Figure 8.1. It is perhaps the most investigated material in the past decade due to its huge advantages over conventional materials in electronics industry. One reason is the extremely high mechanical strength of the graphene sheet; the C-C bonds in graphene are about 25% stronger than in diamond. Another reason is that graphene has a peculiar electronic structure. It is neither a semiconductor nor a metal, rather it is exactly in between, and can be called a semimetal. It does not show a band gap, but the density of states is zero at the Fermi level. The electronic bands cross the Fermi level near the six corners of the hexagonal Brillouin zone (BZ). At these points, the dispersion relation, *i.e.* the change of the electron energy of a band within the BZ, is linear (see Figure 8.1). Such a feature leads to a zero effective mass for electrons and holes near these six points, *i.e.* the electrons and holes behave as if they are massless or relativistic particles, so-called Dirac fermions, and are described by the Dirac equation. The six corners of the BZ are called Dirac points. The cones at the Dirac points are located at the high symmetry K points in the BZ of the honeycomb lattice. This has shown to lead to electron mobilities a hundred times larger for graphene[98] with a potential for much faster electronics than with conventional silicon. However, the main drawback in graphene is its lack of a controllable band gap which makes it not suitable for the use as an electronic switch. Therefore, to use graphene in future nanoelectronic devices, a band gap will need to be engineered into it without compromising any of its other properties. Doping, functionalization, and substrate-induced band gap opening are among the most common techniques and methods reported.[99–101]

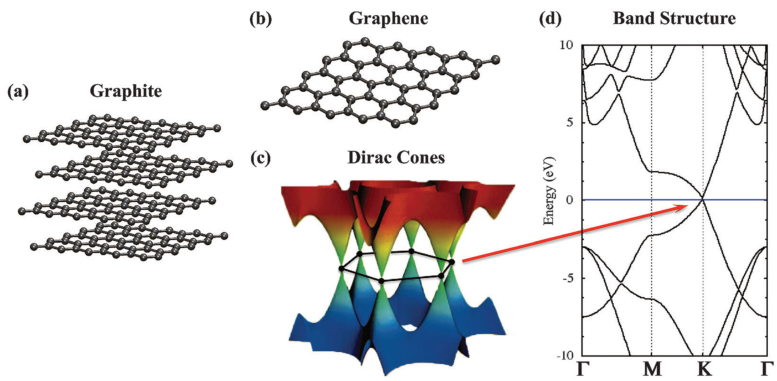

Figure 8.1: Band structure and ball-and-stick model of graphene. (a) Graphite structure (b) Graphene structure. (c) Dirac cones in graphene (d) Graphene band structure along the linepath (Γ-M-K-Γ). The Fermi level has been shifted to 0 eV and depicted with a blue horizontal line.[102]

One question after the discovery of graphene and its fascinating properties would be: Why not the formation of 2D sheets of atoms from group IV of the periodic table, *i.e.* why not silicene or germanene, the silicon and germanium analog of graphene? Since elements are grouped in the periodic table according to the periodic trends in their physical and chemical properties, carbon, silicon, germanium, tin and lead are expected to have certain similar properties. One reason behind the disregard of graphene-like silicon or germanium materials is related to the types of bonding that are common for carbon and not for silicon, germanium, or other group IV elements.

8.2.1 Hybridization of atomic orbitals

Carbon has two naturally occurring crystalline structures or allotropes, graphite and diamond. Although they are both entirely composed of carbon atoms, those two materials do not seem to have a lot in common. Diamond is clear or transparent and nearly a perfect electrical insulator while graphite is black and a great conductor of both heat and electricity. The differences between these substances all derive from the arrangement of their atoms.

A carbon atom has 6 electrons. In the atomic ground state, the 6 electrons are in the configuration $1s^2 2s^2 2p^2$, *i.e.* 2 electrons fill the inner shell $1s$ that is close to the nucleus and that is irrelevant for chemical reactions, whereas 4 electrons occupy the outer shell of the $2s$ and $2p$ orbitals. When a carbon atom gets ready to form bonds with other atoms, hybridization of its orbitals takes place. Hybridization increases the volume of the lobes interacting with other atomic orbitals, and this increase in overlap strengthens the bond and hence stabilizes it. In the case that a carbon atom forms four bonds with four other atoms, it needs to create four *hybrid* orbitals.

For hybridization to take place, the $2s$ orbital must combine with the $2p_x$, the $2p_y$, and the $2p_z$ orbitals to form four identical sp^3 hybrid orbitals (Figure 8.2a), having 25% of s-character and 75% of p-character. Since the carbon atom has 4 valence electrons, each electron fills one sp^3 hybrid orbital. The carbon which has undergone hybridization is ready to interact with four orbitals and adopt a tetrahedral geometry with bond angles of 109.5°. This is the case of diamond which makes it extremely rigid and a strong crystal. In the case that a carbon atom forms three bonds, one $2s$ orbital and only two $2p$ orbitals take part in the hybridization process. This hybridization forms three energetically equivalent sp^2 hybrid orbitals, which adopt a trigonal planar geometry with bond angles of 120°, leaving one p-orbital unchanged that sets at a right angle to the plane of the hybrid orbitals. Graphite undergoes the sp^2 hybridization and the carbon atoms form a 2D sheet of hexagons in which each atom has one unpaired electron left over. Those electrons will go freely across the matrix of atoms if one applies an electric current allowing it to readily conduct electricity.

Silicon [[Ne]$3s^2 3p^2$] and germanium [Ar] $3d^{10}4s^2 4p^2$, on the other hand, lie below carbon in the same group in the periodic table. Therefore, they have the same number of valence electrons as carbon. However, the energy difference between the valence s and p orbitals is lower. For instance, the energy difference in silicon is only half of the corresponding value for carbon, *i.e.* (Si (E_{3p} - E_{3s} = 5.66 eV) and C (E_{2p} - E_{2s} = 10.60 eV)).[103] Because of this difference in energies, there arises the difference in π bonding capabilities. As a consequence, silicon tends to utilize all of its three p orbitals resulting in sp^3 hybridization. In other words, $3s$ in silicon can easily mix with all the subshells of $3p$ ($3p_x$, $3p_y$, $3p_z$). While carbon activates one valence p orbital at a time as required by the bonding situation, giving rise to three possibilities of hybridization sp, sp^2, and sp^3.

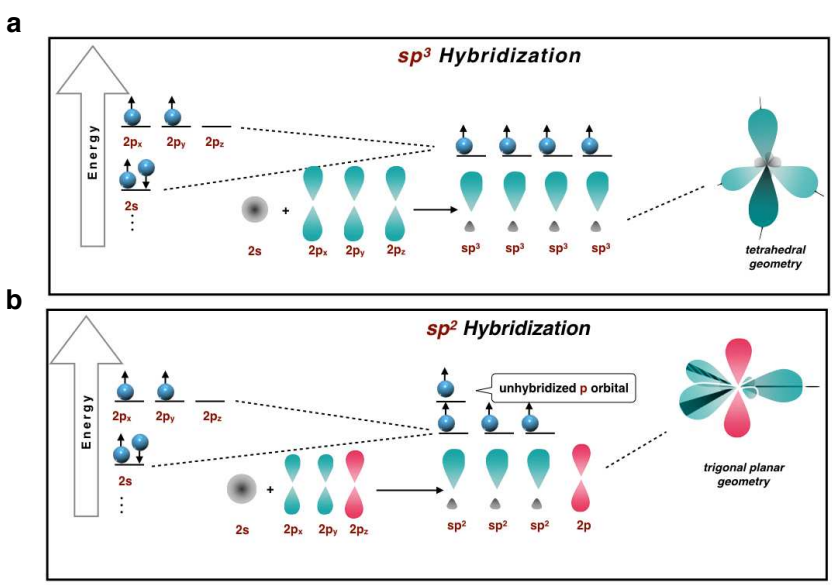

Figure 8.2: Hybridization of atomic orbitals. (a) sp^3 hybridization. (b)sp^2 hybridization.

Therefore, the key to making graphene-like silicon or germanium materials is to take a broader view of two-dimensionality, that is to say, one is not *strictly* looking for the elusive sp^2 bonding in silicon or germanium.[104]

8.3 Silicene and germanene: novel 2D materials

8.3.1 The crystal structure

Silicene and germanene are novel 2D allotropes of silicon and germanium, respectively. They have a honeycomb structure that resembles that of graphene. However, the resemblance is not perfect; silicene and germanene are buckled while graphene is perfectly planar. The buckling parameter is defined as the vertical distance between the two planes of Si or Ge atoms in the same layer (see bottom panel in Figure 8.3-a). There are two main reasons why buckling occurs in silicene and germanene and not in graphene. First, Si or Ge atoms prefer sp^3 hybridization over sp^2 which pulls bond angles from 120° towards 109.5°. Second, the distance between Si or Ge atoms in silicene or germanene becomes rather large to maintain a strong π-bonding. Hence, silicene and germanene exhibit a mixed sp^2-sp^3 hybrdization. Figure 8.3 illustrates the lattice structure and the buckling nature of free-standing silicene and germanene. The calculated lattice constant and buckling parameter are found to be about 3.83 Å and 0.44 Å for silicene, 3.97 Å and 0.65 Å for germanene, respectively. Free-standing silicene and germanene have a similar electronic structure to graphene, that is to say, near the Dirac point, the electronic dispersion relation is linear (see Figure 8.3).

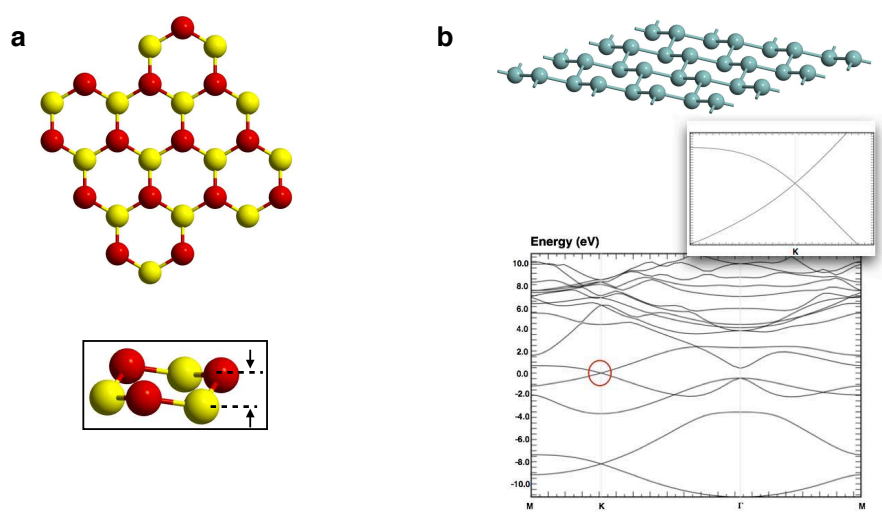

Figure 8.3: Free-standing silicene and germanene. (a) Top view of the silicene hexagonal structure. Red and yellow atoms represent the higher and lower atoms, respectively. The buckling is highlighted in one hexagon in the bottom panel. (b) Inclined view of the germanene lattice structure and its band structure. A zoom into the vicinity of the Dirac point shows the linear bands of germanene.

8.3.2 A brief history

Research on silicene from the experimental and theoretical communities got a real boost after its experimental synthesis on substrates only in 2012,[105] leaving silicene with a relatively short history. Despite that, both silicon and germanium materials were first investigated in 1994 as an infinite 2D Si and Ge corrogated stage, a decade before the emergence of graphene, by Takeda and Shiraishi using first-principles total-energy calculations.[106] In their work, the authors have shown the preference of Si and Ge to form a buckled structure, unlike C atoms in graphene which prefer to remain flat. However, there work was ignored for almost a decade because there was a long standing belief that materials with a monolayer thickness were thermodynamically unstable and could not exist.[94, 95].

Even before the term "silicene" was given, 1D structures of silicon were first synthesized on a Ag (110) surface by Leandri *et al.*[107] In 2007, Si-based structures were investigated using Tight-Binding Hamiltonians by Guzmán-Verri and Lew Yan Voon.[108] They have shown that silicon graphene-like sheets exhibit linearly crossing bands at the Fermi level and the name "silicene" was used for the first time in this study. In 2009, Cahangirov *et al.* reported a study based on first-principles calculations on the stability of both planar and buckled silicene and germanene structures.[109] Their calculations on the phonon dispersions showed imaginary frequencies for the planar structures clearly indicating their instability, while all phonon modes were positive for the buckled ones. This denoted that buckled silicene and germanene had restoring forces to any possible deformation contrary to the planar structures that were unstable. Inspired by the theoretical prediction of the stability of silicon structures with sp^2-like hybridization (buckled structures) and its promising electronic properties, Le Lay *et al.* continued to study the deposition of Si onto silver substrates to form silicene nanoribbons [110–112]. In 2010 and after the Nobel Prize in Physics was awarded to Geim and Novoselov for their work on graphene, research on silicene and other 2D materials had received a strong boost. Many theoretical studies appeared: investigations on the properties of hydrogenated silicene and germanene,[113] on the possibility to tune the band gap of silicene and germanene by the application of an electric field perpendicular to the sheet,[114] and on the quantum spin Hall effect in silicene and germanene.[115] The first compelling experimental evidence for the existence of a silicene monolayer was reported by Vogt *et al* in 2012 by depositing silicon atoms on a Ag (111) substrate.[105] In this work, a 3x3 supercell of silicene perfectly matched with the 4x4 supercell of the Ag (111) surface and agreed with DFT geometry optimizations. Even though there was a previous attempt to grow silicene on Ag (111) in 2010 by Lalmi *et al.*, their results, based on STM measurements, showed a silicene monolayer with a relatively short lattice parameter, [116] and their results were questioned by Vogt *et al.* Moreover, many groups reported the experimental realization of silicene on Ag (111) surfaces and showed the emergence of other phases of silicene as a result of the variation of the experimental conditions.[117, 118] Not only on silver surfaces, silicene was also experimentally synthesized on other metallic surfaces such as zirconium diboride thin films[119] and on an Ir(111) substrate.[120]

On the other hand, the first reports on the synthesis of germanene date back to 2014. The first paper, by Li *et al.*, reported the growth of germanene on a Pt (111) substrate,[121] and a second one, by Davila *et al.*,[122] stated its synthesis on Au (111). After several days, another paper appeared, by Bampoulis *et al.*, reporting the formation of germanene honeycomb structure

terminating the Ge-Pt clusters.[123] Finally, in 2015, Deviraz *et al.* synthesized a continuous germanene layer on an Al(111) surface.[124]
Silicene and germanene have been almost exclusively grown on metallic substrates. On metals, their 2D Dirac character is, in most cases, either altered or completely destroyed because of the hybridization of the relevant electronic states near the Fermi level with electronic states of the metallic substrates.[125–127] Besides, the epitaxial growth of silicene on Ag substrates has been recently questioned.[128–130] It was reported that Si atoms strongly interact with the Ag substrate and penetrate into the first layer of the Ag surface, expelling Ag atoms and inducing reconstructions, faceting, or growing reconstructed islands inside the first layer rather than remaining on top of the substrate. These observations imply that the growth dynamics of an ultrathin silicon layer on any metal substrate is extremely complicated and does not necessarily result into genuine silicene.

8.3.3 Our attempts to grow genuine silicene and germanene

To date, however, reports on the successful growth of germanene and silicene on nonmetallic substrates are rather scarce. A single report on the growth of germanene on MoS_2[131] appeared while our work on germanene was still under review. In view of a viable solution to the above-mentioned issues associated with metallic substrates, we use in our work a highly oriented pyrolytic graphite (HOPG) substrate that, due to its sp^2 configuration, approximates well the electronic and structural properties of a fully honeycombed structure of silicon and germanium. Moreover, HOPG is chemically inert, and this is expected to avoid alloy formation, *i.e.*, intermixing of Ge or Si and C atoms which can easily occur on metallic substrates.

8.4 Outline of Part II

Chapters 9 and 10 are devoted to our theoretical and experimental studies of silicene and germanene, respectively. The following two chapters are presented in a different way; *i.e.*, for each study performed, the method is described at the beginning of the section followed by the corresponding results and discussions. Moreover, we refer the interested reader to Appendices A and B for a theoretical background on molecular dynamics simulations and DFT methods, respectively, and to Appendices E and F for basic concepts in solid state systems and for an overview of the experimental techniques used in the present work, respectively.

Chapter 9

Formation of Silicene Nanosheets on Graphite

In this chapter, we present and discuss our results on the growth of silicene nanosheets on top of HOPG surfaces based on a combined experimental and theoretical work. We provide strong evidence that 2D alloy-free silicene is formed. However, before we go ahead and discuss the above-mentioned study, let us present our theoretical results we have obtained, in the first place, on the interaction of silicon atoms with one particular metallic substrate: the silver surface.

9.1 Theoretical results

9.1.1 Si atoms on a Ag(111) surface

This study aims at the investigation of the interaction of Si atoms with a Ag surface. It was performed in the midst of all the experimental work published on the claimed growth of a silicene sheet on Ag (111) surfaces. During this period, no research work argued the growth of silicene on Ag (111), except for the debate on its electronic properties.[1] From a theoretical approach, we decided to take a closer look at the interaction of Si atoms on Ag (111), but from a dynamical one. This study was crucial due to 1) the lack of molecular dynamics simulations of the silicene growth on metallic surfaces, and 2) the prominence of dynamical studies, not to mention *ab initio* ones, where one is able to "visualize" the motion of atoms at the atomic scale as chemical reactions occur.

AIMD simulations were performed, at quasi realistic experimental conditions, as follows. We have started with a (8×4) four-layer slab[2] Ag (111) surface previously heated to 500 K using a thermostat.[132] We randomly placed 6 Si atoms on top of the surface and followed their trajectories for 4 ps. In Figure 9.1, we show snapshots from the trajectory at different molecular

[1] The debate on the electronic properties are briefly presented in the general introduction of part II, Section 8.3.2.

[2] A slab model is described in Section E.5 of Appendix E.

dynamics (MD) steps. Let us follow the behavior of the two Ag atoms in the top layer marked as 1 and 2. Figure. 9.1-a is a snapshot after 217 MD steps, *i.e.* after 0.217 ps. Here, we find Si atoms move on top of the surface and strongly interact with Ag atoms in the top layer. After 1.4 ps, Figure 9.1-b, the strong interaction between Si atoms and Ag_1 atom causes Ag_1 to start to move out of the surface and Ag_2 to move to the right side, *i.e.* to get closer to Ag_1. After 3 ps, Figure 9.1-c, Ag_1 is pulled out of the surface and Ag_2 tries to fill the vacancy left behind Ag_1. Finally, after 3.6 ps, we clearly see how Ag_1 is released from the surface, Ag_2 sits in its place, and one Si atom quickly "sneaks in" and substitutes Ag_2. This Si atom binds to the Ag atoms in the top layer and the second layer, marked by a green arrow in Figure 9.1-d. Here we would like to note that such behavior is well reproduced in our simulations. We have modelled another Ag (111) surface, a (8×8) Ag(111), and we have obtained exactly the same representative behavior.

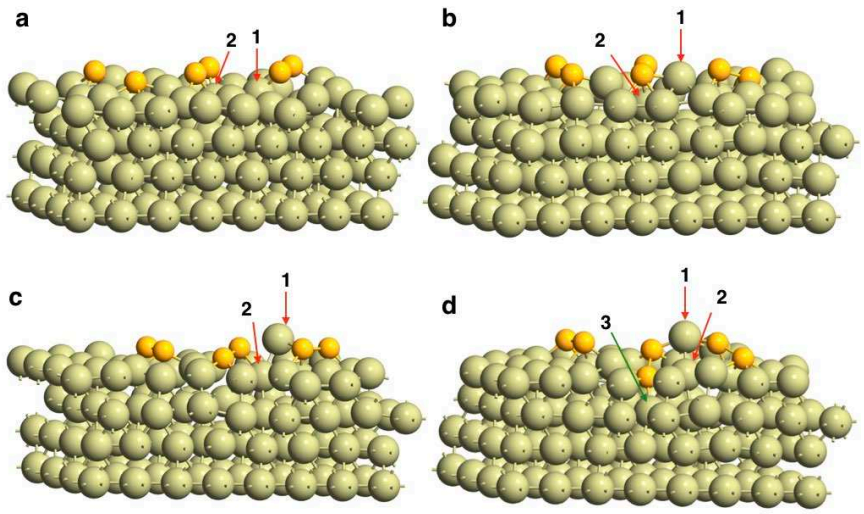

Figure 9.1: AIMD snapshots of 6 Si atoms on Ag(111). (a) After 0.217 ps. (b) After 1.4 ps, a strong interaction between Si and Ag_1 causes Ag_1 to slightly move out of the surface. (c) After 3 ps, Ag_1 is pulled out and Ag_2 fills the vacancy behind. (d) After 3.6 ps, a Si atom substitutes the Ag_2 atom in the top surface layer. Si atoms are shown in yellow and Ag atoms in light green.

We continued our AIMD investigations and added 6 more Si atoms to the structure obtained after 4 ps. Figure 9.2-a shows a snapshot of the trajectory taken after 2 ps from the addition of the additional 6 atoms. Here, we find that the Si atoms continue to interact strongly with the top Ag atoms expelling them out of the top surface layer. Now, we have two Si atoms (marked with blue arrows) filling sites of the Ag top layer. After 3.9 ps, Figure 9.2-b, we find three Si atoms bonding together inside the first layer of the surface of the substrate.

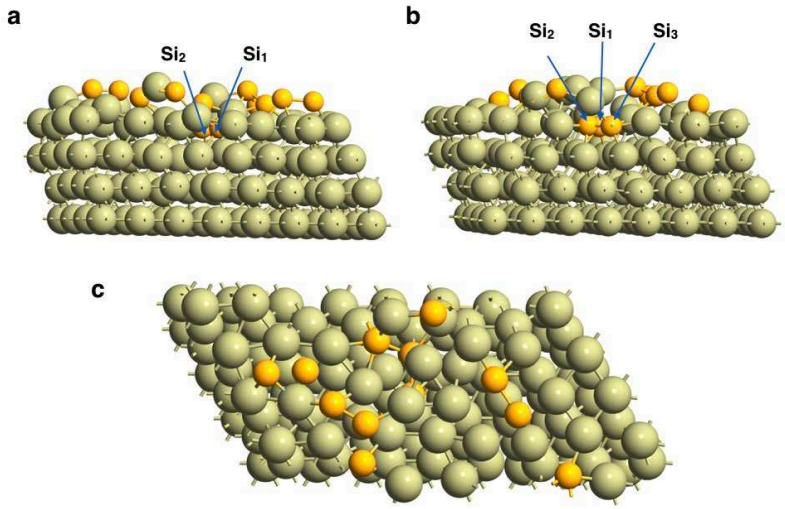

Figure 9.2: Typical AIMD snapshots of 12 Si atoms on Ag(111). (a) After 2 ps, two Si atoms (marked with blue arrows) filling the sites of the Ag top layer (b) After 3 ps, three Si atoms bond together with other Ag atoms in the top surface layer. (c) top view of (b). Si atoms are shown in yellow and Ag atoms in light green.

In addition, we have compared the effect of the interaction of Si monomers, dimers, and trimers on the Ag surface. First, we heated a (8×8) three-layer slab Ag (111) surface to 500 K. After several ps of equilibration at 500 K, we placed Si atoms and followed their trajectories for several ps. The mostly reported structure in the literature was the (4×4) superstucture, which is also known as (3×3) silicene on top of (4×4) Ag. This superstructure consists of 18 Si atoms and 16 Ag atoms per Ag layer. In our simulations, we took twice the size of the Ag superstructure. To consider a full coverage or 1 monolayer (ML) of silicene on top of a (8×8) Ag surface, we need 36 Si atoms. Here, we studied the case of 2, 4, 6 and 12 Si atoms that correspond to a coverage of $\sim$ 0.05 ML, 0.11 ML, 0.2 ML, and 0.3 ML, respectively. We took into account Si monomers, dimers and trimers interacting with the surface. Figure 9.3 shows a plot of the mean square displacement of the top Ag atoms averaged over several MD steps, and calculated for different Si coverages as well as for the different cases of Si. We noticed that a strong displacement of the Ag atoms takes place due to Si monomers and this displacement increases with the increase of the number of Si atoms added. For the dimer and trimer cases, we found a weaker effect on the displacement of the Ag atoms relative to the monomer case. This finding shows that mostly Si monomers are responsible for the modification of the Ag surface and the expelling of Ag atoms.

Our findings demonstrate that the Ag (111) surface is strongly modified upon the interaction with Si atoms. Our simulations reveal that Ag atoms are released from the surface and Si atoms become members of the top substrate layer. Those results have contradicted all previously reported ones which always describe the formation of a silicene sheet on top of an *unreconstructed* Ag surface. Our MD simulations suggest that the formed silicene sheet corresponds to an alloyed structure, that is, a mixture of Si-Ag atoms, and not to a pristine silicene sheet.

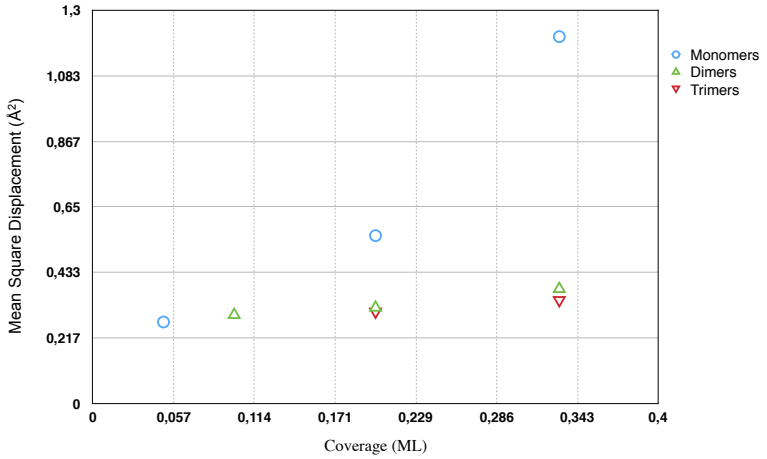

Figure 9.3: Mean square displacement of the top Ag atoms averaged over several MD steps as function of Si coverage investigated separately for Si monomers, dimers and trimers.

While we were in the course of the analysis of our results, a letter by Prévot *et al.*[128] took us by surprise! The authors had done a real-time scanning tunneling microscopy (STM) study of the deposition of Si on Ag (111), under the same experimental conditions previously reported for the growth of a silicene sheet, and had confirmed our simulations! Their experimental work have shown a release of 65% of the surface Ag atoms from the Si covered areas. Their conclusion drawn from the structure of silicene grown on a Ag (111) surface corresponds to either Si-Ag alloys or to a Si plane covered with Ag atoms.

9.1.2 Silicene nanosheets on HOPG

Ab initio calculations were performed by using DFT within the generalized-gradient approximation (GGA) as implemented in VASP-5.3.5.[29] The PBE[31] with the van der Waals-D2[133] functional[3] was used to describe the exchange-correlation. The core electrons were described by the projector-augmented wave (PAW) method.[30] The plane-wave basis set was restricted to a cutoff energy of 400 eV.

9.1.2.1 Silicene/HOPG structure optimizations

The HOPG surface was modelled by a four-layer slab in ABAB stacking of graphene layers within periodic boundary conditions (PBC), keeping the bottom two layers fixed. The vacuum region is as thick as 2.0 nm. The entire system, silicene on top of HOPG, was fully relaxed by a conjugate-gradient method until the forces acting on each atom were less than 0.1 eV/nm. The convergence criterion of total energy for self-consistent field calculations was chosen to be 10^{-4} eV. We have used 3×3×1 and 9×9×1 k-point meshes including the Γ point in order to sample

[3]See section B.2.3 in Appendix B for a discussion on the dispersion interactions in DFT.

the supercells with 30° and10° rotation angles between the two hexagonal patterns, respectively. The calculations for the relaxed silicene on a graphite structure with a 30° rotation angle between the two hexagonal patterns, depicted in Figure 9.4, yield a 0.051 nm buckling of the silicene layer and its distance to the top layer of the graphite surface to be 0.333 nm. The silicene bond length is 0.225 nm and its bond angle is around 114°. The lattice parameters of silicene and graphite are 0.379 and 0.246 nm, respectively, in excellent agreement with our STM measurements obtained for RT deposition.

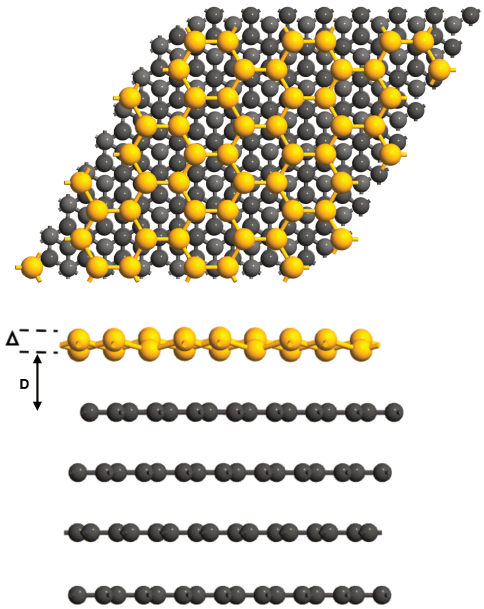

Figure 9.4: Atomic structure model of the silicene on HOPG system. Top and side views of the optimized structure obtained by DFT calculations which show the silicene layer at a distance D of 0.333 nm above the graphite surface with a buckling parameter (Δ) of 0.051 nm. Si atoms are shown in yellow and C atoms in grey.

Here we would like to note that the experimental work, based on STM, have shown different rotation angles between the silicene and graphite lattices. Due to the weak van der Waals forces holding the silicene to the graphite surface, one can actually imagine that the silicene layer is "floating" quite freely on top of the HOPG surface and, therefore, can assume different configurations for different silicene areas even on the same sample.

9.1.2.2 Electonic band structure calculations

Figure 9.5-a shows the calculated band structure of silicene on HOPG for a silicene area with about 10° rotation angle between the two hexagonal patterns in the M-K, K-Γ, and Γ-M directions, revealing one Dirac cone at the Γ point belonging to silicene. We stress that in the

free-standing case, the Dirac cone of silicene is at the K point as well as the Dirac cone of bare graphene.[109] When the silicene-graphene system is built, the Brillouin zones of both graphene and silicene are rotated with respect to the other. Hence, the K point of silicene falls onto the Γ point of the BZ of the silicene-graphene system. Our band structure is quite similar to the band structure of silicene on graphene, as calculated by Cai *et al.*[134] The latter also showed that the p_z states of Si are responsible for the π bonds in the vicinity of the Fermi level and that the Dirac cone of silicene is mapped to Γ while the Dirac point of graphene stays at the K point. Furthermore, the calculated Dirac cone of silicene on HOPG is somewhat shifted above the Fermi level, which can be attributed to a slight charge transfer between silicene and its substrate. Free-standing silicene is predicted to have a band gap of 1.55 meV.[115] When silicene is formed on graphite, we find that this gap increases to about 37 meV; that is, it is quite comparable to the silicene band gap on graphene of 57 meV.[134] Consequently, we can conclude that increasing the number of graphene layers in our graphite surface model would not affect the band gap in the silicene sheet and that the small interaction occurs only between the silicene sheet and the top graphite layer. This energy gap is induced by the substrate, which partially breaks the sublattice symmetry of silicene due to the inhomogeneous van der Waals interaction. The band structure of silicene on HOPG with a 30° rotation angle between the two hexagonal patterns in Figure 9.5-b shows the Dirac cone of silicene at the Γ point, slightly shifted above the Fermi level with a band gap of about 48 meV.

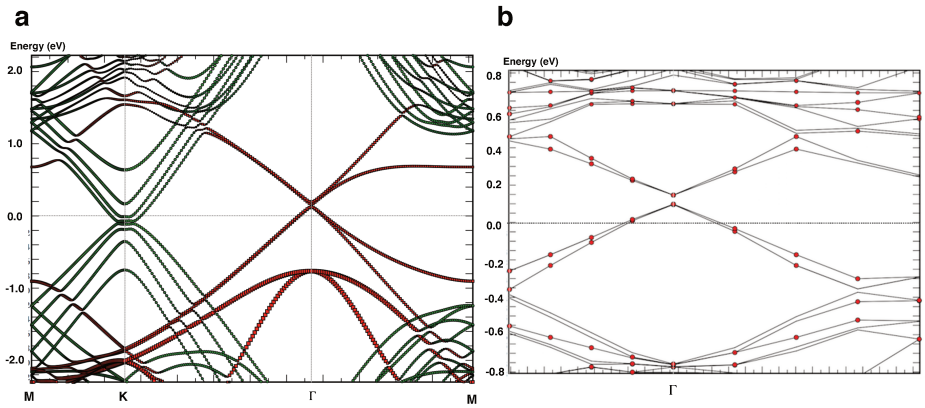

Figure 9.5: The electronic band structure calculated from DFT. (a) Band structures of silicene on graphite with a 10° rotation angle between the two hexagonal patterns; projected bands of Si and C are highlighted in red and green, respectively. (b) Band structures of silicene on graphite with a 30° rotation angle between the two hexagonal patterns highlighting the Dirac cone of silicene at the Γ point.

9.1.3 Molecular dynamics simulations

9.1.3.1 Thermal stability of a silicene sheet on HOPG

To demonstrate the stability of the honeycomb structure for silicene on HOPG, we have performed AIMD simulations within the canonical ensemble, using the Nose-Hoover thermostat for

temperature control.[132] A (2×2) supercell model of a silicene monolayer on HOPG (*i.e.*, 2 times the length of the optimized silicene on the graphite system, with a 10° rotation angle between the two hexagonal patterns in both x- and y-directions) with dimensions of 1.3 nm×1.3 nm, was at first fully optimized with standard *ab initio* methods. Then, we carried out our AIMD simulations, with a time step of 1.0 fs, at RT and at 350°C for more than 3 ps. Our simulations reveal that the silicene layer remains stable even at temperatures well above RT (see Figure 9.6). While the in-plane hexagonal lattice structure of silicene is preserved for both temperatures, we find that the buckling of the silicene sheet slightly increases with temperature.

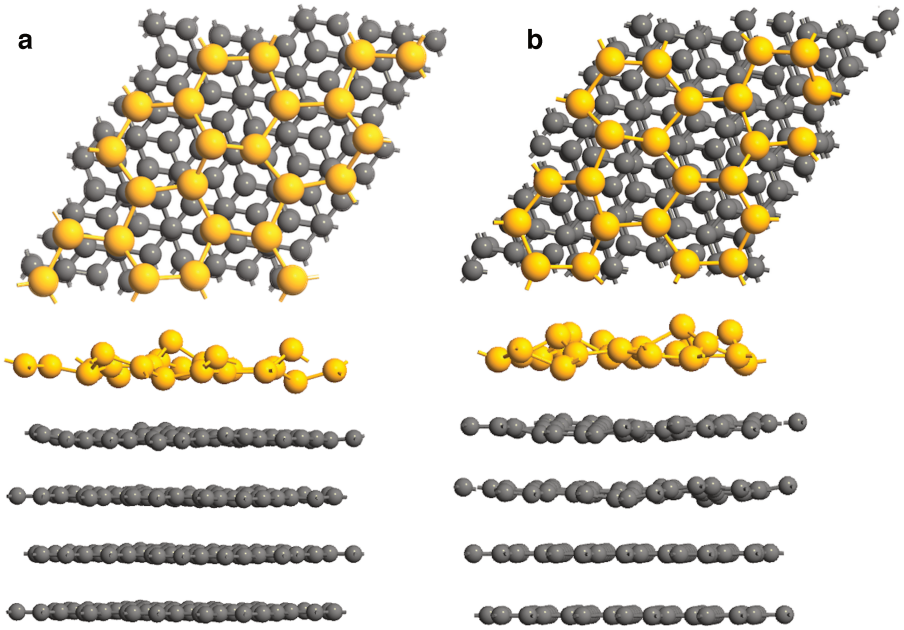

Figure 9.6: AIMD snapshots of a silicene sheet on HOPG. (a,b) Snapshots from AIMD simulations showing the structure (top and side views) obtained at RT (a) and at 350°C (b), revealing the stability of the silicene layer well above RT.

To investigate the stability of silicene at elevated temperatures for some time in experiments, we carried out AIMD simulations. Here, we would like to point out that the time scale in the AIMD simulation method is on the order of picoseconds, which is too short compared to the time scale in experiments; therefore, we have chosen to study the stability of the system at extremely high temperatures. To this end, we heated the silicene on graphite system from 25 to 725°C during 5.6 ps, and then we applied a thermostat to keep the temperature of the system stable around 725°C for 4.58 ps. We noticed that the silicene structure did not break apart and did not convert to a 3D structure, but Si atoms remained intact in the honeycomb lattice. The relatively high stability at this extreme temperature suggests that our system should remain stable over relatively long times at less elevated temperatures.

The thermal stability of the silicene monolayer even above RT underlines the essential contribution of the van der Waals forces binding the silicon atoms in a honeycomb pattern to the graphite surface. From our simulations of a perfect silicene sheet on top of HOPG, we did not perceive any 3D silicon cluster formation even at 350°C. Therefore, we will take a closer look at the details of the growth dynamics below. At this point, however, we can already conclude that a perfect silicene sheet remains stable at such a high temperature of the substrate, supporting the STM measurements (see Figure 9.10 below) where silicene zones were observed in many regions.

9.1.3.2 Growth of a silicene sheet on HOPG

In order to go deeper in the atomic-scale view of the growth process of the silicene layer on HOPG, we have carried out AIMD simulations under quasi realistic experimental conditions. In the experiments, Si atoms were evaporated at an extremely small deposition rate (0.01 nm/min); that is, a deposited Si atom will have lost all of its initial impact information a long time before the next Si atom will arrive. Consequently, we have started the simulation of the growth mechanism with Si atoms randomly positioned on top of the graphite surface and not by explicitly simulating the deposition process atom by atom. It is necessary to introduce such a model because it is impossible to follow the growth with AIMD methods on a time scale of several minutes. To comply with the experimental conditions, we have started the simulations with a coverage of Si atoms above the graphite surface, which was less than 1 ML, followed the system evolution at RT, and then added Si atoms successively until we reached a 1 ML coverage as in the experiment.

In Figure 9.7, we present the general trends observed during the growth. The initial structure consisted of a 0.75 ML of Si atoms, that is, 18 Si atoms, randomly distributed at about 0.35 nm above the graphite surface with relatively large lateral distances between them, such that the initial interaction between those Si atoms before moving was negligible, as depicted in Figure 9.7-a. Following the trajectories for 900 MD steps (0.9 ps evolution time), we can notice from Figure 9.7-b how Si atoms bind together in a long chain (black ellipse), while other Si atoms move closer to each other to form the first hexagon (red circle). After 1 ps of system evolution from the starting configuration, three Si atoms were added on the bare regions of the graphite surface to have a 0.88 ML coverage. We notice that two hexagons are formed (red circles) along with small polygonal rings after 900 MD steps (Figure 9.7-c). After another 1 ps, three more Si atoms were added to get a 0.96 ML coverage. Figure 9.7-d is a snapshot of the structure resulting from its self-organization after about 1300 MD steps. Nearly all Si atoms in the system now bind in a hexagonal network with one large polygon (black ellipse). Finally, after around 1.4 ps of system evolution, one more Si atom was added in a random location to reach a full coverage (1 ML). Figure 9.7-e is a snapshot of the system trajectory after an additional 633 MD steps showing the honeycomb network of the silicene monolayer with only little defects. The formed silicene sheet lies about 0.4 nm above the HOPG surface, which agrees very well with our STM measurements.

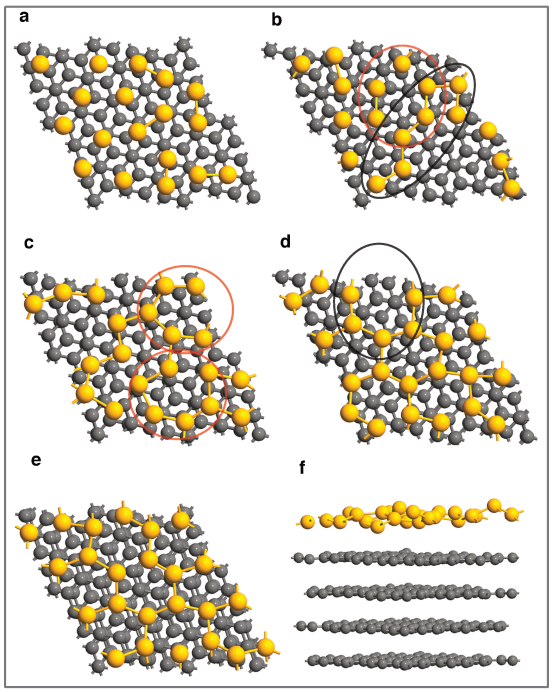

Figure 9.7: Typical snapshots from AIMD simulations of the epitaxial growth of a silicene monolayer on HOPG at RT. (a) Initial configuration: 0.75 ML coverage of Si atoms randomly distributed above the graphite surface. Silicon atoms are shown in yellow and carbon atoms in grey. (b) Structure after 0.9 ps of self-organization: one hexagon of Si atoms starts to form. (c) Structure with 0.88 ML coverage of Si atoms after 1.9 ps clearly showing two hexagons forming. (d) Structure with 0.96 ML coverage of Si after 3.3 ps. (e) Structure with 1 ML coverage of Si after 3.9 ps showing that the silicene region formed with only few defects. (f) Side view of (e) underlining the flatness of the silicene sheet at RT.

Two different growth mechanisms, obtained experimentally, are unveiled in the AIMD simulations: a two-dimensional one where a silicene sheet was observed and a three-dimensional one where 3D silicon islands were formed. We can explain these growth mechanisms as follows: the lower the temperature of the graphite surface, the more perfectly a 2D plane based on van der Waals forces is defined. If the temperature gets so high that the out-of-plane vibrational amplitude of the carbon atoms gets anywhere close to half of the Si-Si interatomic distance, the van der Waals potential will no longer define a plane, but rather a volume, favoring the onset for the formation of 3D Si clusters. To confirm this hypothesis, we checked the maximum vibrational amplitude of carbon atoms in the top layer of the graphite substrate and found it to be around 0.04 and 0.10 nm for RT and 350°C, respectively. Consequently, we propose tentatively that perfect 2D silicene layers cannot be created on HOPG at substrate temperatures exceeding well above 350°C. Moreover, we have carried AIMD simulations at lower temperatures. Here, we found that by decreasing the temperature, even down to -225°C, we obtain a spontaneous organization of Si atoms above the HOPG surface. However, for all temperatures below RT, the formation of hexagons was accompanied by other polygons such as pentagons and heptagons. Therefore, we suggest tentatively that a temperature of 25°C presents the low-temperature limit

for the formation of a default-free honeycomb structure.
Interestingly, we have observed at an atomistic scale how Si hexagons spontaneously form on top of the HOPG substrate at RT. This growth mechanism only becomes possible due to the van der Waals interactions between silicon and carbon atoms which are strong enough to define a flat growth plane necessary for the silicene sheet formation, but weak enough to leave the silicene properties largely unchanged from the free-standing silicene case; that is, in the present system, one can create a stable silicene monolayer without any covalent bonds to its supporting substrate underneath.

9.2 Experimental results

- Preparation of HOPG surface: A HOPG (from GE Advanced Ceramics, USA, 12 mm×12 mm×1 mm) sample was used as a substrate. A fresh surface of graphite was obtained by peeling the HOPG substrate with a scotch tape in a nitrogen atmosphere and was then transferred into a UHV chamber.
- Deposition of silicon: High-purity silicon (Sil'tronix ST, ρ = 1-10 Ω·cm) was evaporated from a tungsten basket-shaped crucible located at 200 mm from the substrate. The deposition was done in UHV conditions (base pressure low 10^{-10} Torr) at a constant rate of 0.01 nm/min (0.04 ML/ min) monitored by an Inficon quartz balance (properly calibrated for the Si density and carefully positioned close to the sample holder). Deposition was carried out keeping the substrate at RT.

9.2.1 STM measurements

STM imaging was performed using an Omicron-STM system with electrochemically etched tungsten tips. The STM was calibrated by acquiring atomically resolved images of the bare HOPG substrate. All images were acquired in the constant current mode and were unfiltered apart from the rigid plane subtraction.
We present, in Figure 9.8-a,b, typical STM images obtained after one ML deposition of Si on HOPG kept at RT. We observe the formation of some small Si islands (very bright regions) rising above flatter zones. These flatter areas appear like a patchwork of hexagonal patterned regions with different lattice spacings. Their extension and size prevent their interpretation in terms of Moiré interference or other artifacts induced on the HOPG surface by the Si deposition. White circles in Figure 9.8-a evidence the areas with wider lattice spacing, while in the top-left corner, a hexagonal region with a lower lattice spacing is clearly visible. In Figure 9.8-c,d, we report the bi-dimensional Fourier transform of the two STM images. Both of them confirm the STM image texture observation, exhibiting the presence of two hexagonal arrangements rotated by 30° with respect to another. The observed external spots correspond to four {10} and two {-11} spots of the HOPG. Indeed, since the distance d_{10} (or equivalently d_{-11}) is equal to $\frac{\sqrt{3}}{2}a$, where a is the hexagonal lattice parameter, by measuring the distance between the spots and the center, we obtain a value of $a = 0.24 \pm 0.01$ nm that corresponds well to the lattice constant of carbon atoms arranged in a hexagonal pattern for a bare HOPG surface. The inner spots correspond

to the atoms arranged with a wider lattice parameter. The ratio between a couple of outer and inner spots is 1.71± 0.01, which is a factor of $\sqrt{3}$ of the HOPG hexagonal lattice parameter and corresponds to a lattice parameter of 0.41±0.02 nm. This is strong evidence in favor of the formation of a $(\sqrt{3} \times \sqrt{3})$R30° Si adlayer.

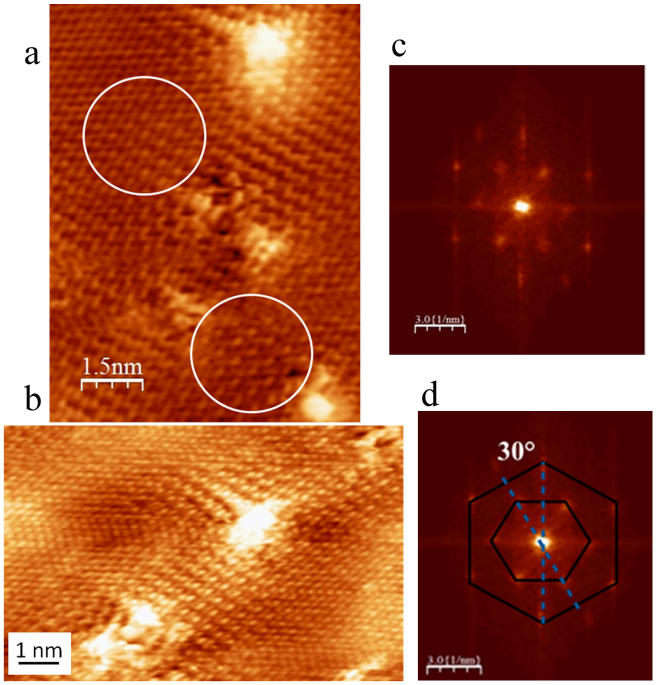

Figure 9.8: Scanning tunneling microscopy images of one monolayer silicon deposited on HOPG at room temperature. (a,b) STM images (collected with V_{sample} = +0.3 V, tunneling current, I_{tunn} = 0.3 nA) after one silicon monolayer deposited on a HOPG substrate at RT. Note the coexistence of silicene areas and small, 1 nm high, silicon clusters (white regions). (c,d) Bidimensional Fourier transform of the two STM images: two hexagons (the external one due to HOPG and the internal one due to silicene) can be noted to be rotated by about 30° with respect to each other.

To support this finding, we show in Figure 9.9-a the STM image and in Figure 9.9-b the corresponding Fourier transform of the bare HOPG substrate before Si deposition. It is worth noting that the Fourier transform presents only a single hexagonal pattern, giving a lattice parameter of 0.24 ± 0.01 nm. Interestingly, the Si adlayer hexagonal pattern of Figure 9.8 is different from that of the HOPG (see also the discussion of Figure 9.10 below), in which only one atom out of two of the hexagonal honeycomb structure is observed (note for comparison Figure 9.9-b and the HOPG atomic model in Figure 9.9-c). For HOPG, this is due to the characteristic alternation between filled and empty p_z orbitals normal to the surface, while for the Si adlayer, all Si atoms can be simultaneously observed, but at different heights, suggesting that the adlayer is not completely flat as for HOPG and presents a small buckling.

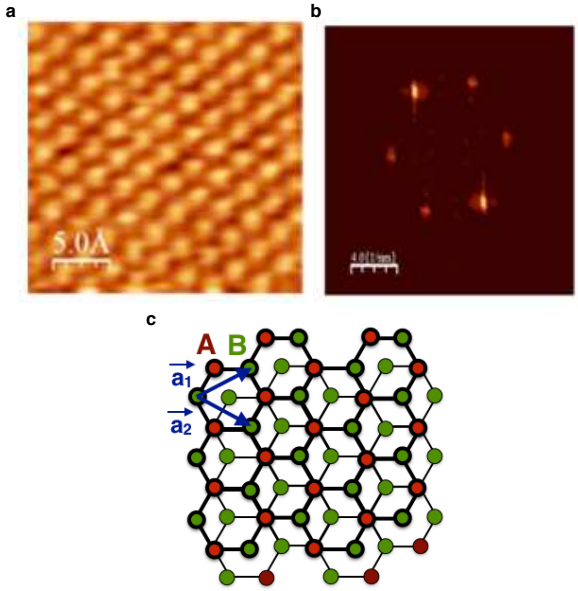

Figure 9.9: Scanning tunneling microscopy image of the bare HOPG substrate. (a) STM image of the bare HOPG before the deposition of the silicon adlayer exhibiting the characteristic hexagonal pattern in which only one atom of two of the hexagonal honeycomb structure is observed due to the characteristic alternation between filled and empty p_z orbitals normal to the surface. (b): Bi-dimensional Fourier Transform of the STM image of the HOPG surface. (c) HOPG atomic model.

Now let us take a closer look on a certain region on the surface. In Figure 9.10-a, we show the enlarged image of the central part of Figure 9.8-b, highlighting the honeycomb lattice of the Si adlayer in the region between two clusters. A ball-and-stick model representing the Si atom arrangement, with higher atoms in blue and lower ones in red, clearly shows a rotation of the lattice structure of the Si adlayer with respect to that of graphite. The experimental height of the Si honeycomb regions above the HOPG (indicated by a red arrow on the line profile shown in 9.10-b) is perfectly comparable with that obtained with our *ab initio* calculations (see above). Moreover, following the black horizontal line profile drawn in Figure 9.10-a, we identify the presence of the buckling of the silicon nearest neighbors, which results in about 0.05± 0.01 nm. This accounts well for the theoretical model of silicene in the low buckling configuration (as discussed in the theoretical part) and reported in the literature for free-standing silicene[109] and for silicene on graphene.[134] Besides the well-known growth of Si clusters[135] on HOPG and on epitaxial graphene on 6HSiC(0001),[136] we have observed genuine silicene regions in the present study. The most striking difference with the existing literature on silicene growth on metallic substrates is the absence of any atomic surface reconstruction and/or superstructure.[105]

Finally, we would like to point out an inherent problem with our recording of the STM images: at present, we have to operate our STM at RT. From our AIMD simulations (see above), we know that Si atoms that are bonded with van der Waals forces to the HOPG substrate experience much larger displacements around their equilibrium position than Si atoms that are bonded

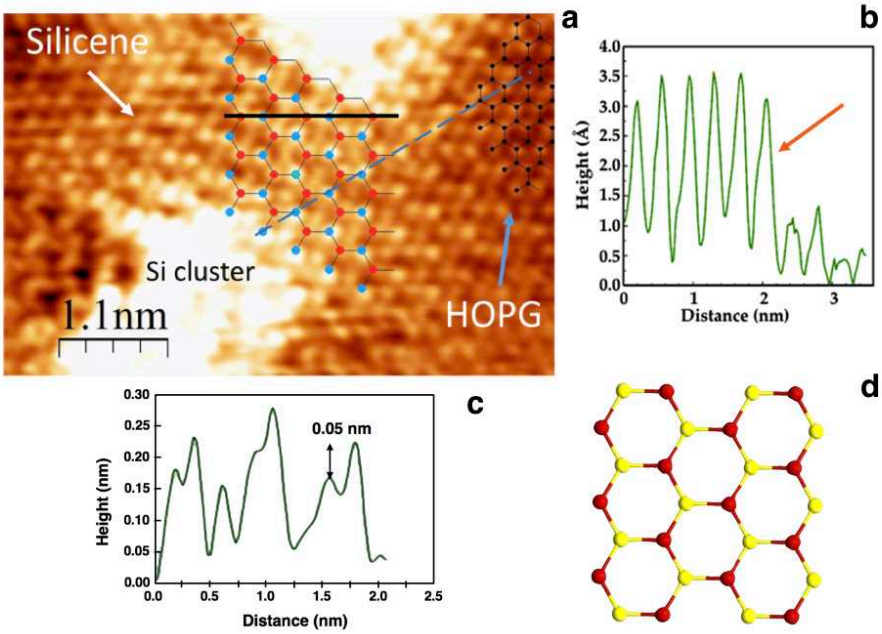

Figure 9.10: Scanning tunneling microscopy image of one monolayer of Si deposited on HOPG at room temperature. (a) STM image (collected with $V_{sample} = +0.3$ V, $I_{tunn} = 0.3$ nA) obtained with the HOPG substrate kept at RT during silicon evaporation. Ball-and-stick models have been superimposed on the image representing Si atoms (blue and red) and C atoms (black) for better understanding. (b) Line profile obtained along the blue dashed line drawn in (a). The red arrow indicates the height of the silicene layer with respect to the HOPG surface. (c) The line profile obtained along the solid black line drawn in (a) determines the presence of a buckling of about 0.05 nm of the silicon nearest neighbors. (d) Ball-and-stick model drawn for silicene with a low buckling of the honeycomb structure. Red balls represent the highest Si atoms, while the yellow ones are slightly lower in height.

covalently to a silver substrate. In order to achieve the same image quality as those previously published on silver, we estimate that we have to cool down our samples to about liquid nitrogen temperatures to reduce the large root-mean-square displacement.

9.2.2 STS measurements

The scanning tunneling spectroscopy (STS) measurements helped us to investigate the local electron density of states near the Fermi level. During the acquisition, the tunneling current was recorded as a function of the applied bias voltage (I *vs* V), the feedback loop was disabled, and the set-point current, which regulates the tip-sample distance, remained unchanged during the voltage scan. Current-voltage curves were collected over grids of points equally spaced on the scanned sample area, and the I-V spectra were averaged over a set of several curves.
In Figure 9.11, we show the current versus voltage curve obtained on the silicene region. The experimental curve in Figure 9.11-a is an average of many acquisitions, where several currents

and distances from the tip and the sample were used to discriminate the behavior of the silicene patches from the metallic character of the HOPG. It can be noticed that the silicene region reveals a metallic behavior. Figure (9.11-b) reports the normalized conductance that can be related to the local density of states (LDOS), and it reveals a finite density at E_F. We observe a zone of minimum number of states close to the Fermi level, which can be associated with the gap opening at the Γ point for silicene and at the K point for HOPG of the silicene/HOPG system. This result nicely agrees with the computed LDOS from the energy band structure (as discussed in the theoretical section) and reported in the same figure as a red dotted line.

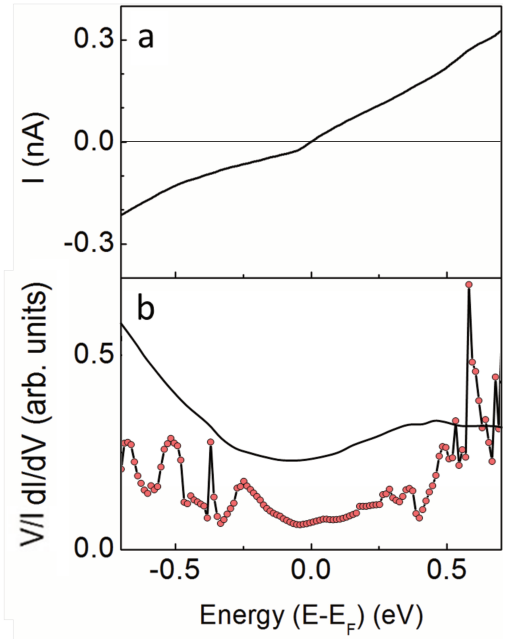

Figure 9.11: Scanning tunneling spectroscopy measurement. (a) I-V curve registered for silicene on HOPG. We observe a straight line around the Fermi level (located at 0.0 eV) showing the metallic character, *i.e.*, ohmic behavior. (b) Normalized conductance calculated from curve (a) related to the local density of states further confirming the metallic character of the obtained silicene. Red dotted line is the theoretical density of states computed through the energy band structure of the silicene/HOPG system as discussed above.

9.2.3 XPS measurements

The C 1s, Si 2p and Si 2s Xray photoemission spectra were measured *in situ* using a non-monochromatic Al Kα radiation source (1486.6 eV) and a double-pass cylindrical mirror analyzer operating in retarding mode. The energy scale was calibrated with reference to the binding energy of the Si $2p_{3/2}$ peak from a clean Si(100) 2×1 reconstructed sample and measured to be 99.5±0.9 eV with respect to the Fermi level.

In Figure 9.12-a we show the behavior of the Si 2p and Si 2s XPS core levels obtained after deposition of one ML of silicon at RT. We note that both Si peaks are highly symmetric and do not

show any additional components due to oxidation processes (located between 101 and 103.5 eV) or due to carburization reactions with the substrate to form Si(1-x)C(x) compounds.[137] This observation ensures the low reactivity of the Si deposition at RT with the graphite underneath.

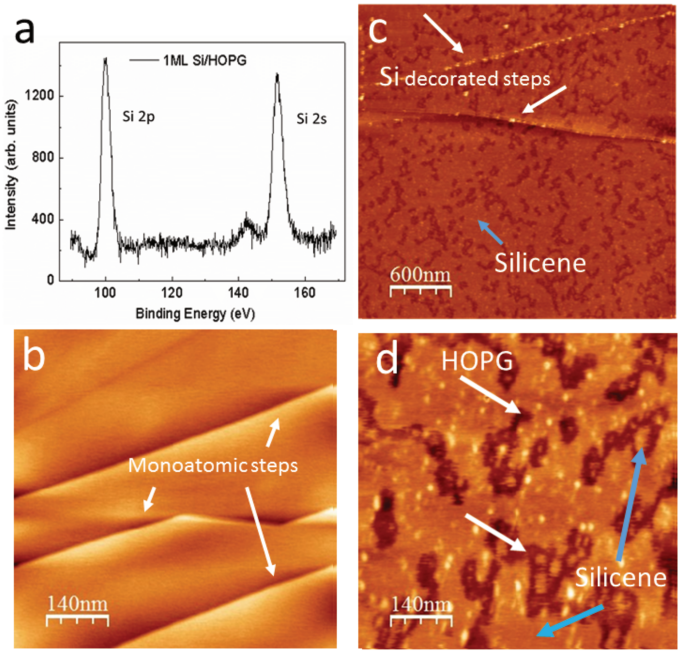

Figure 9.12: Xray photoemission spectra and atomic force microscopy images. (a) Si 2p and Si 2s XPS core levels obtained after the deposition of one ML of Si on HOPG at RT. We note that both Si components are highly symmetric and do not show any additional peaks due to oxidation or due to carburization reactions to form Si(1-x)C(x) compounds. (b) AFM image of HOPG showing a flat and clean surface with several monatomic steps (whites arrows). (c) Silicon monolayer deposited at RT on HOPG. The image has been collected in air. The Si thin film (clearest regions indicated by a light blue arrow) appears to not completely cover the entire HOPG substrate (darkest regions) probably because of the large mismatch between the silicon and graphite atomic lattices. The white spots are very small 3D Si clusters (1 nm height) which decorate the HOPG steps (white arrows). (d) Enlarged image of a region of the AFM image shown in (c), where the HOPG regions (white arrows), silicene patchworks (light blue arrows), and Si clusters (white spots) are shown.

9.2.4 AFM measurements

Atomic force microscopy (AFM) measurements were performed in air, on the same sample used for the STM measurements, with a XE-100 of PSIA apparatus with sharp silicon tips for advanced scanning probe microscopy.

The AFM image of the HOPG sample in Figure 9.12-b shows a perfectly flat and clean bare surface with well-resolved monatomic steps. Figure 9.12-d (as an enlarged view of Figure 9.12-c) shows the AFM images collected on the same substrate after 1 ML deposition of Si maintaining the substrate at RT. As reported in Figure 9.12-d, the silicene ultrathin film appears organized in

a quasi-continuous layer with large patchworks (clearest regions indicated by light blue arrows) extending over tens of nanometers, but not completely covering the HOPG substrate (darkest zones as indicated by white arrows) probably because of the large mismatch between the silicon and graphite lattices. In these conditions, we estimate that the percentage of coverage of HOPG is about 80%. Due to the exposure to air, we cannot exclude the formation of a silicon oxide layer, although a low reactivity of the silicene surface with O_2 has recently been reported.[115] Moreover, we note from the AFM image that the silicene areas form flat surfaces (with a roughness of 0.1-0.2 nm measured by the line profile of the clearest zones of Figure 9.12-d). The white spots are due to the formation of small Si clusters (1 nm high) which decorate the HOPG monatomic steps, as indicated in Figure 9.12-c by white arrows.

9.3 Conclusion

This work is devoted to the investigation of a new allotropic form of silicon, namely silicene. A new form of silicon whose lattice structure resembles that of graphene, yet includes a small buckling of the Si atoms, and whose synthesis on supporting substrates remains a challenging issue.

Our preliminary investigations on the interactions of Si atoms with a silver surface, based on AIMD simulations, have shown a non-negligible interaction between Si and Ag atoms. Our results have shown that Si atoms penetrate into the first layer of the silver surface. They can expel Ag atoms and form bonds with other Si atoms inside the first layer rather than remaining on top of the substrate.

To solve the growth problems, we have performed a combined experimental and theoretical study to investigate the growth of silicene on HOPG. In this study, we directly deposited Si on a chemically inert graphite substrate at RT. Based on AFM, STM, and AIMD simulations, we revealed the growth of silicon nanosheets where the substrate-silicon interaction is minimized. STM measurements clearly displayed the atomically resolved unit cell and the small buckling of the silicene honeycomb structure. Similar to the C atoms in graphene, each of the Si atoms has three nearest and six second nearest neighbors, thus demonstrating its dominant sp^2 configuration. Our STS investigations confirmed the metallic character of the deposited silicene, in excellent agreement with our band structure calculations that have also exhibited the presence of a Dirac cone.

Chapter 10

Van der Waals Heteroepitaxy of Germanene Islands on Graphite

The success in synthesizing silicene nanosheets on HOPG surface have spurred our interest to carry out new investigations on another group IV element, germanium. This chapter presents our results on germanene/HOPG heterostructures based on a combined theoretical and experimental study.

10.1 Theoretical results

10.1.1 Germanene/HOPG structure optimisations

Ab initio electronic structure and total energy calculations were performed using VASP-5.3.5.[29] The calculations were based on DFT and the PAW representations.[30] The exchange-correlation interaction was treated with the GGA parametrized by the PBE formula.[31] The van der Waals correction to the GGA calculations was included by using the D2 method of Grimme.[133] The wave functions were expanded in plane waves up to a kinetic energy cutoff of 400 eV. For BZ integrations, a Γ-centered k-point mesh of size 4×4×1 was used for the geometry optimizations and of size 11×11×1 for the density of states computations. The optimization of the atomic positions was performed via the conjugate-gradient method with the maximal force equal to 0.01 eV $Å^{-1}$. The convergence criterion of the total energy for SCF calculations was chosen to be 10^{-4} eV.

The graphite substrate was modelled by a four-layer slab in ABAB stacking of graphene layers with PBC in three dimensions and keeping the bottom two layers fixed at the optimized bulk values. Two neighboring slabs were separated by a vacuum space of about 15 Å along the z-direction that is perpendicular to the surface to avoid interactions between the different slabs. For establishing the calculation models for the germanene/HOPG structure and to minimize the lattice mismatch between the two lattices, different configurations have been investigated.

Several models have been created by combining different supercells of germanene and graphite with a rotation angle between the two surfaces.

Our first principles calculations show that the van der Waals interaction is responsible for the bonding of the germanene layer to the graphite substrate. Eventual covalent bonding between the Ge and C atoms is ruled out by the search for the minimum-energy structure. The weak bonding to the substrate allows for an out-of-plane buckling and in-plane misorientation of the germanene layer with respect to the graphite substrate, enabling a partial relief of the misfit strain of the system. As a consequence of the weak interaction, our simulations show multiple configurations having similar stability which could coexist at finite temperatures. The binding energy per Ge atom, defined as

$$E_b = \frac{(E_{Ge/HOPG} - N_{Ge} \times E_{Ge} - N_C \times E_C)}{n_{Ge}} \tag{10.1}$$

where $E_{Ge/HOPG}$ is the total energy in the supercell germanene/HOPG; $N_{Ge}xE_{Ge}$ and N_CxE_C are the total energies in the monolayer germanene and graphite unit cells, respectively; and n_{Ge} is the number of Ge atoms in the germanene/HOPG supercell. Equation (10.1) shows a maximum difference in E_b for the different investigated configurations to be about 40 meV. The structural parameters are then defined by averaging over the configurations with the uncertainty being the statistical dispersion.

In Figure 10.1, we display a ball-and-stick model of the germanene on graphite heterostructure. Despite sharing a honeycomb structure, the lattice constant of graphite is markedly smaller (about 38%) than that expected for germanene; consequently, the two lattices can be unequivocally distinguished by STM (see below). The difference in the relative size is evident from the schematic illustration of the germanene/HOPG system reported in Figure10.1-a. Such a lattice mismatch, which would be giant for classical epitaxial growth based on covalent bonding, is easy to handle in van der Waals heteroepitaxy because of the weakly bound heterojunction.[138, 139]

From DFT, the relaxed germanene structure has a Ge bond length of (2.45 ± 0.07) Å with a buckling of (0.69 ± 0.07) Å, and its distance to the top layer of graphite is (3.28 ± 0.04) Å.

10.1.2 Electronic band structure calculations

In Figure 10.2-a, we show the calculated electronic band structure of the germanene/HOPG heterosystem along the line paths M-K, K-Γ, and Γ-M of the BZ. An enlarged picture in the vicinity of the Fermi level is displayed in Figure 10.2-b. To facilitate the comprehension of the band structure of the heterosystem, the contributions of germanene (Ge) and graphite (C) to the bands are shown in green and red, respectively. We find that the Dirac cone of germanene supported on graphene is mapped to the Γ point. Thin dashed lines are also added as a guide to the eye to highlight the linearity of the electronic bands of germanene at the Γ point. When germanene is paired up to an inert substrate like graphite, the van der Waals interaction at the interface breaks the sublattice symmetry in germanene and opens a small band gap. We find that the band gap of germanene supported on HOPG is about 80 meV, larger than the

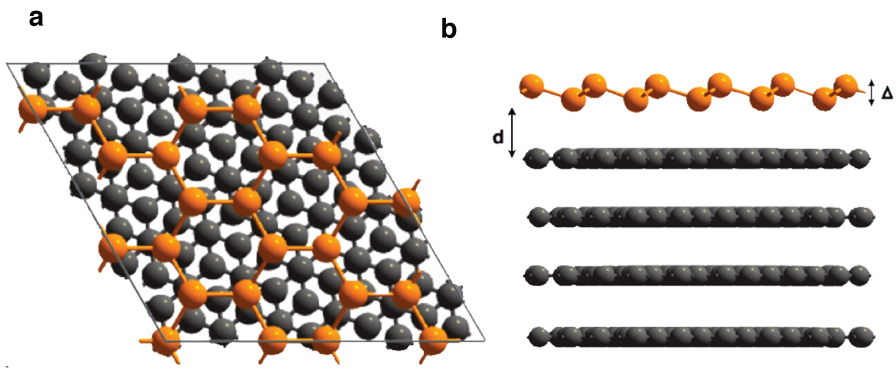

Figure 10.1: Atomic structure model of the germanene on HOPG system. Schematics showing the top (a) and side (b) views of the germanene/graphite system with a 21° rotation angle between the surfaces based on our DFT calculations. Ge atoms have a residual buckling (Δ) of 0.7 Å and a distance (d) of 3.2 Å from the graphite substrate. Orange and gray balls represent Ge and C atoms, respectively.

free-standing germanene value of 24 meV.[115] The difference is due to two distinctive origins for the gap opening in both cases. For the free-standing layer, the gap is induced only by effective spin-orbit coupling, whereas in our case, it is directly caused by the broken symmetry at the interface driven by the van der Waals interaction between germanene and graphene layers. In particular, the charge transfer at the interface builds up an interlayer potential difference, *i.e.*, the two sublattices of germanene feel different Coulomb fields, and this results in a charge redistribution leading to the opening of a gap.[140] The Fermi level crosses the Dirac cone, promoting an electron transfer between germanene and graphene layers which shifts the Dirac cone of germanene about 0.1 eV above the Fermi level. It is interesting to note that similar light doping effects have already been found for the inverse epitaxy, e.g., graphene/germanium[141] or observed for graphene coupled to silicon islands.[142] The shift is also clearly visible from the calculated total electronic DOS[1] (Figure 10.5-a) and can be used as a fingerprint of germanene compared to HOPG.

10.2 Experimental results

Experiments were performed in an UHV environment at a base pressure of $p<4\times10^{-11}$ mbar. Graphite substrates were thoroughly outgassed in UHV for several hours at 400°C. Ge was deposited at RT using an e-beam evaporator at a rate of 0.07 ML per minute. After Ge deposition, samples were annealed to 350°C for 10 min. The growth was monitored *in situ* by STM (Omicron-STM) using W tips at room temperature. Lattice parameters were obtained by analyzing the STM images with the Lattice tool of the WsXM software.

[1] See a discussion on the calculated DOS in the experimental results, Section 10.2.2.

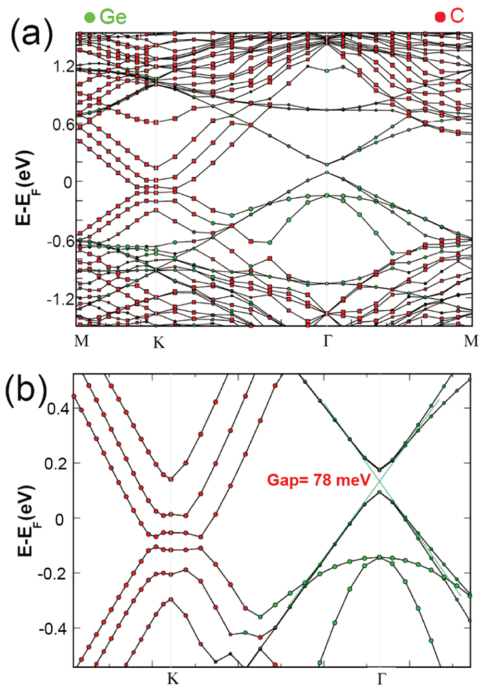

Figure 10.2: Electronic band structure of germanene/HOPG by DFT calculation. Projected bands of Ge and C are highlighted in green and red, respectively. Panel (b) shows a blow-up close to the Fermi level. The linearly dispersing bands of germanene around the Γ-point are highlighted by thin dashed lines.

10.2.1 STM measurements

10.2.1.1 Bare HOPG

Let us first characterize the surface of the graphite substrates which were used for the growth of germanene. In Figure 10.3, we show atomic resolution STM images of the bare graphite surface prior to Ge deposition. In panels a and b, we observe the well-known triangular lattice of graphite with a periodicity of about 0.25 nm, matching well the second-neighbor distance of C atoms. The triangular lattice stems from the electronic interaction of the surface graphene layer and the underlying layers: for the A-B stacking of graphite, there is a lower electronic density of states for carbon atoms that are situated directly above a carbon atom in the underlying layer because of the π-state interaction between the two carbon atoms. This suggests that the whole honeycomb lattice can be imaged if the coupling between the layers is reduced. It has actually been demonstrated that the STM tip can lift the surface layer enough to make this happen.[143] An example is reported in Figure 10.3-c which shows a honeycomb lattice with a first-neighbor distance of about 0.14 nm, as expected for a graphene layer.

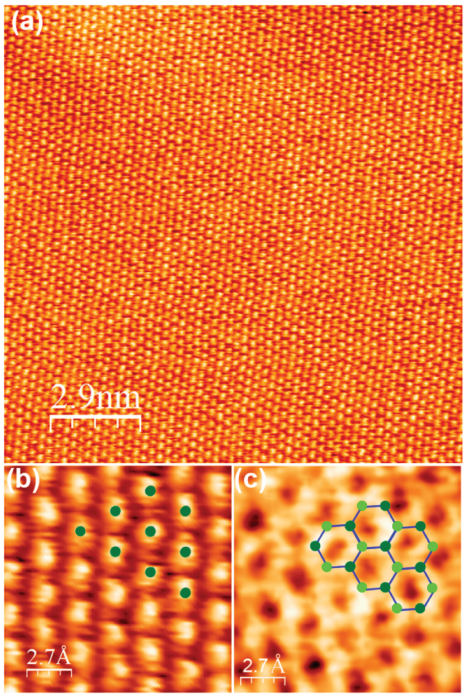

Figure 10.3: Atomic-resolution STM images of the bare graphite surface used as a template for the germanene growth. (a, b) triangular lattice; (c) honeycomb lattice (V_{bias}= -106 mV; I= 2.1 nA). On the images, ball-and-stick models showing the triangular and the honeycomb lattices are superimposed as a guide for the eye.

10.2.1.2 Germanene islands on HOPG

A typical nanometer-sized island grown on top of graphite after the deposition of a nominal coverage of 0.2 ML of Ge at room temperature and subsequent annealing to 350°C is shown in Figure 10.4-a. The height profile across the edge of the sheet (inset of Figure 10.4-a) indicates that the distance of the overlayer from the substrate is (3.0± 0.2) Å, a value compatible with the expected separation of a germanene layer grown on graphite and in excellent agreement with our DFT calculations. On the islands, high-resolution imaging of the germanene honeycomb lattice is obtained (Figure 10.4-b) and both triangular sublattices of the honeycomb are resolved. This is noteworthy because in the other reports on the growth of silicene and germanene on insulating substrates the honeycomb lattice was often imaged only in part.[131, 144] The periodicity of the structure shows a first neighbor separation (bond length) of (2.5± 0.2) Å and a second-nearest distance of (4.2±0.3) Å. These values closely match those expected for a germanene layer. Also, the lattice does not lie perfectly flat on the substrate but shows a residual buckling of about 0.7 Å. In contrast to metal-supported germanene, we do not observe any atomic reconstruction, suggesting that the properties of free-suspended germanene are preserved on graphite. The absence of atomic reconstruction is confirmed by the simulated STM image of germanene on graphite shown in Figure 10.4-c.

In addition to the 2D germanene island, a small 3D Ge cluster is visible in Figure 10.4-a. This

confirms the existence of a competition between perfect 2D growth driven by van der Waals interaction and the onset of 3D growth.

As a larger amount of Ge is deposited (0.7 ML), Figure 10.4-d, the germanene patches follow the underlying graphite layers as does a carpet, confirming that the formation of the 2D sheets is driven by Ge. The density and size of germanene islands increase, although uncovered substrate areas are still visible between the islands.

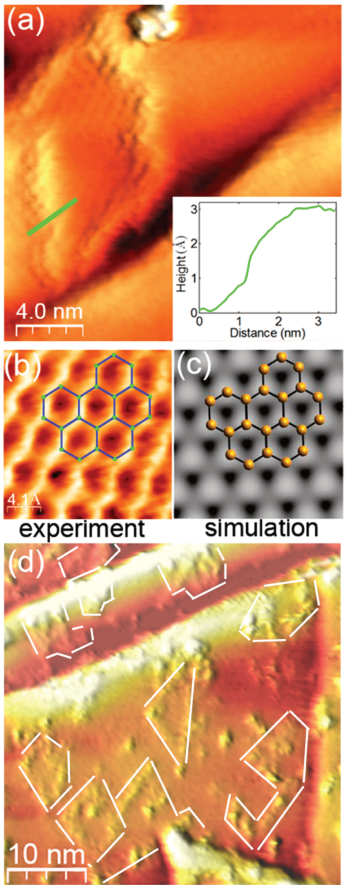

Figure 10.4: STM images showing 2D islands formed after Ge deposition at room temperature and subsequent annealing to 350°C. Panel (b) shows an enlarged view of the honeycomb lattice of the 2D islands. The nominal Ge coverage is 0.2 ML in panels (a) and (b) and 0.7 ML in panel (d). In the inset of panel (a), the height profile taken along the green line in the image is shown. A 3D Ge cluster is also visible in the top part of the image in panel (a). (c) Simulated STM image of germanene/graphite having the same size as in panel (b) and recorded with the same scanning parameters, based on calculated partial charge densities, but at 0 K. The Ge atoms in the honeycomb arrangement are highlighted by a ball-and-stick model. In panel (d), the edges of the islands are highlighted. The STM scan parameters are V_{bias} = -980 mV and I = 1.0 nA for panels (a) and (d) and V_{bias}= -860 mV and I= 0.88 nA for panel (b).

10.2.2 STS measurements

In order to better understand the electronic properties of the deposited germanene layer, we have measured the STS spectra at different areas on the surface at RT with the Z-feedback off. First, let us compare the STS spectra taken on top of a germanene island, Figure 10.5-b, with that on the bare HOPG substrate, Figure 10.5-c. As expected, both curves reveal a metallic character with a finite DOS close to the Fermi level. However, while the STS curve for HOPG has a minimum at the Fermi level, the germanene curve is shifted toward the empty states, well-matching the results of our DOS calculations (see Figure 10.5-a). Actually, it has recently been shown that the metallic behavior of the "silicene" I/V curve has been exploited for realizing a field effect transistor based on ambipolar charge transport effects.[145] Besides topography, this electronic fingerprint clearly distinguishes germanene from the graphite substrate. Conversely, STS curves taken on 3D clusters (inset of Figure 10.5-c) show the absence of electronic states at the Fermi level, confirming that 3D Ge nanoislands are semiconducting.[146]

10.3 Conclusion

Flat 2D germanium sheets, showing a honeycomb lattice, grown on top of a HOPG surface were the result of a successful collaboration between theory and experiments. Germanene islands were synthesized on HOPG by depositing submonolayers of Ge on graphite at RT and subsequent annealing to 350°C. STM showed that the germanene islands have a small buckling with no atomic reconstruction and did not give any hints for alloy formation and hybridization with the substrate. Our DFT calculations of the structural properties agreed well with our experimental findings and indicated that the germanene sheet interacts only weakly with the substrate underneath. Our band structure calculations confirm that the Dirac cone of free-standing germanene is preserved for layers supported on graphite. The germanene islands show a small, but characteristic charge transfer with the graphite substrate which is predicted by our *ab initio* simulations in excellent quantitative agreement with our STS measurements.

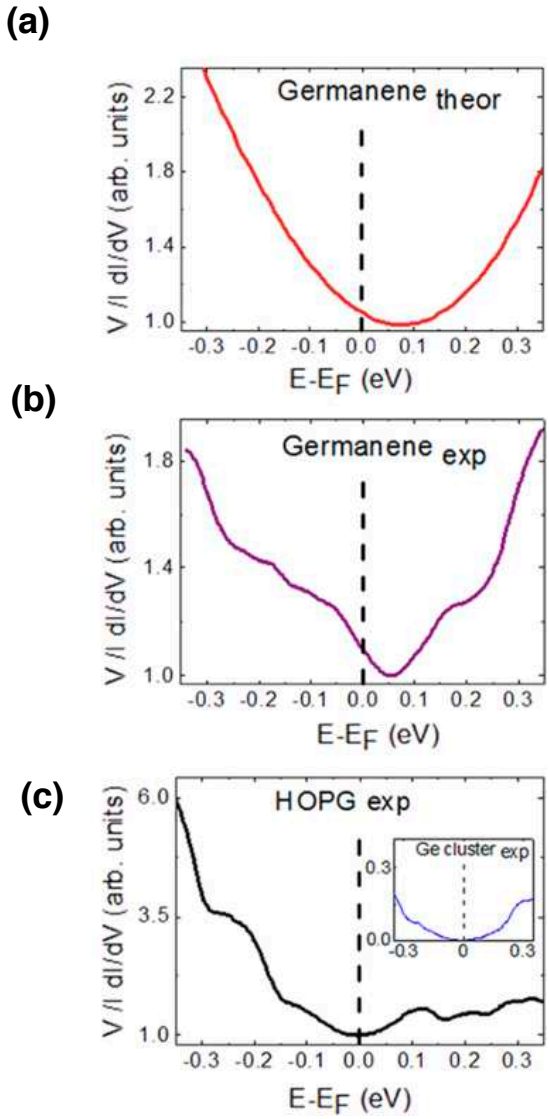

Figure 10.5: Scanning tunneling spectroscopy measurements and density of states calculations. (a) Calculated total DOS for germanene on graphite. (b, c) Normalized differential tunneling conductance (V/I)dI/dV obtained by STS at room temperature: (b) on top of a germanene island; (c) on the HOPG substrate (main panel), on a Ge 3D cluster (inset). In contrast to clusters, germanene shows a finite DOS at the Fermi level. The axis labels of the inset are the same as for the main panel. Each experimental curve is an average of 10 acquisitions.

Chapter 11

Conclusions and Perspectives

Our economy consistently pushes for the development of revolutionary materials to meet our ever-increasing technological demands. The search for novel silicon allotropes and corresponding synthesis methods represents the beginning of a wide-open field which is expected to yield further exotic structures with superlative properties. In this context, we focused our studies on new allotropes of silicon and explored their miscellaneous and fascinating properties. Not only silicon, but also its brother, germanium, is part of our research interests.
Two topics were the subject of this thesis:

1. Plasma-born aromatic silicon nanoclusters.
2. Two-dimensional silicon and germanium materials.

In the first topic, we focused our theoretical study mainly on the isomer scaffold of hydrogenated silicon clusters with a $Si_{19}H_{12}$ stoichiometry, as one specific example, in order to demonstrate that a cluster of a given stoichiometry can possess a huge variety of physical and chemical properties resulting from apparently minor differences in its structure. Looking at different previously reported stoichiometries, we notice how the properties can further dramatically be changed by modifying the cluster size by just a few Si atoms and/or by the different degrees of hydrogenation of those clusters. This result can fully be exploited for the fabrication of cheaper and less toxic nanotechnological components and devices since it is a powerful alternative to the more traditional strategy where different properties are obtained by changing the chemical composition often involving the incorporation of chemicals as toxic as PbS, PbSe, CdS, and CdSe or as expensive as Ag and Au.
$Si_{19}H_{12}$ nanoclusters exhibit high electron delocalization as can be concluded from their magnetic shielding values and their magnetically induced aromatic ring currents that largely exceed the ones of benzene. The ELF calculations demonstrate that the electrons around the over-coordinated Si atoms behave similar to the ones in a homogeneous electron gas showing some clear resemblance with small metal clusters, resulting in an extended range of absorption wavelengths from the ultraviolet to the infrared. Using NEB calculations of the $Si_{19}H_{12}$ scaffold, we established how many isomers may be yet more stable than the symmetric nanocrystal, but that

all members of this scaffold manifest very comparable physical, optical, and chemical properties despite their asymmetric structures. This last finding has demonstrated the potential wealth of non-tetrahedral hydrogenated silicon nanoclusters that all derive their ultrastability and their special features from extensive electron delocalization that is induced by their electron deficient bonds. All isomers of the presently investigated scaffold turned out actually to be so much more stable than their tetrahedral counterparts that it appeared quite unlikely that the latter ones are formed at all by self-assembly. This conclusion is supported by the fact that we have never observed the spontaneous formation of tetrahedral clusters in the presently investigated cluster size range during the AIMD simulation of the cluster growth.

For a given stoichiometry, the degree of electron delocalization depends on the details of the cluster structure. Since delocalized electrons are less tightly bonded, the resulting calculated absorption spectra shift toward longer wavelengths in comparison with perfectly tetrahedral silicon clusters of the same size. In order to prove this, we performed several experiments to investigate the absorption spectra of plasma-born hydrogenated silicon clusters with a size of less than 2 nm in the visible spectral region. To this end, we combined a cavity enhanced absorption setup as a diagnostic tool with a capacitively-coupled plasma reactor. We optimized the plasma parameters, such as the gas temperature and pressure, the plasma duration, pulse cycle, etc, in such a way that we only create "first-generation" nanoclusters that, based on our AIMD simulations, would spontaneously form with a variety of non-tetrahedral structures. We synchronized the incoherent broadband cavity enhanced absorption measurements with the nanoclusters production and we measured the transmitted light intensities "simultaneously" with and without the absorbing species between two successive plasma pulses. Using a spatially coherent supercontinuum light source, a bunch of filters, and two sets of highly reflecting mirrors, covering two spectral ranges between 575-665 nm and between 655-745nm, respectively, we found an obvious extinction peak around 645 nm. The size of this peak have also shown to vary with the density of absorbing nanoclusters crossing the detection beam by varying the time between the end of the discharge and the measurement of the cavity transmission.

Besides, we performed numerous extinction measurements varying the discharge time (from a few milliseconds to a few seconds), the reactor pressure and temperature, and the gas flow rate. The results will be analysed, in a future study, for an understanding of the nucleation and growth of silicon nanoclusters in a plasma reactor.

Moreover, we performed extensive extinction measurements with- and without an electric field applied during the cavity transmission measurements. Here, we have always obtained a decrease in the extinction peak in the presence of an applied DC bias which depends on the strength of the electric field. This effect can only be attributed to the presence of a permanent dipole moment in plasma-born silicon nanoclusters, where the inhomogeneity of the electric field in the reactor chamber plays an important role. Simulations of the electric field have helped us to analyse and understand the behavior of aromatic silicon nanoclusters under the influence of the dipole forces. From the coherence between our simulations of the density or distribution of nanoclusters in the plane of the detection beam and the extinction measurements, we found the permanent dipole moment of aromatic silicon nanoclusters to be between 2.0 and 2.5 Debye in excellent agreement with our prior *ab initio* calculations. Such a property is crucial for many applications that rely on the use of polar molecules to enhance the properties of materials, as for instance the modification of the work function of electrodes of an organic field effect transistor.

Furthermore, the deposition of such silicon nanoclusters under optimized plasma conditions have shown the formation of crystalline nanoparticles along with amorphous ones. From our HRTEM characterization, we found that the crystalline nanoparticles, with a size of 2.0 to 3.5 nm, attain a primitive hexagonal structure. Such a crystalline structure of silicon obtained from a RF plasma along with other structures reported in the literature, such as the bc8 and the bcc, usually form after exposing diamond silicon to extremely high pressures. Since the appearance of exotic forms of silicon by a RF plasma is not well understood yet, we propose an experiment to examine where such a crystallization takes place. For instance, we can deposit the nanoclusters (under different optimized plasma conditions) on a soft surface (gel), instead of a hard one, placed under a grid to control the impact velocity. Then, we can collect the nanoclusters and perform HRTEM measurements. From the obtained results, we can deduce if the crystallization occurs in the plasma or if a high impact energy is needed. If the latter is true, we will have direct experimental evidence for the theoretically predicted "chemistry with a hammer" mechanism.
Finally, a plasma-born mixture of different structures deposited within a thin film might be advantageous; e.g. for efficient large-band light absorption as needed, for instance, in photovoltaic cells and protective coatings. Indeed, combining slightly different stoichiometries and structures, light of the entire solar spectrum between 1.0 eV and 5.2 eV can be absorbed using only nanoclusters having a size of about twenty silicon atoms. Therefore, this new allotropic form of nanosilicon may pave the way for new competitive solar materials and architectures. We predict that this unique combination of metal and semiconductor properties within the same pure, but nontetrahedral hydrogenated silicon nanoclusters will be an extremely rich source for future bandgap engineering employing nothing else but silicon and hydrogen atoms.

In the second topic, we focused on a combined theoretical and experimental study of the growth of a new allotropic form of silicon and germanium, silicene and germanene, on top of a graphite surface. We have obtained, and for the first time, several silicene areas with a structure very similar to that of graphene by the deposition of one ML of Si on an inert HOPG substrate at RT and under UHV conditions. The AFM images supported the formation of a quasi-continuous 2D silicon layer leaving some areas of HOPG uncovered together with the formation of small 3D Si clusters. The STM data supported the existence of a graphene-like structure with a very small buckling of the silicon nearest neighbors. The atomic resolution images obtained by STM did not show any surface reconstruction, as found when silicene is deposited on metal surfaces, suggesting a negligible electronic interaction/hybridization with the substrate underneath. Our observation suggested that a growth mode with a full release of strain has occured. Our AIMD simulations predicted the thermal stability of a perfect silicene monolayer on a HOPG surface at RT and 350°C, highlighting the essential role of van der Waals forces bonding silicene to the surface. The simulations of the growth mechanism of the silicene sheet on HOPG at RT showed how the silicon hexagons spontaneously form and remain at a vertical distance corresponding to the van der Waals distance above the surface.
Similarly, flat 2D sheets showing a honeycomb lattice matching that of germanene were synthesized for the first time by depositing submonolayers of Ge on HOPG at RT followed by annealing to 350°C. The overlayers also showed a small buckling and no atomic reconstruction suggesting the absence of any alloy formation and hybridization with the substrate. *Ab initio* calculations indicated that the Dirac cone of free-standing germanene is preserved for layers deposited on

HOPG. Compared to the substrate, the germanene islands showed a characteristic charge transfer which was predicted by simulations and observed with STS spectroscopy. The two different approaches lead to an astonishing quantitative agreement.

HOPG has been found to be a good candidate to form silicene and germanene layers with remarkable electronic properties very different from any other known silicon and germanium-based nanostructures. The growth of silicene and germanene on a nonmetallic and inert substrate is an important step toward the realization of alloy-free layers with properties that approach the free-standing ones. We believe that we have succeeded in observing these small, but true, silicene and germanene areas because of a rather slow deposition rate of Si and Ge, and we are confident that in the future by using more sophisticated growth methods (as molecular beam epitaxy) larger areas can be obtained. Only in the case of a continuous silicene and germanene layer formation, we will be able to detach and transfer these ultrathin films for device applications.

In future works, the ideal deposition temperature has, for instance, to be determined more carefully: hot enough to overcome all energy barriers to silicene and germanene growth, but low enough to avoid 3D cluster formation. Optimized experimental deposition conditions will favor the extent of the pure silicene and germanene domains, eventually pushing them to the size limits imposed by the terrace size of the graphite substrate possibly making the use of graphene instead of graphite necessary for extremely large 2D layers.

The ultimate silicene/graphene heterostructure can then be lifted off from the underlying substrate and be deposited on SiO2 as already reported in the literature. The silicene/graphene/-SiO2 system can then be integrated in functional devices. Such systems can be grown on a very large scale corresponding to the requirements of the electronic industry. Besides this immediate compatibility with powerful silicon technologies and the absence of any alloying problems, the silicene on graphite system presents a much less expensive solution than strategies based on silver substrates. The present research is in the forefront of 2D materials with revolutionary future applications for nanotechnological devices as, for example, ultra-high-speed electronic devices and for functional electronic devices based on silicene and germanene.

Appendix A

Molecular Dynamics Simulations

A.1 The basic idea

With the advent of high speed and massively parallel computing, simulations play a very important role in science today to the extent that their results can be compared directly with experimental results. Computer simulations have become an extremely powerful tool not only to understand and interpret experimental results at the microscopic level, but also to predict and study cases which are not accessible experimentally or which imply very expensive experiments.

One of the most commonly used theoretical approach is the molecular dynamics (MD) method, in which the time evolution of a set of interacting particles is followed by integrating their equations of motion. The particles interact by exerting forces on each other and they follow the laws of classical mechanics, notably Newton's second law of motion:

$$\mathbf{F}_i = m_i \mathbf{a}_i = m_i \frac{d^2 \mathbf{r}_i}{dt^2} \tag{A.1}$$

where, $\mathbf{F}_i$ is the force acting upon the ith particle at time t; m_i, $\mathbf{a}_i$, and $\mathbf{r}_i$ are the mass, acceleration, and position of particle i, respectively.

With the interatomic potential, $U(\mathbf{r}_1,\mathbf{r}_2,...,\mathbf{r}_N)$, which represents the potential energy of N interacting particles in a system as a function of their positions $\mathbf{r}_i$, being known, the force acting upon each particle can be determined by the negative gradient with respect to the particle displacement as:

$$\mathbf{F}_i = -\frac{\partial U(\mathbf{r}_1, \mathbf{r}_2, ..., \mathbf{r}_N)}{\partial \mathbf{r}_i} \tag{A.2}$$

The solution of the set of equations (A.1) gives the positions and velocities of each particle in the system at any time; *i.e.*, the phase-space trajectories of the system.

Therefore, in order to calculate a MD trajectory of a system we need, in general, to perform the following:

- Specify the initial positions and velocities of all particles of the system of interest.

- Compute the forces acting on all particles according to Eq. (A.2). This is the most time-consuming calculation.
- Integrate the above second order differential equations, Eq. (A.1). Due to the many-body nature of the problem, the equations of motion are discretized and solved numerically.
- As the particles "move", their trajectories are analysed, providing instantaneous and averaged properties.

The second and third steps are repeated for a chosen number of time-steps (Δt) in a MD simulation.

A.1.1 Numerical integration of the equations of motion

The aim of the numerical integration of Newton's equations of motion is to find positions $\mathbf{r}_i(t+\Delta t)$ and velocities $\mathbf{v}_i(t+\Delta t)$ at time $t+\Delta t$ in terms of the already known positions and velocities at time t. To this end, the Verlet algorithm is used in our MD simulations because of its simplicity and its stability. The basic formula for this algorithm is derived from the second-order Taylor expansions for the positions of a particle at $(t+\Delta t)$:

$$\mathbf{r}_i(t+\Delta t) = \mathbf{r}_i(t) + \mathbf{v}_i(t)\Delta t + \frac{1}{2}\frac{\mathbf{F}_i(t)}{m_i}(\Delta t)^2 + O((\Delta t)^3) \tag{A.3}$$

similarly,

$$\mathbf{r}_i(t-\Delta t) = \mathbf{r}_i(t) - \mathbf{v}_i(t)\Delta t + \frac{1}{2}\frac{\mathbf{F}_i(t)}{m_i}(\Delta t)^2 - O((\Delta t)^3) \tag{A.4}$$

By adding Eqs. (A.3) and (A.4), we obtain:

$$\mathbf{r}_i(t+\Delta t) = 2\mathbf{r}_i(t) - \mathbf{r}_i(t-\Delta t) + \frac{\mathbf{F}_i(t)}{m_i}(\Delta t)^2 + O((\Delta t)^4) \tag{A.5}$$

Equation (A.5) is accurate up to terms of the fourth power in Δt. The velocity is computed by subtracting Eq. (A.4) from Eq. (A.3):

$$\mathbf{v}_i(t) = \frac{\mathbf{r}_i(t+\Delta t) - \mathbf{r}_i(t-\Delta t)}{2\Delta t} + O((\Delta t)^2) \tag{A.6}$$

The choice of Δt is an important consideration in any MD simulation. Exact trajectories correspond to the limit of an infinitesimally small integration step in order to conserve the total energy of the system. For a too large Δt, a particle can find itself *unphysically* close to another particle. This will be reflected in a "jump" in the potential energy and the total energy of the system. Moreover, the period of the bond vibration must also be considered. For instance, bonds involving light atoms vibrate with periods of several femtoseconds, implying that Δt should be on a subfemtosecond scale to ensure stability of the integration and to follow adequately the movement of all atoms.

A.2 Classical *vs ab initio* molecular dynamics simulations

The quality of a MD calculation depends largely on the method by which the forces are calculated. In classical MD simulations, the forces are computed from "force field" models or empirical potentials with a specific functional form representing the physics and chemistry of the system of interest. The adjustable parameters are chosen such that the empirical potential represents a good fit to the results of *ab initio* calculations of small model systems, or they may be based on experimental data. Since most force fields are not able to model chemical reactions because of the requirement of breaking and forming bonds, it is often necessary to turn to the methodology of *ab initio* molecular dynamics (AIMD). In an AIMD calculation, finite-temperature dynamical trajectories are generated by using forces obtained directly from electronic structure calculations performed "on the fly" as the simulation proceeds. Thus, AIMD permits chemical bond breaking and forming events to occur.[147]

Appendix B

Density Functional Theory

B.1 The Schrödinger equation

If we are interested in describing the electron distribution in detail, there is no substitute for quantum mechanics. Electrons are, to a certain extent, delocalized and "shared" by many nuclei and the resulting electronic cloud determines the chemical bonding. The Schrödinger equation is the fundamental equation of quantum mechanics. In principle, the solution for a system of N nuclei and n electrons can be found in the time-independent non-relativistic Schrödinger equation,

$$\hat{H}\Psi(\mathbf{R},\mathbf{r}) = E\Psi(\mathbf{R},\mathbf{r}) \tag{B.1}$$

where $\mathbf{R}$ and $\mathbf{r}$ are collective variables of the nuclear and electronic coordinates, respectively. E is the total energy of the system and Ψ is the wavefunction of the $3n$ electronic coordinates and $3N$ nuclear coordinates. The many-body Hamiltonian operator, $\hat{H}$, is represented as:

$$\hat{H}(\mathbf{R},\mathbf{r}) = \hat{T}_N(\mathbf{R}) + \hat{T}_e(\mathbf{r}) + \hat{V}_{NN}(\mathbf{R}) + \hat{V}_{ee}(\mathbf{r}) + \hat{V}_{Ne}(\mathbf{R},\mathbf{r}) \tag{B.2}$$

where the first two terms represent the nuclear and electronic kinetic energy operators, respectively. The third and fourth terms represent the nuclear-nuclear and electron-electron Coulomb repulsion, respectively, and the last term represents the nuclear-electron Coulomb attraction. The above terms are expressed in atomic units as follows:

$$\hat{T}_N = -\sum_{I}^{N}(\frac{1}{2M_I})\nabla_I^2 \tag{B.3}$$

$$\hat{T}_e = -\frac{1}{2}\sum_{i}^{n}\nabla_i^2 \tag{B.4}$$

where ∇_I^2 and ∇_i^2 are the Laplacian operators involving the differentiation with respect to the I-*th* nucleus coordinate and the i-*th* electron coordinate at the $\mathbf{R}_I$ and $\mathbf{r}_i$ positions, respectively.

Moreover,

$$\hat{V}_{NN} = \frac{1}{2}\sum_{I=1}^{N-1}\sum_{J=I+1}^{N}\frac{Z_I Z_J}{|\mathbf{R}_I - \mathbf{R}_J|} \tag{B.5}$$

$$\hat{V}_{ee} = \frac{1}{2}\sum_{i=1}^{n-1}\sum_{j=i+1}^{n}\frac{1}{|\mathbf{r}_i - \mathbf{r}_j|} \tag{B.6}$$

$$\hat{V}_{Ne} = -\sum_{I=1}^{N}\sum_{i=1}^{n}\frac{Z_I}{|\mathbf{R}_I - \mathbf{r}_i|} \tag{B.7}$$

here Z_I and Z_J are the atomic numbers of nuclei I and J.

Due to the complexity of the many-body problem, Eq. (B.1) becomes difficult to be solved and an approximation is needed.

B.1.1 Born-Oppenheimer approximation

In 1927, Born and Oppenheimer[148] showed that to a very good approximation, based on the huge difference in mass between nuclei and electrons, the electronic and nuclear problems can be separated. Hence, it is assumed that the electron cloud "equilibrates" quickly for each instantaneous configuration of the heavy nuclei. In other words, the electronic wave functions can be found by assuming that the nuclei are fixed. The nuclei, in turn, move in the field of the averaged electron densities. Consequently, the electronic and nuclear motions are said to be decoupled. Therefore, the total wave function of a given electronic state splits into two components: one which describes the nuclear motion, $\chi(\mathbf{R})$, and one which describes the electronic motion, $\psi(\mathbf{R},\mathbf{r})$, for a fixed nuclear coordinate, $\mathbf{R}$. Therefore, the total wave function has the form:

$$\Psi(\mathbf{R},\mathbf{r}) = \chi(\mathbf{R})\psi(\mathbf{R},\mathbf{r}) \tag{B.8}$$

Then, the electronic wave function $\psi(\mathbf{R},\mathbf{r})$ is obtained from the solution of the electronic Schrödinger equation:

$$\left(-\frac{1}{2}\sum_{i=1}^{n}\nabla_i^2 + \hat{V}_{ee}(\mathbf{r}) + \hat{V}_{Ne}(\mathbf{R},\mathbf{r})\right)\psi(\mathbf{R},\mathbf{r}) = E_e(\mathbf{R})\psi(\mathbf{R},\mathbf{r}) \tag{B.9}$$

Equation (B.9) is solved for each set of fixed nuclear positions, $\mathbf{R}$. Consequently, the electronic eigenvalue, E_e, explicitly depends on $\mathbf{R}$. The nuclei, in turn, are assumed to move according the to nuclear Schrödinger equation:

$$\left(-\sum_{I}^{N}\left(\frac{1}{2M_I}\right)\nabla_I^2 + \hat{V}_{NN}(\mathbf{R}) + E_e(\mathbf{R})\right)\chi(\mathbf{R}) = E_n(\mathbf{R}) \tag{B.10}$$

With the Born-Oppenheimer (BO) approximation, the many-body problem is reduced to the solution of the nuclear motion on a single potential energy surface (PES), where the electronic potential energy, E_e, plays part in the potential energy of the nuclei:

$$V(\mathbf{R}) = \frac{1}{2}\sum_{I=1}^{N-1}\sum_{J=I+1}^{N}\frac{Z_I Z_J}{|\mathbf{R}_I - \mathbf{R}_J|} + E_e(\mathbf{R}) \tag{B.11}$$

Therefore, within the BO approximation, the electronic eigenvalue equation, Eq. (B.9) has to be solved first. Then, Eq. (B.11) is applied to obtain the PES of the system. However, the ground-state electronic problem, Eq. (B.9), cannot be solved exactly. Therefore, approximate electronic structure methods are needed.

B.2 Kohn-Sham density functional theory

In modern AIMD, the electronic structure method most commonly used is the Kohn-Sham formulation of density functional theory (DFT). The basis for DFT is the proof by Hohenberg and Kohn[149] that the ground state electronic energy is determined completely by the electron density, ρ. The electron density is the square of the wave function, integrated over the electron coordinates. While the complexity of a wave function increases exponentially with the number of electrons, the electron density has the same number of variables, independent of the system size.[37] The goal of DFT methods is to design functionals[1] connecting the electron density with the energy.

Early attempts at designing DFT models tried to express all the energy components as a functional of the electron density, but these methods had poor performance. The success of modern DFT methods is based on the suggestion by Kohn and Sham[150] that the electron kinetic energy should be calculated from an auxiliary set of one-electron orbitals, "Kohn-Sham orbitals", used for representing the electron density. The Kohn-Sham method is based on paramaterization of the density $\rho(\boldsymbol{r})$ in terms of Kohn-Sham orbitals $\phi_i(\boldsymbol{r})$:

$$\rho(\mathbf{r}) = \sum_{i=1}^{N}|\phi_i(\mathbf{r})|^2 \tag{B.12}$$

and a decomposition of the total energy functional according to:

$$E[\rho] = T[\rho] + E_H[\rho] + E_{xc}[\rho] + E_{ext}[\rho] \tag{B.13}$$

where

$$T[\rho] = \sum_i \int \phi_i^*(\mathbf{r})(-\frac{1}{2}\nabla^2)\phi_i(\mathbf{r})d^3\mathbf{r} \tag{B.14}$$

[1] A function is a prescription for producing a number from a set of *variables* (coordinates). A *functional* is a prescription for producing a number from a function, which in turn depends on variables. The wave function and the electron density are thus functions, while the energy depending on a wave function or an an electron density is a functional.

is the contribution of the kinetic energy approximated by that of non-interacting electrons in states $\phi_i(\boldsymbol{r})$.

$$E_H = \int\int \frac{\rho(\mathbf{r})\rho(\mathbf{r}')}{|\mathbf{r}-\mathbf{r}'|} d\mathbf{r}d\mathbf{r}' \tag{B.15}$$

is the Coulomb electron-electron repulsion in the Hartree approximation, while

$$E_{ext} = \int V_{ext}(\mathbf{r})\rho(\mathbf{r}) \tag{B.16}$$

describes the interaction with the external field, with

$$V_{ext} = -\sum_I \frac{Z_I}{|\mathbf{R}_I - \mathbf{r}|} \tag{B.17}$$

the Coulomb interaction between electrons and nuclei.

$\mathrm{E}_{xc}[\rho]$ is the **exchange-correlation** energy. It accounts for "exchange" and "correlation" effects. The key to Kohn-Sham theory is to calculate the kinetic energy under the assumption of *non-interacting* electrons from Eq. (B.14). However, the electrons, in reality, *are* interacting, and Eq. (B.14) does not provide the total kinetic energy. Therefore, the remaining kinetic energy is absorbed into the $\mathrm{E}_{xc}[\rho]$ term. This complicated functional has no explicit form. It has to be approximated, as will be discussed shortly.

Variation of the total energy functional, Eq. (B.13), with respect to ${\phi_i}^*(\mathbf{r})$ leads to an effective one-electron equation for the determination of $\phi_i(\mathbf{r})$, the Kohn-Sham equations:

$$\left(-\frac{1}{2}\nabla^2 + \int \frac{\rho(\mathbf{r}')}{|\mathbf{r}-\mathbf{r}'|} d^3\mathbf{r}' + V_{ext}(\mathbf{r}) + \frac{\delta E_{xc}[\rho(\mathbf{r})]}{\delta\rho(\mathbf{r})}\right)\phi_i(\mathbf{r}) = \epsilon_i\phi_i(\mathbf{r}) \tag{B.18}$$

The Kohn-Sham equations describe electrons moving in one-electron potential given by

$$V_{eff}(\mathbf{r}) = V_{ext}(\mathbf{r}) + \int \frac{\rho(\mathbf{r}')}{|\mathbf{r}-\mathbf{r}'|} d^3\mathbf{r}' + V_{xc}[\rho(\mathbf{r})] \tag{B.19}$$

where the exchange correlation potential is given by the variational derivation of the exchange-correlation energy,

$$V_{xc}(\mathbf{r}) = \frac{\delta E_{xc}[\rho(\mathbf{r})]}{\delta\rho(\mathbf{r})} \tag{B.20}$$

The Kohn-Sham formalism solves the Schrödinger equation iteratively in a self-consistent field (SCF) fashion. SCF is needed because the Coulomb potential and the exchange-correlation potential, Eq. (B.20), are functionals of the density which itself depends on the unknown orbitals.

B.2.1 Exchange-correlation functionals

- **Local density approximation**

The difference between various DFT methods is the choice of the functional form for the exchange-correletion energy, $E_{xc}[\rho]$. Several approximation methods to the $E_{xc}[\rho]$ are available. The oldest and simplest functional is the local density approximation (LDA) proposed by Hohenberg and Kohn.[149] The LDA consists of locally approximating the true exchange-correlation energy of a system by the exchange-correlation energy associated with a homogeneous electron gas of the same density. The homogeneous gas is the only system for which the form of the exchange-correlation energy is known precisely.

The LDA is only dependent on local density, and the total energy is commonly written as

$$E_{xc}^{LDA}[\rho(\mathbf{r})] = \int d^3(\mathbf{r})\rho(\mathbf{r})\epsilon_{xc}[\rho(\mathbf{r})] \tag{B.21}$$

where $\epsilon_{xc}[\rho(\mathbf{r})]$ is the exchange-correlation energy density corresponding to a homogeneous electron gas of density $\rho(\mathbf{r})$.

- **Generalized gradient approximation**

A major drawback in LDA is its incapability of describing non-homogeneous electron densities. One way to improve this approximation is to consider, not only the electron density, but also its gradient. The electron density gradient describes the non-homogeneity of the true electron density. As a result of this procedure, the generalized gradient approximation (GGA) can be conveniently written in terms of an analytic function known as the enhancement factor, $F_{xc}[\rho(\mathbf{r}),\nabla\rho(\mathbf{r})]$, that directly modifies the LDA energy density,

$$E_{xc}^{GGA}[\rho(\mathbf{r})] = \int d^3(\mathbf{r})\rho(\mathbf{r})\epsilon_{xc}^{hom}(\rho(\mathbf{r}))F_{xc}[\rho(\mathbf{r}),\nabla\rho(\mathbf{r})] \tag{B.22}$$

In recent years, several exchange-correlation GGA implementations have become a kind of standard choice, namely: Perdew-Wang **(PW86)**,[151] Perdew-Wang **(PW91)**,[152] and Perdew-Burke-Ernzerhof **(PBE)**.[31] Moreover, several GGA functionals were developed in the form of an exchange functional (**B**)[153] or a correlation functional ((**LYP**),[154] (**B95**), and (**P86**)[155]). A combination between different exchange and correlation functionals is made to describe completely the systems under study. Some of the most common combinations are: **BP86 and BPW91**.

- **Hybrid Functionals**

Hybrid functionals were developed to provide a better description to the exchange part of the GGA functional. Since the exchange part in Hartree-Fock (HF) is defined exactly, the hybrid functional uses a combination of HF, GGA, and LDA functionals to describe the exact exchange and correlation part. One of the most commonly used hybrid functional is **B3LYP** (Becke, three-parameter, Lee-Yang-Parr),

$$E_{xc}^{B3LYP} = E_x^{LDA} + a_0(E_x^{HF} - E_x^{LDA}) + a_x(E_x^{GGA} - E_x^{LDA}) + E_c^{LDA} + a_c(E_c^{GGA} - E_c^{LDA}) \tag{B.23}$$

where a_0, a_x, and a_c are three fitting parameters; ${E_x}^{GGA}$, ${E_c}^{GGA}$, and ${E_c}^{LDA}$ are the B88 exchange functional,[153] LYP correlation functional,[154] and Vosko-Wilk-Nusair (VWN) LDA[156] correlation functional, respectively.

B.2.2 Basis sets

To solve the Kohn-Sham equations, Eq. (B.18), the single particle wave function can be mathematically expressed as a linear combination of a set of given functions. This set of functions is called a *basis set* and is formed in different ways depending on the systems under study and the required accuracy. *Localized basis sets* are one type and are based on atom-centred basis functions, while *plane wave basis sets* are another type and are used for calculations involving periodic systems.

B.2.2.1 Localized basis sets

Localized basis sets can be further classified into two main types, *Slater type orbitals* (STO)[157] and *Gaussian type orbitals*(GTO).[158] They both have the same form

$$\chi_{nlm}(r,\theta,\phi) = R_{nl}(r)Y_{lm}(\theta,\phi) \tag{B.24}$$

where n, l, and m are the principle quantum numbers and $Y_{l,m}(\theta,\phi)$ is a spherical harmonic function. The main difference in both types lies in the radial part, $R_{nl}(r)$,

$$STO : R_{nl}(r) = N_{nl}(\zeta)r^{n-1}e^{-\zeta r} \tag{B.25}$$

$$GTO : R_{nl}(r) = N_{nl}(\alpha)r^{n-1}e^{-\alpha r^2} \tag{B.26}$$

where N_{nl} is a normalization constant; ζ, in Eq. (B.25), is a constant related to the nucleus effective charge; and α, in Eq. (B.26), is the orbital exponent. Although the STO gives a more accurate description of the atomic orbital, the GTO can be numerically solved more efficiently. However, a linear combination of several GTOs, called *contractions*, is able to mimic the STO accuracy. The more of GTOs included in the contraction, the better they are able to model the accuracy of STO functions. As a result, the Gaussian type basis functions are the most popular localized basis sets used today.

When using GTOs to mimic STOs, the new basis sets are given a new name. They may be in the format of a minimal basis sets or a split-valence basis sets. The conventional nomenclature for the minimal basis sets is STO-xG, where x is a constant and represents the number of Gaussian primitive functions used to comprise a single basis function. One way to improve the STO-xG is to use two or three functions for each of the minimal basis functions, *i.e. double zeta* and *triple zata basis set*, respectively. Another convenient and efficient way to build a basis set is to let the valence functions doubled (or tripled) while each inner shell orbital use a single function, known as *split valence shell basis sets*. One typical example is the 6-311G basis set. It implies that each of the inner core shell orbitals consists of one basis function that is a contraction of 6 primitive Gaussians; while each of the valence orbitals is composed of three basis functions, the first one composed of a contraction of 3 primitive Gaussians, the other two composed of 1

primitive Gaussian respectively. Moreover, in order to increase the accuracy of the calculations, additional functions, such as *polarization* functions ($*$) and *diffusion*($+$) functions need to be added to the basis.

B.2.2.2 Planewaves and pseudopotentials

The electron orbitals, used to express the single particle density, defined in the Kohn-Sham equations, Eq. (B.18), may be expanded in terms of a planewave basis set. Planewave basis sets are the natural choice in the case of solids that exhibit periodicity. Therefore, the electron wave functions can be written as

$$\psi_{n\mathbf{k}}(\mathbf{r}) = \sum_{\mathbf{K}} c_{n\mathbf{k}}(\mathbf{K}) e^{i(\mathbf{k}+\mathbf{K})\cdot\mathbf{r}} \tag{B.27}$$

where $\mathbf{K}$ are reciprocal lattice vectors. The number of planewaves used in the basis can be controlled by imposing an energy cut-off. Thus, for a given energy cut-off (E_{cut}) all planewaves with a kinetic-energy smaller than (E_{cut}) are included in the basis set.

Although the use of a planewave basis set is advantageous in periodic systems, the computational cost is prohibitive if we treat all electrons in a system explicitly. This problem can be circumvented by the implementation of *pseudopotentials*.[159] This approximation is based on the assumption that only valence electrons strongly participate in the bond formation. Therefore, in the pseudopotential approach, the nuclei and core electrons are described by an effective, smooth potential which is constructed in such a way to reproduce the correct effect on the remaining valence electrons. The Kohn-Sham equations are then solved only for valence electrons, thus reducing the computational cost. On the other hand, all information about the real wave function close to the nucleus is lost, making it hard to compute properties which rely on the core region.

The **projector-augmented wave** (PAW) method,[30] originally developed by Blöchl,[160] is often used as an improvement to the pseudopotentials. The PAW allows to use a computationally convenient representation of the wave function while maintaining the all-electron information available. This is achieved by describing the all-electron wave function in terms of a smooth pseudo-wave function ($\tilde{\Psi}$) in the valence region and a local basis set expansion in the core region, called the augmentation sphere, around each atom a. The true, all-electron, Kohn-Sham wave function is, thus, defined as

$$\Psi_n(\mathbf{r}) = \tilde{\Psi}_n(\mathbf{r}) + \sum_a \sum_i (\phi_i^a(\mathbf{r}) - \tilde{\phi}_i^a(\mathbf{r})) < \tilde{p}_i^a | \tilde{\Psi}_n > \tag{B.28}$$

where ϕ_i^a, $\tilde{\phi}_i^a$ are atom-dependent partial waves, and $\tilde{p}_i^a$ are some fixed projector functions. The partial waves ϕ_i^a and $\tilde{\phi}_i^a$ are the basis sets used to expand $\Psi_n(\mathbf{r})$ and $\tilde{\Psi}_n(\mathbf{r})$, respectively. ϕ_i^a are usually chosen to be the solutions of the Kohn-Sham equations for the isolated atom, and $\tilde{\phi}_i^a$ are their smooth continuation inside the augmentation spheres. The projectors, $\tilde{p}_i^a$, are functions chosen to obtain a rapid convergence of the expansion of the wave functions.

B.2.3 Dispersion interactions in DFT

Dispersion interactions are weak van der Waals interactions. This type of interaction is due to *long range* dynamical correlation effects. It arises from the instantaneous fluctuation in the charge distribution which creates instantaneous dipole moments even though the system does not possess a permanent dipole moment. Traditional DFT functionals, such as LDA, GGA, and hybrids, are incapable of modelling dispersion interactions because of their nonlocal character. Therefore, dispersion corrected DFT functionals are good practical alternatives to conventional wave function methods. One approach is the DFT-dispersion (DFT-D) method. It is based on adding an explicit dispersion term to the conventional DFT energy.

$$E_{(DFT-disp)} = E_{KS-DFT} + E_{disp} \tag{B.29}$$

In the present work, we have used the DFT-D2 method of Grimme.[133] The dispersion correction is given by an attractive semi-empirical pair potential:

$$E_{(disp)} = s_6 \sum_{\mu<\mu'} V^{PP}(Z_\mu, Z_{\mu'}, R_{\mu,\mu'}) \tag{B.30}$$

where s_6 is a global scaling factor that is specific for each exchange-correlation functional. The pair potential between two atoms (Z_1 and Z_2) separated by r_{12} is

$$V^{PP}(Z_1, Z_2, r_{12}) = -\frac{\sqrt{C_6(Z_1)C_6(Z_2)}}{r_{12}^6} f \frac{r_{12}}{R_0(Z_1) + R_0(Z_2)} \tag{B.31}$$

where C_6 and R_0 are element-specific dispersion coefficients and van der Waals radii, respectively, and

$$f(x) = \frac{1}{1 + e^{-dx}} \tag{B.32}$$

is a cut-off function.

Empirical DFT-D methods have been implemented in many computational packages because they are easy to implement and the forces required e.g. for geometry optimizations are easily computed.

B.3 Structure optimization

The principle of *ab initio* calculations is to find the electronic ground state of the system, *i.e.* a particular arrangement of atoms that corresponds to the lowest potential energy. In order to search for the optimal geometry, an iterative procedure is followed. The quantum-mechanical code performs several *ionc relaxation* steps; *i.e.*, all nuclei are displaced in appropriate directions (according to energy gradients). After each ionic step, the ground state energy of the particular arrangement is evaluated by means of self-consistent cycles of *electronic relaxation* steps. Once the difference between two consecutive energy values is lower than a specified threshold value,

the self-consistent cycle of ionic relaxations is stopped and the new positions of all atoms result in the relaxed (optimized) structure.

Several numerical algorithms are developed for finding the ground state according to the energy and its gradients.[161] One optimal search strategy is the **Conjugate-Gradient** method, which starts at an arbitrary point in a multidimensional space and evaluates the gradient of the function. The negative of the gradient vector gives the direction of the steepest descent which is followed until a minimum is reached along this line. In this method, the search direction contains information not only from the gradient at the current step, but also from the previous gradient. The procedure is repeated until the value can no longer be lowered within a given convergence threshold of the residual forces on atoms.

Appendix C

Time-dependent Density Functional Theory

C.1 Time-dependent density functional theory

As the underlying Hohenberg-Kohn theorem is only a statement about the ground state, standard DFT cannot be applied to the broad class of problems involving excited states, most notably the simulation of optical properties of an electronic system. The extension of DFT to excited states has been accomplished in the form of time-dependent DFT (TD-DFT) based on the Runge-Gross theorem,[162] a time-dependent analogue to the Hohenberg-Kohn theorem. As in the ground state, we have to assume that a potential, $v_{KS}(\mathbf{r},\mathrm{t})$, exists that reproduces the time-dependent density of the interacting system. The density of the interacting system can then be found from the time-dependent Kohn-Sham equations

$$\left(-\frac{\nabla^2}{2} + v_{KS}[\rho(\mathbf{r},t)]\right)\phi_i(\mathbf{r},t) = i\frac{\partial}{\partial t}\phi_i(\mathbf{r},t) \tag{C.1}$$

The time dependent Kohn-Sham potential takes the following form

$$v_{KS}[\rho(\mathbf{r},t)] = v_{ext}(\mathbf{r},t) + \int \frac{\rho(\mathbf{r}',t)}{|\mathbf{r}-\mathbf{r}'|}d^3\mathbf{r}' + v_{xc}[\rho(\mathbf{r},t)] \tag{C.2}$$

where the external potential, $v_{ext}(\mathbf{r},\mathrm{t})$, represents the potential the electrons experience due to the nuclear attraction and due to any field (perturbation) applied to the system, the second term is the Coulomb term, and the last term is the time-dependent exchange-correlation functional. v_{xc} is usually adopted within the adiabatic approximation.[163]

The time-dependent density is then given by the sum of the time-dependent Kohn-Sham orbitals, ϕ_i, as

$$\rho(\mathbf{r},t) = \sum_i^N |\phi_i(\mathbf{r},t)|^2 \tag{C.3}$$

C.1.1 Linear response TD-DFT

The time-dependent Kohn-Sham equation, Eq. (C.1), can be applied to essentially any time-dependent situation and can be solved in two ways: real-time propagation and linear response theory. If the time-dependent external potential is weak, as in normal spectroscopic experiments, perturbation theory can be applied and it is thus sufficient to use the *linear-response theory* through which the electronic excitation can be extracted (thus the optical absorption spectra). On the other hand, if the time-dpendent potential is strong (*e.g.*, strong laser field), the real-time propagation[164] of the system should be used to describe non-linear phenomena.

Linear response of a Kohn-Sham system: In linear response TD-DFT, the linear response of the density to the applied field is a crucial quantity. The linear response of an interacting (*real*) system (χ) can be derived from that of its corresponding non-interacting (*Kohn-Sham*) system (χ_s), whose form can be known from the general linear-response theory.[165] Therefore, the density response related properties can be extracted.

If a time-dependent field (v_{appl}(t)) is applied to an unperturbed interacting system, this will cause a change in the time-dependent density. The linear changes of the density can be found from the *density-density response function*, χ (the so-called *susceptibility*):

$$\delta\rho(\mathbf{r},t) = \int\int \chi(\mathbf{r},\mathbf{r}',t-t')\delta v_{appl}(\mathbf{r}',t)dt'd^3\mathbf{r}' \tag{C.4}$$

Equation (C.4) means that if a small change in the external potential is made at point $\mathbf{r}'$ and time t', the density-density response function ($\chi(\mathbf{r}$, $\mathbf{r}'$, t-t$'$)) tells us how the density will change at point $\mathbf{r}$ and later time t.

When the field v_{appl}(t) is applied to the unperturbed Kohn-Sham system which corresponds to the interacting system, it will cause a variation in the Kohn-Sham potential. Thus the linearized total variation of the Kohn-Sham effective potential is

$$\delta v_{eff}(\mathbf{r},t) = \delta v_{appl}(\mathbf{r},t) + \delta v_H(\mathbf{r},t) + \delta v_{xc}(\mathbf{r},t) \tag{C.5}$$

where

$$\delta v_H(\mathbf{r},t) = \int \frac{\delta\rho(\mathbf{r}',t)}{|\mathbf{r}-\mathbf{r}'|}d^3\mathbf{r}' \tag{C.6}$$

and

$$\delta v_{xc}(\mathbf{r},t) = \int f_{xc}(\mathbf{r},\mathbf{r}',t-t')\delta\rho(\mathbf{r}',t')dt'd^3\mathbf{r}' \tag{C.7}$$

The time-dependent exchange-correlation kernel, f_{xc}, is a key quantity of TD-DFT in the linear response regime. It is a functional of the corresponding ground state density,

$$f_{xc}[\rho](\mathbf{r},\mathbf{r}',t-t') = \frac{\delta v_{xc}(\mathbf{r},t)}{\delta\rho(\mathbf{r}',t')} \tag{C.8}$$

Then the linearized density variation of the Kohn-Sham system to the applied field can be calculated *via* the non-interacting Kohn-Sham response function (χ_s):

$$\delta\rho(\mathbf{r},t) = \int\int \chi_s(\mathbf{r},\mathbf{r}',t-t')\delta v_{eff}(\mathbf{r}',t)dt'd^3\mathbf{r}' \tag{C.9}$$

According to the Kohn-Sham assumption, the density response in Eq. (C.4) and Eq. (C.9) should be equal, resulting in an expression connecting χ and χ_s in real space. For convenience, the equation is transformed to the frequency representation *via* Fourier transformation:

$$\chi(\mathbf{r},\mathbf{r}',w) = \chi_s(\mathbf{r},\mathbf{r}',w) + \int\int \chi_s(\mathbf{r},\mathbf{r}_1,w)\left(\frac{1}{(|\mathbf{r}_1-\mathbf{r}_2|)} + f_{xc}(\mathbf{r}_1,\mathbf{r}_2.w)\right)\chi(\mathbf{r}_2,\mathbf{r}',w)d^3\mathbf{r}_1d^3\mathbf{r}_2 \tag{C.10}$$

Now all the terms are functionals of the ground state density. Eq. (C.10) contains the key to electronic excitations *via* TD-DFT. When the frequency of the applied field, w, matches a true transition frequency of the system, the response function χ has a pole as a function of w.

The frequency-dependent, non interacting Kohn-Sham density response function is known as:

$$\chi_s(\mathbf{r},\mathbf{r}',w) = \sum_q \left(\frac{\xi_q(\mathbf{r})\xi_q^*(\mathbf{r}')}{w-w_q+i\eta} - \frac{\xi_q^*(\mathbf{r})\xi_q(\mathbf{r}')}{w+ww_q-i\eta}\right) \tag{C.11}$$

where q is a double index (a, i) representing a transition from an occupied Kohn-Sham orbital (ϕ_i) to an unoccupied Kohn-Sham orbital (ϕ_a); w_q is a transition energy which is equal to the difference of the Kohn-Sham orbital energies

$$w_q = \epsilon_a - \epsilon_i \tag{C.12}$$

and $\xi_q(\mathbf{r})$ denotes

$$\xi_q(\mathbf{r}) = \phi_i^*(\mathbf{r})\phi_a(\mathbf{r}) \tag{C.13}$$

In 1995, Casida[166] derived the essential equations to extract the exact energies of the interacting system from the density-density response function. His approach is nowadays implemented in many electronic-structure codes and is popular for calculating the optical properties of a system. Casida reformulated the calculation of the poles (the transition energies) of χ into a generalized Hermitian eigenvalue problem:

$$\Omega_{qq'}F_I = w_I^2F_I \tag{C.14}$$

where the $\Omega_{qq'}$ matrix is defined as

$$\Omega_{qq'}(w) = w_q^2 \delta_{q,q'} + 4\sqrt{w_q w_q'} K_{q,q'}(w) \tag{C.15}$$

where $q(a, i)$ and $q'(b, j)$ are double indexes: q denotes an electronic transition from an occupied Kohn-Sham orbital, ϕ_i, to an unoccupied Kohn-Sham orbital, ϕ_a, and q' denotes an electronic transition from an occupied Kohn-Sham orbital, ϕ_j, to an unoccupied Kohn-Sham orbital, ϕ_b; $K_{q,q'}$ is the frequency-dependent coupling matrix

$$K_{q,q'}(w) = \int\int \xi_q^*(\mathbf{r}) f_{HXC}(\mathbf{r}, \mathbf{r}', w) \xi_q(\mathbf{r}') d^3\mathbf{r} d^3\mathbf{r}' \tag{C.16}$$

here, $f_{Hxc}(\mathbf{r}, \mathbf{r}', \mathrm{w})$ is the response kernel including the Hartree kernel and exchange-correlation kernel,

$$f_{Hxc}(\mathbf{r}, \mathbf{r}', w) = \frac{1}{|\mathbf{r} - \mathbf{r}'|} + f_{xc}(\mathbf{r}, \mathbf{r}', w) \tag{C.17}$$

and the frequency-dependent xc kernel is given by

$$f_{xc}(\mathbf{r}, \mathbf{r}', w) = \int e^{iw(t-t')} f_{xc}(\mathbf{r}, \mathbf{r}', t - t') d(t - t') \tag{C.18}$$

The eigenvalues of Eq. (C.15) provide the excitation energies w_I and the eigenvectors can be used to obtain the oscillator strengths, f, defined in Eq. (3.6), and to assign the symmetry of each transition.

Appendix D

What is a supercontinuum light source?

A supercontinuum light source, first invented in the late 1960s by R. Alfano and S. Shapiro,[167, 168] can best be described as "broad as a lamp, bright as a laser". Bridging the gap between incandescent lamps and lasers, a supercontinuum source combines the spatial coherence and brightness properties of a laser with the ultrabroadband spectrum of a white-light incandescent bulb. Supercontinuum light is generated by focusing a high-peak-intensity laser pulse into a dielectric material, which will strongly polarize the material in such a way that the induced polarization depends *nonlinearly* on the electric field of the incident light. This nonlinear light-matter interaction is behind the transformation of the incident narrowband light into broadband radiation. Because it is produced in the guided modes of an optical fiber, the supercontinuum preserves the spatial coherence of the incident light. This results in an arbitrary-wavelength source of spatially coherent light. [169]

When light propagates through a dielectric material, it induces a polarization, P, which is a charge separation that can be quantified as a dipole moment per volume. Therefore, the interaction between the electric field of a light wave and the material strongly depends on the strength of the electric field. For light with low intensity; *i.e.*, if the amplitude of the electric field is much less than the Coulomb field of an atom, the displacement of the electrons is small and the restoring force can follow the electric-field linearly. Hence, the induced electric dipole moments are proportional to E, and the response is linear resulting in a polarization, P, of the medium described by

$$P = \epsilon_0 \chi E \tag{D.1}$$

where χ is the linear susceptibility of the medium and ϵ_0 is the electric permittivity of free space. In an isotropic material, χ is related to the refractive index n of the material:

$$n = \sqrt{1 + \chi} \tag{D.2}$$

Now, if the intensity is increased and E gets closer to the Coulomb field strength, the induced electric dipoles in the medium cannot respond linearly anymore; *i.e.*, the displacement of the electrons becomes so large that the restoring forces on the electrons are no longer proportional to their displacements, thus, higher order terms contribute to the polarization:[170]

$$P = P^{(1)} + P^{(2)} + P^{(3)} + ... = \epsilon_o \left[\chi E + \chi^{(2)} E^2 + \chi^{(3)} E^3 + ...\right] \tag{D.3}$$

where $\chi^{(n)}$ is the n-th order susceptibility of the material. In its most general form, all susceptibilities are tensors that determine the spatial direction of the polarization vector as induced by multiple field vectors applied simultaneously to the material.
The usual linear susceptibility, χ, is much greater than the other coefficients of the nonlinear terms, $\chi^{(2)}$, $\chi^{(3)}$, etc. and hence the latter contribute noticeably only at high-amplitude fields.
If we suppose that a light wave of the form

$$E = E_o \sin \omega t \tag{D.4}$$

is incident on the medium. The resulting polarization

$$P = \epsilon_0 \chi E_0 \sin \omega t + \epsilon_0 \chi^{(2)} E_0^2 \sin^2 \omega t + \epsilon_0 \chi^{(3)} E_0^3 \sin^3 \omega t + ... \tag{D.5}$$

can be rewritten as

$$P = \epsilon_0 \chi E_0 \sin \omega t + \frac{\epsilon_0 \chi^{(2)}}{2} E_0^2 (1 - \cos 2\omega t) + \frac{\epsilon_0 \chi^{(3)}}{4} E_0^3 (3 \sin \omega t - \sin 3\omega t) + ... \tag{D.6}$$

As the harmonic light wave sweeps through the medium, it creates a polarization wave, *i.e.* an undulating redistribution of charge within the material in response to the field. If only the linear term (i.e. $P^{(1)}$) were effective, the electric polarization wave would correspond to an oscillatory current following along with the incident light. The light thereafter reradiated in such a process is the usual refracted wave generally propagating with a reduced speed and having the same frequency as the incident light.[170] $P^{(1)}$ can give the Pockels effect (the linear electro-optic effect), *i.e.* the linear electro-optic effect, where the refractive index of a medium is modified in proportion to the applied electric field strength. The Pockels effect exists only in certain crystals which lack center symmetry.
The second-order nonlinear polarization, $P^{(2)}$, *i.e.* the second term in Eq. (D.6), arises from a $\chi^{(2)}$ nonlinearity. It is composed of two components that are of great interest: the first corresponds to a constant bias polarization varying as E_0^2. If an intense plane-polarized beam traverses an appropriate crystal, the presence of quadratic linearity will, in part, be manifested by a constant electric polarization of the medium. A voltage difference, proportional to the beam flux density, will accordingly appear across the crystal. This effect is known as optical rectification.[170] Another important effect that takes place when a material is subjected to an intense electric field is the Kerr effect. The material becomes birefringent, *i.e.* a change in the refractive index of the material takes place that is directly proportional to the square of

the electric field, *i.e.* the light intensity. This refractive index variation is responsible for the nonlinear optical effect of self-focusing of light, for example. The second component (according to the $\cos 2\omega t$ term) corresponds to a variation in electric polarization at twice the fundamental frequency. The reradiated light which arises from the driven oscillators also has a component at this same frequency, 2ω, and the process is termed second-harmonic generation. Now, if two or more primary beams of different frequencies propagate through the material, other effects can take place, such as sum and difference frequency conversion (frequency mixing).
In order to have a non-vanishing $\chi^{(2)}$ component, the material must not exhibit inversion symmetry.
The third-order nonlinear polarization, $\mathrm{P}^{(3)}$, arises from a $\chi^{(3)}$ nonlinearity that quantifies the strength of various related nonlinear processes such as, the nonlinear contribution to the refractive index, four-wave mixing, self-phase modulation, and third harmonic generation, depending on the involved light frequencies and phase matching conditions.
Higher orders of nonlinearity can be neglected, since their strength of susceptibility decreases as $\chi^n/\chi^{n+1} \approx 10^{12}$.

The supercontinuum light is generally generated in photonic crystal fibers that possess centrosymmetric structures, therefore the $\chi^{(2)}$ term vanishes and Eq. D.6 becomes:

$$P = P^{(1)} + P^{(3)} + ... = \epsilon_0 \chi E_0 \sin \omega t + \frac{3}{4}\epsilon_0 \chi^{(3)} E_0^3 \sin \omega t \tag{D.7}$$

We note that due to variations in the refractive index of the fiber, a lack of phase between frequencies ω and 3ω takes place and, hence, the third-harmonic of polarization term (sin 3ωt) can be neglected in Eq. (D.7).

Equation D.7 can then be reformulated as:

$$P = \epsilon_0 \left[\chi + \frac{3}{4}\chi^{(3)} E_0^2 \right] E_0 \sin(\omega t) \tag{D.8}$$

The expression in the square brackets is referred as the effective susceptibility $\chi_{eff} = \chi_L + \chi_{NL}$ and contains both linear (L) and nonlinear (NL) terms. Therefore, a nonlinear contribution is added to the total refractive index of the material in Eq. (D.2) to become

$$n(w, I) = n_0(w) + n_2 I \tag{D.9}$$

where I is the intensity of the electric field, n_0 is the linear refractive index, and n_2 is the induced nonlinear refractive index

$$n_2 = \frac{3}{4} \frac{\chi^{(3)}}{\epsilon_o c n_0^2} \tag{D.10}$$

Since the strong field of a laser beam is capable of inducing an appreciable intensity-dependent refractive index change in the medium, the medium then reacts back and inflicts a phase change on the incoming wave, resulting in *self-phase modulation* (SPM).

SPM frequency shift of a laser pulse

For an ultrashort pulse with a Gaussian shape and constant phase, the intensity at time t is given by

$$I(t) = I_0 \exp(\frac{-t^2}{\tau^2}) \tag{D.11}$$

where I_0 is the peak intensity and τ is half the pulse duration.

The electric field of the incident laser pulse propagating in z direction is expressed as:

$$E_{in}(z_0, t) = E_0(z, t)e^{i(knz - w_0 t)} + c.c. = E_0(z, t)e^{i\phi_0} \tag{D.12}$$

where k is the wavenumber and n is the refractive index of the material. As the pulse propagates in a non-linear optical medium of length L, the intensity at any one point in the medium rises and then falls as the pulse goes past. This will produce a time-varying refractive index:

$$\frac{dn(I)}{dt} = n_2 \frac{dI}{dt} = n_2 I_0 \frac{-2t}{\tau^2} \exp(\frac{-t^2}{\tau^2}) \tag{D.13}$$

This variation in the refractive index produces a shift in the instantaneous phase of the pulse:

$$\phi(t) = \omega_0(t) - \frac{2\pi}{\lambda_0} n(I)L \tag{D.14}$$

where ω_0 and λ_0 are the carrier frequency and (vacuum) wavelength of the pulse, and L is the distance the pulse has propagated. This phase shift results in a frequency shift of the pulse. Since the time derivative of the phase of a wave, ϕ(t), is simply the angular frequency of the wave, the instantaneous frequency ω(t) will be:

$$\omega(t) = \frac{d\phi(t)}{dt} = \omega_0 t - \frac{2\pi L}{\lambda_0} \frac{dn(I)}{dt} \tag{D.15}$$

and from Eq. (D.13), the instantaneous frequency becomes:

$$\omega(t) = \omega_0 + \frac{4\pi L n_2 I_0}{\lambda_0 \tau^2} \cdot t \cdot \exp\left(\frac{-t^2}{\tau^2}\right) \tag{D.16}$$

Figure D.1 shows how the instantaneous frequency is red-shifted to lower frequencies (*i.e.* longer wavelengths) in the leading edge (the left-hand wing) of a pulse and blue-shifted to higher frequencies (*i.e.* shorter wavelengths) in the trailing edge. The consequence is a broadening of the pulse spectrum resulting from the time-dependent intensity slope.[171]

For a **large spectral broadening**, one needs a strong SPM (*i.e.*, a large time derivative in the phase change). This obviously favors the use of **short pump laser pulses**. In practice, with sufficiently intense femtosecond laser pulses, a spectral broadening of 20,000 cm^{-1} (500 nm)

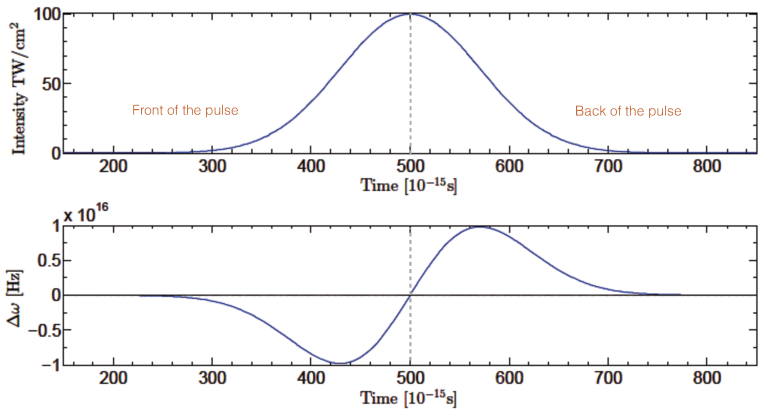

Figure D.1: Demonstration of self-phase modulation in a laser pulse. *Upper*: Time-dependent intensity profile of a Gaussian laser pulse. *Lower*: Frequency shift of the fundamental frequency ω_0 in a non-linear optical medium.[172]

is readily achievable by SPM in a condensed medium. Moreover, in order to explore the pure SPM process, one would like to keep the beam cross-section constant over the entire propagation distance in the medium. This can readily be achieved in an photonic crystal fibers.[173]

Appendix E

Basic Concepts in Solid State Systems

E.1 Basic concepts in crystallography

- **The unit cell:** A crystal is an array of atoms packed together in a regular pattern. The smallest unit that constitutes the repeating pattern is the **unit cell** of the structure. When the unit cell repeats itself to fill all of 2D or 3D space, the network is called a *lattice*. The unit cell completely defines the symmetry and structure of the entire crystal lattice, which is built by repetitive translation of the unit cell along its principle axes. Basically there are two distinctively types of unit cells in constructing the lattice: *primitive* and *non-primitive* (Figure E.1-a,b). The former consists of only one lattice point. For example, a primitive unit cell joining four lattice points, each of which counts for 1/4 shared among four unit cells. The latter, on the other hand, contains more than one lattice point per unit cell. The lengths of the principle axes, or edges, of the unit cell ($\mathbf{a}$, $\mathbf{b}$, $\mathbf{c}$) and the angles between them (α, β, γ) are the **lattice constants**, also called lattice parameters (Figure E.1-c).

- **Lattice systems - the 14 Bravais Lattices:** Lattices can be classified into "systems", each system being characterized by the shape of its associated unit cell. In three dimensions, the lattices are categorized into seven crystal systems: cubic, hexagonal, trigonal, tetragonal, orthorhombic, monoclinic, and triclinic. Each lattice is assigned to one or more of the following classifications (lattice types) based on the positions of the lattice points within the cell: primitive, body-centred, face-centred, base-centred, and rhombohedral. Altogether, there are fourteen different ways of distributing lattice points to make space lattices in a three-dimensional lattice, called the **Bravais lattices**.
  The structure of a crystal can, thus, be constructed by combining following elements: (i) the lattice type, which defines the location of the lattice points within the unit cell; (ii) the lattice parameters, that define the size and shape of the unit cell; (iii) the motif or the basis, which gives a list of atoms associated with each lattice point, along with their fractional coordinates relative to the lattice point.

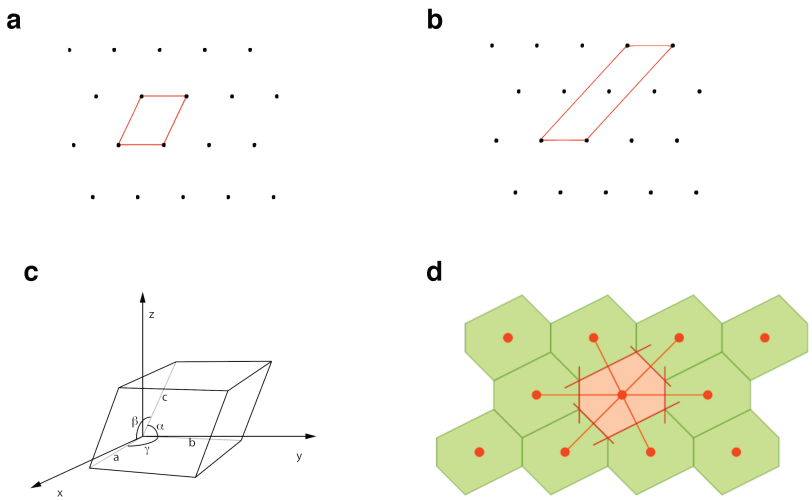

Figure E.1: The unit cell and Wigner-Seitz cell. (a) A Primitive unit cell consists of one lattice point. (b) Non-primitive unit cell consists of more than one lattice point. The lattice vectors and angles are presented in (c). (d) 2D construction of a Wigner-Seitz cell.

- **Wigner-Seitz cell and Brillouin zone:** A Wigner-Seitz cell is an example of another kind of primitive cell, since it contains only one lattice point. The cell may be chosen by first picking a lattice point. Then, lines are drawn from this point to all nearest lattice points. At the midpoint of each line, another line is drawn normal to each of the first set of lines. The smallest enclosed area (or volume) is called the Wigner-Seitz primitive cell (see Figure E.1-d). In reciprocal space, the Wigner-Seitz cell is known as the first Brillouin zone (BZ).

- **Direct and Reciprocal lattice:** A periodic structure has two lattices associated with it. The first is the real space (**direct**) lattice, and describes the periodic structure. Any real lattice vector may be expressed in terms of the lattice basis vectors as:

$$\mathbf{R} = c_1\mathbf{a} + c_2\mathbf{b} + c_3\mathbf{c} \tag{E.1}$$

where c_i are integers and $\mathbf{R}$ represents the crystal translation vector. The second is the reciprocal lattice, that determines how the periodic structure interacts with waves. The reciprocal lattice is described by a set of vectors, $\mathbf{a}^*$, $\mathbf{b}^*$, and $\mathbf{c}^*$, that are defined in terms of the direct lattice vectors as:

$$\mathbf{a}^* = 2\pi\frac{\mathbf{b}\times\mathbf{c}}{|\mathbf{a}\cdot(\mathbf{b}\times\mathbf{c})|} \quad ; \quad \mathbf{b}^* = 2\pi\frac{\mathbf{c}\times\mathbf{a}}{|\mathbf{a}\cdot(\mathbf{b}\times\mathbf{c})|} \quad ; \quad \mathbf{c}^* = 2\pi\frac{\mathbf{a}\times\mathbf{b}}{|\mathbf{a}\cdot(\mathbf{b}\times\mathbf{c})|} \tag{E.2}$$

E.1.1 The hexagonal lattice

- **Direct Lattice**

  Silicene and germanene share the same honeycomb lattice as graphene, except that they include a small buckling into their structure. To this end, we will examine the lattice of graphene and define its different lattice parameters. As shown in Figure E.2-a, the honeycomb lattice is decomposed into two sublattices marked A and B. Therefore, the unit cell (shaded area) contains two atoms, one from each sublattice.[174] The basis (lattice) vectors are defined as:

$$\vec{a}_1 = (\frac{\sqrt{3}a}{2}, \frac{a}{2}) \quad ; \quad \vec{a}_2 = (\frac{\sqrt{3}a}{2}, -\frac{a}{2}) \tag{E.3}$$

  where $a = |\vec{a}_1| = |\vec{a}_2| = \sqrt{3}a_0$ with a_0 the interatomic distance.

- **Reciprocal lattice**

  The reciprocal lattice, shown in Figure E.2-b, is also a hexagonal lattice, but rotated 90° with respect to the direct lattice. The reciprocal lattice vectors of a hexagonal lattice are:

$$\vec{b}_1 = (\frac{2\pi}{\sqrt{3}a}, \frac{2\pi}{a}) \quad ; \quad \vec{b}_2 = (\frac{2\pi}{\sqrt{3}a}, -\frac{2\pi}{a}) \tag{E.4}$$

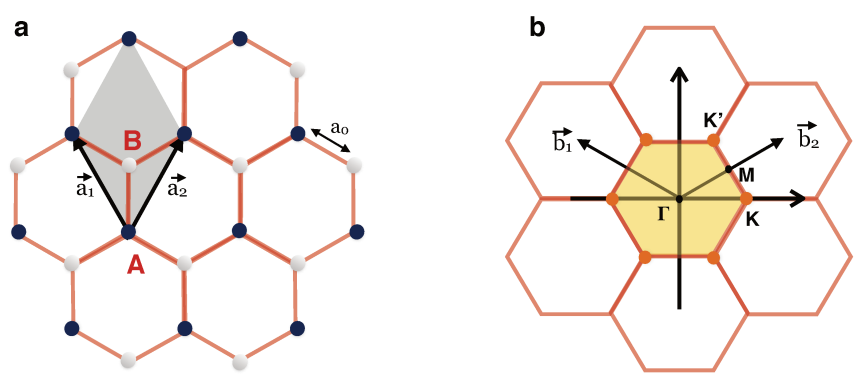

Figure E.2: Real space lattice and Brillouin zone of graphene. (a) The hexagonal lattice of graphene, with the basis vectors depicted. The shaded area represents the unit cell, (b) The reciprocal lattice of graphene. The BZ is represented by a shaded hexagon. High symmetry points are also indicated.

The first BZ, shaded hexagon in Figure E.2-b, represents a set of inequivalent points in the reciprocal space, *i.e.* points which may not be connected to one another by a reciprocal lattice vector. There are three key locations of high symmetry in the BZ. These locations are identified, by convention, as the Γ-point, M-point, and K-point, with the Γ point at the centre of the BZ.

E.2 Electrons in a periodic potential

E.2.1 The Bloch function and the band structure

In a solid system, a periodic potential appears because the ions are arranged with a periodicity of their Bravais lattice, given by the lattice vectors $\mathbf{R}$ (Eq. (E.1)):

$$U(\mathbf{r}+\mathbf{R}) = U(\mathbf{r}) \tag{E.5}$$

When this periodic potential enters into the Schrödinger equation, the translation symmetry of the periodic potential is imposed on the wave function. According to the Bloch theorem,[175] the eigenstates of the hamiltonian, $\hat{H}$, will have the form of a planewave times a function with the periodicity of the Bravais Lattice,

$$\psi_{n\mathbf{k}}(\mathbf{r}) = \exp(i\mathbf{k}\cdot\mathbf{r})u_{n\mathbf{k}}(\mathbf{r}) \tag{E.6}$$

where $\mathbf{r}$ is a position vector, $\mathbf{k}$ is a wave vector confined to the first BZ of the reciprocal lattice, and n is a discrete index called the *band index* and takes numbers n= 1, 2, 3, ... This number corresponds to the appearance of independent eigenstates of different energies, but with the same $\mathbf{k}$.

The Bloch theorem sets the stage for using planewaves as basis sets because it suggests a planewave character of the wave function. The periodic function, $u_{n\mathbf{k}}(\mathbf{r})$, is also expanded in terms of planewaves determined by wave vectors of the reciprocal lattice vectors, $\mathbf{K}$,

$$\psi_{n,\mathbf{k}+\mathbf{K}}(\mathbf{r}) = \sum_{\mathbf{K}} c_{n,\mathbf{k}+\mathbf{K}} \exp(i(\mathbf{k}+\mathbf{K})\cdot\mathbf{r}) \tag{E.7}$$

where $c_{n,\mathbf{k}+\mathbf{K}}$ are now coefficients that can be varied to determine the lowest energy solution. This also converts the Kohn-Sham equations, Eq. (B.18), from an integral to a set of algebraic equations that can readily be solved using matrix algebra.

Bloch functions, $\psi_{n\mathbf{k}}$, and their eigenvalues are periodic in $\mathbf{k}$-space, *i.e.* for a reciprocal lattice vector that does not lie in the first BZ, $\mathbf{K}$, we have

$$\psi_{n,\mathbf{k}+\mathbf{K}}(\mathbf{r}) = \psi_{n\mathbf{k}}(\mathbf{r}) \qquad ; \qquad \epsilon_{n,\mathbf{k}+\mathbf{K}} = \epsilon_{n\mathbf{k}} \tag{E.8}$$

Hence, a full set of levels can be described with $\mathbf{k}$ restricted to the first BZ. For each n, the set of electronic levels specified by $\epsilon_{n\mathbf{k}}$, is called an *energy band*. This leads to a description of energy levels of an electron in a periodic potential in terms of a family of continuous functions, $\epsilon_{n\mathbf{k}}$ or $(\epsilon_n(\mathbf{k}))$, each with the periodicity of the reciprocal lattice. The information contained in these functions is referred to as the *band structure* of the solid.[176] Moreover, the symmetry

of the lattice allows one to calculate all the possible bands by selecting a line path in the BZ (irreducible BZ). This line path includes all the important high symmetry points.

E.3 Density of states

Calculating the density of states (DOS) is another way to analyse the band structure. The DOS corresponds to the number of electronic states or unit energy within a given energy interval. It is expressed as

$$g(E) = \sum_i \delta(E - \epsilon_i) \tag{E.9}$$

where ϵ_i denote the one-electron energies. So the integral of $\psi(E)$ over an energy interval, E_1 to E_2, gives the number of one-electron states in that interval. When the δ- functions are multiplied by a weight factor that describes some property of the one-electron state ϕ_i at energy ϵ_i, various types of DOS are obtained. One example is the projected DOS (PDOS) for molecules

$$\psi_\mu(E) = \sum_i |<\chi_\mu|\phi_i>|^2 \delta(E - \epsilon_i) \tag{E.10}$$

The PDOS provides the projection of a function, χ_μ, onto the orbital ϕ_i as a weight factor for the importance of χ_μ in the orbital. In other words, with PDOS, information about the different contributions of the different orbitals is computed. One, then, knows which states (s, p, d) contribute at which energy.

E.4 Kpoint sampling

Bloch theorem eliminates the need to calculate an infinite number of wave functions, because there is only a finite number of electrons in the unit (super) cell. However, there is still an infinite number of discrete k points that must be considered, and the energy of the unit cell is calculated as an integral over these points. It turns out that wave functions at k points that are close to each other are similar, thus an interpolation scheme can be used with a *finite* number of k points. The present work employs the Monkhorst-Pack scheme,[177] which distributes the k points evenly through the first BZ, with the grid centred at the Γ point. An example of a Monkhorst-Pack grid for a hexagonal reciprocal lattice is provided in Figure E.3.

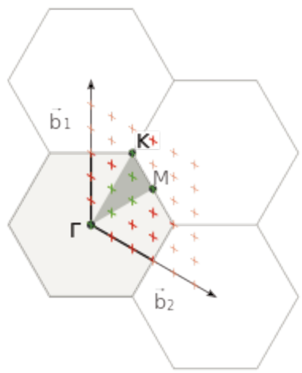

Figure E.3: Brillouin zone sampling. Example of BZ sampling of a hexagonal lattice with a Γ-centred 6×6×1 Monkhorst-Pack grid, the first BZ is highlighted in light grey and the irreducible BZ in dark grey, which is the first BZ reduced by all of the point symmetries of the lattice.

E.5 Periodic boundary conditions

Real systems contain enormous number of atoms (10^{23} atoms). However, in *ab initio* simulations, and even with powerful computational resources, the size of a system is limited to (∼300 atoms). The usual way to overcome this problem is to approximate an infinite system using a finite number of species and imposing periodic boundary conditions (PBC). In this scheme, a cubic simulation box containing the particles is replicated throughout space to form an infinite lattice. This is illustrated in the 2D case in Figure E.4. As shown, particles in each box move identically to their corresponding images in other boxes, and whenever a particle moves out of the main box (box with thick black border), one of its periodic replicas from a neighboring box moves in from the other side to replace it.

The slab model:
Depending on the type of the system under study, different PBC are applied to the simulation cell, PBC in: 1D for nanowires, in 2D for surfaces, or 3D for crystals. In order to model surfaces, for instance, one uses a slab model as shown in Figure E.5. The slab model is composed of few atomic layers, parallel to a (hkl) crystalline plane of interest, and periodic in two directions, say in x and y directions where PBC are imposed. A thick vacuum zone is applied in the third direction, to model a surface. In this way, fictitious interactions between adjacent slabs are negligible.

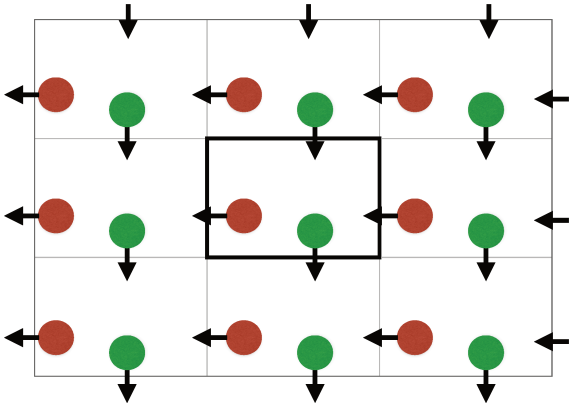

Figure E.4: 2D representation of PBC with the simulation box in bold.

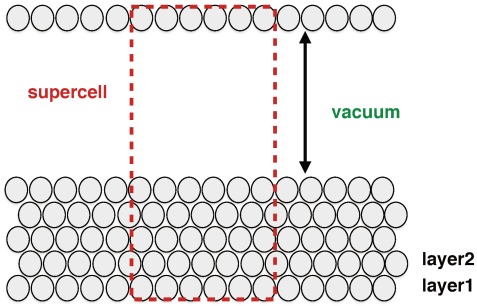

Figure E.5: Schematic representation of a slab model. Side view of a supercell which contains the layers of substrate atoms and a sufficiently large vacuum space.

Appendix F

Experimental Techniques

F.1 Scanning tunneling microscopy/spectroscopy

The field of nanotechnology was boosted in 1981 when the scanning tunneling microscope (STM) was invented with which researchers are capable of observing atoms. The STM was developed by Binning and Rohrer[178] at IBM laboratories in Zurich, for which they were awarded the Nobel Prize in Physics. The STM is a powerful tool for investigations not only of the topography of (semi) conducting surfaces with ultimately atomic resolution in real space, but also of the local electronic properties.

The STM is a non-optical microscope whose operation is based on quantum mechanical principles (see Figure F.1). A very sharp metallic tip is positioned over the specimen under study at a distance of the diameter of an atom (typically 5-10), and a bias voltage (V_{bias}) is applied between them. Depending on the characteristics of that voltage, the electrons can jump from one side to the other by a tunneling effect, producing a weak current flow, known as "tunneling current", whose value is approximately a few picoAmperes. Therefore, when the tip scans the surface along the X and Y directions, raising and lowering it by a piezoelectric mechanism to control its level, the tunneling current is measured at each point of the digital XY matrix.

The tunneling current decays exponentially with the distance gap z and is strongly affected by the density of states of the sample at the Fermi level, $\rho_s(E_F)$:

$$I \propto V_{bias}\rho_s(E_F)\exp\left[-2\frac{\sqrt{2m(\phi-E)}z}{\hbar}\right] \tag{F.1}$$

where m is the mass of the electron and ϕ is the workfunction.

The STM can be operated in two different modes: (1) constant current mode and (2) constant height mode as shown in Figure F.1-c,d. In the former case, the tip is scanned over the surface, while the feedback loop controls the height of the tip to maintain a constant tunneling current value. The recording of the feedback signal (vertical displacement of the scanner) as a function of the tip lateral position results in a map of the surface topography. The constant current mode

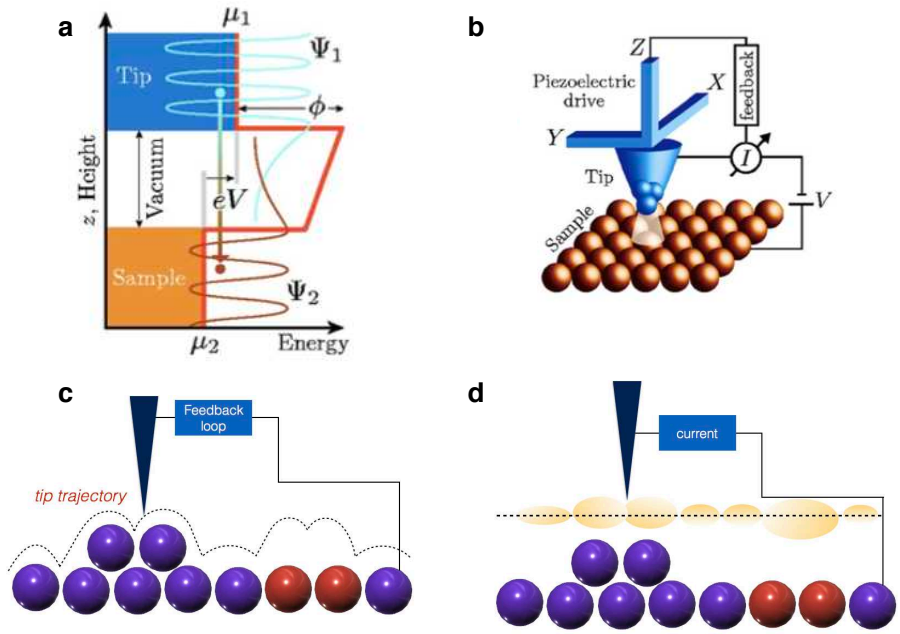

Figure F.1: Schematic illustration of scanning tunneling microscopy. (a) Tunneling process between the tip and sample across a vacuum barrier. The electron wave functions Ψ decay exponentially into vacuum with a small overlap, allowing electrons to tunnel from one electrode to the other. With a positive bias voltage applied to the sample, electrons tunnel preferentially from the tip into unoccupied sample states. (b) Schematic view of the STM.[179] (c) Tunneling in the constant-current mode. The dotted line shows the path followed by the STM tip. Notice that the substituted atoms shown in red exhibit a different apparent height to the purple surface atoms due to their different local density of states. (d) STM tip operating in the constant-height mode. The tip maintains a constant height over the surface and records the current, shown by a yellow glow.

is the most frequently used method in STM imaging because it allows probing surfaces which are not necessarily atomically flat. Alternatively, in the latter case, the tip is scanned across the surface at nearly constant height or constant vertical position from the surface. The variation of the tunneling current, depending on the topography and local electronic surface properties of the sample, is recorded as function of the tip position. However, this mode is limited to relatively flat surfaces, otherwise the tip might touch surface steps or impurities.

The second power of the STM is the ability to perform local spectroscopy. Scanning tunneling spectroscopy (STS) is able to probe the density of states (DOS) as a function of energy. The main method used here is the measurement of changes in current as a function of applied voltage with the tip held at a constant height. Since dI/dV is proportional to the DOS of the sample, ρ, the derivative of this curve corresponds to the LDOS.

$$dI/dV \propto \rho_s(E_F - eV) \tag{F.2}$$

F.2 Atomic force microscopy

The atomic force microscope (AFM) results from a development of the STM, intended to extend the possibilities of STM to insulating samples. In 1986, Binning *et al.* replaced the electron tunneling from a fine tip of the STM by the cantilever approach of the AFM. An AFM uses a cantilever with a very sharp tip to scan over a sample surface (see Figure F.2). As the tip approaches the surface, the close-range, attractive force between the surface and the tip causes the cantilever to deflect toward the surface. However, as the cantilever is brought even closer to the surface, an increasingly repulsive force takes over and causes the cantilever to deflect away from the surface. A laser beam is used to detect the cantilever deflections towards or away from the surface. By reflecting an incident beam off the flat top of the cantilever, any cantilever deflection will cause slight changes in the direction of the reflected beam. A position-sensitive photo diode array can be used to track these changes. By using a feedback loop to control the height of the tip above the surface, the AFM can generate an accurate topographic map of the surface features even for insulating samples.

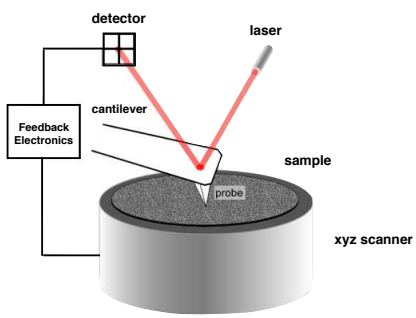

Figure F.2: Schematic illustration of atomic force microscopy.

F.3 X-ray photoelectron spectroscopy

X-ray photoelectron spectroscopy (XPS) is a widely used quantitative spectroscopic technique to determine elemental composition, as well as chemical and electronic states of the elements in a sample.[137] The principle of XPS is based on the photoelectric effect. The XPS spectra are obtained by irradiating a sample surface with a beam of X-rays. The X-ray photon energy, produced either by an X-ray source such as Mg Kα (1253.6 eV) and Al Kα (1486.6 eV) or from a synchrotron radiation light source, is transferred to a core-level electron. If this energy is higher than the electron binding energy, the electron will be ejected from the atom (see Figure F.3). Once ejected, the photoelectron will travel with a certain velocity, and therefore will have a certain kinetic energy which can be determined via the following equation:

$$E_B = h\nu - E_{kin} - \Phi_s \tag{F.3}$$

where $h\nu$ is the energy of an incoming photon, E_B is the binding energy of the electron in its initial state, E_{kin} is the kinetic energy of the photoelectron that is measured, and Φ_s is the sample work function. Knowing the frequency of radiation used in the experiment, the kinetic energy of the photoelectrons, and the sample work function, the binding energies can be calculated. The binding energy of the electron depends on the chemical structure and chemical composition of a sample.

The detector in the spectrometer determines the relative number of photoelectrons with a particular kinetic energy, known as photoelectron count. The spectrometer then generates a spectrum that expresses the photoelectron count as a function of binding energy. Based on the analysis of a peak at a particular energy in the XPS spectrum, quantitative and qualitative information on the elements present in the sample can be obtained.

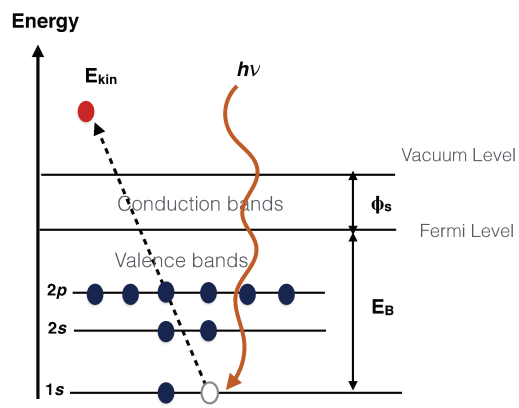

Figure F.3: Principle of Xray photoelectron spectroscopy.

Bibliography

[1] B. Haberl, T.A. Strobel, and J.E. Bradby. Pathways to exotic metastable silicon allotropes. *Appl. Phys. Rev.*, 3(4):040808, 2016.

[2] J.C. Jamieson. Crystal structures at high pressures of metallic modifications of silicon and gemanium. *Science*, 139:762–764, 1963.

[3] M.I. McMahon and R.J. Nelmes. New high-pressure phase of Si. *Phys. Rev. B*, 47:8337–8340, 1993.

[4] H. Olijnyk, S.K. Sikka, and W.B. Holzapfel. Structural phase transitions in Si and Ge under pressures up to 50 GPa. *Phys. Lett. A*, 103:137–140, 1984.

[5] M. Hanfland, U. Schwarz, K. Syassen, and K. Takemura. Crystal structure of the high-pressure phase silicon VI. *Phys. Rev. Lett.*, 82(6):1197–1200, 1999.

[6] S.J. Duclos, Y.K. Vohra, and A.L. Ruoff. Experimental study of the crystal stability and equation of state of Si to 248 GPa. *Phys. Rev. B*, 41:12021, 1990.

[7] S. Wippermann, Y. He, M. Vörös, and G. Galli. Novel silicon phases and nanostructures for solar energy conversion. *Appl. Phys. Rev.*, 3:040807, 2016.

[8] R. West, M.J. Fink, and J. Michl. Tetramesityldisilene, a stable compound containing a silicon-silicon double bond. *Science*, 214:1343–1344, 1981.

[9] M. Kira and T. Iwamoto. Progress in the chemistry of stable disilenes. *Adv. Organomet. Chem.*, 54:73, 2006.

[10] A. Sekiguchi, R. Kinjo, and M. Ichinohe. A stable compound containing a silicon-silicon triple bond. *Science*, 305(5691):1755–1757, 2004.

[11] A. Kekulé. Sur la constitution des substances aromatique. *Bull. Soc. Chim.*, 3:98, 1865.

[12] A. Kekulé. Note sur quelques produits de substitution de la benzine. *Bull. Acad. Roy. Belg*, 119:551, 1865.

[13] A. Kekulé. Untersuchungen uber aromatische verbindungen. *Ann. Chem.*, 137:129, 1865.

[14] E. Hückel. Quantum-theoretical contributions to the benzene problem. I. the electron configuration of benzene and related compounds. *Z. Physik*, 70: 204, 1931.

[15] E. Hückel. Quantum theoretical contributions to the problem of aromatic and non-saturated compounds. *Z. Physik*, 76:628, 1932.

[16] T. Iwamoto, D. Tsushima, E. Kwon, S. Ishida, and H. Isobe. Persilastaffanes: Design, synthesis, structure, and conjugation between silicon cages. *Angew. Chem., Int. Ed.*, 51:2340–2344, 2012.

[17] A.I. Boldyrev and L.-S. Wang. Beyond organic chemistry: Aromaticity in atomic clusters. *Phys. Ch.em. Chem. Phys.*, 18:11589–11605, 2016.

[18] K. Abersfelder, A.J.P. White, H.S. Rzepa, and D. Scheschkewitz. A tricyclic aromatic isomer of hexasilabenzene. *Science*, 327(5965):564–566, 2010.

[19] H. Vach. Electron-deficiency aromaticity in silicon nanoclusters. *J. Chem. Theory Comput.*, 8(6):2088–2094, 2012.

[20] J.T. Okada, P.H.-L Sit, Y. Watanabe, Y.J. Wand, B. Barbiellini, T. Ishikawa, M. Itou, Y. Sakurai, A. Bansil, R. Ishikawa, M. Hamaishi, T. Masaki, P.-F. Paradis, K. Kimura, T. Ishikawa, and S. Nanao. Persistence of covalent bonding in liquid silicon probed by inelastic x-ray scattering. *Phys. Rev. Lett.*, 108:067402, 2012.

[21] H. Vach and Q. Brulin. Controlled growth of silicon nanocrystals in a plasma reactor. *Phys. Rev. Lett.*, 95:165502, 2005.

[22] H. Vach. Ultrasrable silicon nanocrystals due to electron delocalization. *Nano Lett.*, 11(12):5477–5481, 2011.

[23] H. Vach, Q. Brulin, N. Chaabane, T. Novikova, P. Roca i Cabarrocas, B. Kalache, K. Hassouni, S. Botti, and L. Reining. Growth dynamics of hydrogenated silicon nanoparticles under realistic conditions of a plasma reactor. *Comput. Mater. Sci.*, 35(3):216–222, 2006.

[24] P. Roca i Cabarrocas, A. Fontcuberta i Morral, and Y. Poissant. Growth and optoelectronic properties of polymorphous silicon thin films. *Thin Solid Films*, 403-404:39–46, 2002.

[25] Y. Poissant, P. Chatterjee, and P. Roca i Cabarrocas. Analysis and optimization of the performance of polymorphous silicon solar cells: experimental characterization and computer modeling. *J. Appl. Phys.*, 94(11):7305–7316, 2003.

[26] L. Boufendi, M.Ch. Jouanny, E. Kovacevic, J. Berndt, and M. Mikikian. Dusty plasma for nanotechnology. *J. Phys. D: Appl. Phys.*, 44: 174035, 2011.

[27] André Bouchoule, editor. *Dusty plasma: Physics, chemistry, and technological impact in plasma processing.* Wiley, 1999.

[28] L. Boufendi and A. Bouchoule. Particle nucleation and growth in a low-pressure argon-silane discharge. *Plasma Sources Sci. Technol.*, 3:262–267, 1994.

[29] G. Kresse and J. Furthmüller. Efficient iterative schemes for ab initio total-energy calculations using a plane-wave basis set. *Phys. Rev. B*, 54:11169, 1996.

[30] G. Kresse and D. Joubert. From ultrasoft pseudopotentials to the projector augmented-wave method. *Phys. Rev. B*, 59:1758, 1999.

[31] J.P. Perdew, K. Burke, and M. Ernzerhof. Generalized gradient approximation made simple. *Phys. Rev. Lett.*, 77:3865, 1996.

[32] M.J. Frisch, G.W. Trucks, H.B. Schlegel, G.E. Scuseria, M.A. Robb, J. R. Cheeseman, G. Scalmani, V. Barone, B. Mennucci, G.A. Petersson, H. Nakatsuji, M. Caricato, X. Li, H.P. Hratchian, A.F. Izmaylov, J. Bloino, G. Zheng, J.L. Sonnenberg, M. Hada, M. Ehara, K. Toyota, R. Fukuda, J. Hasegawa, M. Ishida, T. Nakajima, Y. Honda, O. Kitao, H. Nakai, T. Vreven, J.A. Montgomery Jr., J. E. Peralta, F. Ogliaro, M. Bearpark, J.J. Heyd, E. Brothers, K.N. Kudin, V.N. Staroverov, R. Kobayashi, J. Normand, K. Raghavachari, A. Rendell, J.C. Burant, S.S. Iyengar, J. Tomasi, M. Cossi, N. Rega, J. M. Millam, M. Klene, J.E. Knox, J. B. Cross, V. Bakken, C. Adamo, J. Jaramillo, R. Gomperts, R.E. Stratmann, O. Yazyev, A.J. Austin, R. Cammi, C. Pomelli, J. W. Ochterski, R. L. Martin, K. Morokuma, V.G. Zakrzewski, G. A. Voth, P. Salvador, J.J. Dannenberg, S. Dapprich, A.D. Daniels, Ã. Farkas, J.B. Foresman, J.V. Ortiz, J. Cioslowski, and D.J. Fox. *Gaussian 09 Revision D.01*, 2009.

[33] D. Sundholm, H. Fliegl, and R.J.F. Berger. Calculations of magnetically induced current densities: theory and applications. *Wiley Interdiscip. Rev.: Comput. Mol. Sci.*, 6:639–678, 2016.

[34] J. Jusélius, D. Sundholma, and J. Gauss. Calculation of current densities using gauge-including atomic orbitals. *J. Chem. Phys.*, 121:3952–3963, 2004.

[35] J. Gauss and H.J. Werner. NMR chemical shift calculations within local correlation methods : the giao-lmp2 approach. *Phys. Chem. Chem. Phys.*, 2:2083–2090, 2000.

[36] J. Stanton, J. Gauss, M. Harding, and P. Szalay. *CFOUR, A quantum-chemical program package.* Mainz, Germany, 2012.

[37] F. Jensen. *Introduction to Computational Chemistry.* Wiley, second edition, 2006.

[38] A.D. Becke and K.E. Edgecombe. A simple measure of electron localization in atomic and molecular systems. *J. Chem. Phys.*, 92:5397–5403, 1990.

[39] A. Savin, O. Jepsen, J. Flad, O.K. Andersen, H. Preuss, and H.G. von Schnering. Electron localization in solid-state structures of the elements – the diamond structure. *Angew. Chem., Int. Ed. Engl.*, 31:187–188, 1992.

[40] T. Lu and F. Chen. A multifunctional wavefunction analyzer. *J. Comp. Chem.*, 33:580–592, 2012.

[41] D. Sheppard, R. Terell, and G. Henkelman. Optimization methods for finding minimum energy paths. *J. Chem. Phys.*, 128:134106, 2008.

[42] H. Jónsson, G. Mills, and K.W. Jacobsen. *Classical and quantum dynamics in condensed phase simulations.* World Scientific, 1998.

[43] J. Kästner, J.M. Carr, T.W. Keal, W. Thiel, A. Wander, and P. Sherwood. Dl-find: An open-source geometry optimizer for atomistic simulations. *J. Phys. Chem. A*, 113:11856–11865, 2009.

[44] H.P. Hratchian and H.B. Schlegel. Using Hessian updating to increase the efficiency of a Hessian based Predictor-Corrector reaction path following method. *J. Chem. Theory Comput.*, 1(1):61–69, 2005.

[45] H.P. Hratchian and H.B. Schlegel. Accurate reaction paths using hessian based predictor-corrector integrator. *J. Chem. Phys.*, 120:9918–9924, 2004.

[46] P.W. Atkins and R. Friedman. *Molecular Quantum Mechanics.* Oxford University Press, 2010.

[47] H. Vach. Symmetric and irregular aromatic silicon nanoclusters. *Chem. Phys. Lett.*, 614:199–203, 2014.

[48] Q. Brulin, N. Ning, and H. Vach. Hydrogen-induced crystallization of amorphous silicon clusters in a plasma reactor. *J. Non-Cryst. Solids*, 352:1055, 2006.

[49] S. Rao, K. Mantey, J. Therrien, A. Smith, and M. Nayfeh. Molecular behavior in the vibronic and excitonic properties of hydrogenated silicon nanoparticles. *Phys. Rev. B*, 76:155316, 2007.

[50] G. Belomoin, J. Therrien, A. Smith, S. Rao, R. Twesten, S. Chaieb, M. H. Nayfeh, L. Wagner, and L. Mitas. Observation of a magic discrete family of ultrabright Si nanoparticles. *Appl. Phys. Lett.*, 80:841–843, 2002.

[51] O. Akcakir, J. Therrien, G. Belomoin, N. Barry, J.D. Muller, E. Gratton, and M. Nayfeh. Detection of luminescent single ultrasmall silicon nanoparticles using fluctuation correlation spectroscopy. *Appl. Phys. Lett.*, 76:1857–1859, 2000.

[52] S. Magill, M. Nayfeh, M. Fizari, J. Malloy, Y. Maximenko, J. Xie, and H. Yu. Enhanced UV light detection using wavelength-shifting properties of silicon nanoparticles. *Journal of Instrumentation*, 10: P05008, 2015.

[53] A.D. Zdetsis. Stabilization of large silicon fullerenes and related nanostructures through puckering and poly(oligo)merization. *Phys. Rev. B*, 80:195417, 2009.

[54] A. Puzder, A.J. Williamson, F.A. Reboredo, and G. Galli. Structural stability and optical properties of nanomaterials with reconstructed surfaces. *Phys. Rev. Lett.*, 91:157405, 2003.

[55] J.E. Northrup. Structure of Si(100)H: Dependence on the H chemical potential. *Phys. Rev. B*, 44:1419, 1991.

[56] H. Vach. Terahertz and gigahertz emission from an all-silicon nanocrystal. *Phys. Rev. Lett.*, 112:197401, 2014.

[57] S. Bulusu and X.C. Zeng. Structures and relative stability of neutral gold clusters: Aun (n=15-19). *J. Chem. Phys.*, 125:154303, 2006.

[58] P. Gruene, D.M. Rayner, B. Redlich, A.F.G. van der Meer, J.T. Lyon, G. Meijer, and A. Fielicke. Structures of neutral Au_7, Au_19, and Au_20 clusters in the gas phase. *Science*, 321:674–676, 2008.

[59] J.P.K. Doye and S.C. Hendy. On the structure of small lead clusters. *Eur. Phys. J. D.*, 22:99–107, 2003.

[60] R. Fournier, J.B.Y. Cheng, and A. Wong. Theoretical study of the structure of lithium clusters. *J. Chem. Phys.*, 119:9444–9454, 2003.

[61] N.J. Juster. Color and chemical constitution. *J. Chem. Educ.*, 39:596–601, 1962.

[62] M.A. Lieberman and A.J. Lichtenberg. *Plasma discharges and materials processing.* Wiley, second edition, 2005.

[63] G. Bruno, P. Capezzuto, and A. Madan, editors. *Plasma deposition of amorphous silicon-based materials.* Academic Press, Boston, 1995.

[64] T. Roschek. *Microcrystalline Silicon Solar cells prepared by 13.56 PECVD.* PhD thesis, Forschungszentrum Jülich in der Helmholtz-Gemeinschaft, 2003.

[65] A. Bouchoule, A. Plain, L. Boufendi, J.Ph. Blondeau, and C. Laure. Particle generation and behavior in a silane-argon low-pressure discharge under continuous or pulsed radio-frequency excitation. *J. Appl. Phys.*, 70(4):1991–2000, 1991.

[66] A.A. Fridman, L. Boufendi, T. Hbid, B.V. Potapkin, and A. Bouchoule. Dusty plasma formation: Physics and critical phenomena. theoretical approach. *J. Appl. Phys.*, 79(3):1303–1313, 1996.

[67] Ch. Hollenstein, J-L. Dorier, J. Dutta, L. Sansonnens, and A.A. Howling. Diagnostics of particle genesis and growth in RF silane plasmas by ion mass spectrometry and light scattering. *Plasma Sources Sci. Technol.*, 3:278–285, 1994.

[68] M. Mikikian, L. Couëdel, M. Cavarroc, Y. Tessier, and L. Boufendi. Dusty plasma: synthesis, structure and dynamics of a dust cloud in a plasma. *Eur. Phys. J. Appl. Phys.*, 49:13106, 2010.

[69] C.F. Bohren and D.R. Huffman. *Absorption and scattering of light by small particles.* New York: Wiley, 1983.

[70] S.E. Fiedler, A. Hese, and A.A. Ruth. Incoherent broad-band cavity-enhanced absorption spectroscopy. *Chem. Phys. Lett.*, 371:284–294, 2003.

[71] R.A. Washenfelder, A.O. Langford, H. Fuchs, and S.S. Brown. Measurement of glyoxal using an incoherent broadband cavity enhanced absorption spectrometer. *Atmos. Chem. Phys.*, 8:7779–7793, 2008.

[72] P. Debye. *Polar Molecules.* Dover, 1929.

[73] K. De Bleecker. *Modeling of the formation and behavior of the nanoparticles in dusty plasma.* PhD thesis, University of Antwerpen, Belgium, 2006.

[74] G. Viera, M. Mikikian, E. Bertran, P. Roca i Cabarrocas, and L. Boufendi. Atomic structure of the nanocrystalline si particles appearing in nanostructured si thin films produced in low-temperature radiofrequency plasmas. *J. Appl. Phys.*, 92:4684, 2002.

[75] A. Fontcuberta i Morral, R. Brenot, E.A.G. Hamers, R. Vanderhanghen, and P. Roca i Cabarrocas. In situ investigation of polymorphous silicon deposition. *J. Non-Cryst. Solids*, 266-269:48–53, 2000.

[76] S. Veprek, Z. Iqbal, and F-A. Sarott. A thermodynamic criterion of the crystalline-to-amorphous transition in silicon. *Phil. Mag. B*, 45, 1982.

[77] S.T. Ceyer. New mechanisms for chemistry at surfaces. *Science*, 249:133–139, 1990.

[78] H. Vach, N. Nguyen, Q. Timerghazin, and G.H. Peslherbe. Nonadiabatic ladder climbing during molecular collisions. *Phys. Rev. Lett.*, 97:143402, 2006.

[79] T. Nguyen, Q. Timerghazin, H. Vach, and G. H. Peslherbe. Mechanically-induced generation of highly reactive excited-state oxygen molecules in cluster-surface scattering. *J. Chem. Phys.*, 134:64305–64317, 2011.

[80] Richard P. Feynman. Plenty of Room at the Bottom. Presentation to American Physical Society, 1959.

[81] R. F. Frindt. Single crystals of MoS_2 several molecular layers thick. *J. Appl. Phys.*, 37(1):1928–1929, 1966.

[82] K.S. Novoselov, A.K. Geim, S.V. Morozov, D. Jiang, Y. Zhang, S.V. Dubonos, I.V. Grigoriev, and A.A. Firsov. Electric field effect in atomically thin carbon films. *Science*, 306(5696):666–669, 2004.

[83] S. Balendhran, S. Walia, H. Nili, J. Z. Ou, S. Zhuiykov, R. B. Kaner, and S. Sriram. Two-dimensional molybdenum trioxide and dichalcogenides. *Adv. Funct. Mater*, 23:3952–3970, 2013.

[84] Q.H. Wang, K. Kalantar-Zadeh, A. Kis, J.N. Coleman, and M.S. Strano. Electronics and optoelectronics of two-dimensional electronic and optoelectronics of two-dimensional transition metal dichalcogenides. *Nat. Nanotechnol.*, 7:699–712, 2012.

[85] Q. Tang and Z. Zhou. Graphene-analogous low-dimensional materials. *Prog. Mater. Scienc.*, 58: 1244–1315, 2013.

[86] M. Houssa, A. Dimoulas, and A. Molle. Silicene: a review of recent experimental and theoretical investigations. *J. Phys.: Condens. Matter*, 27:253002, 2015.

[87] H. Liu, A. T. Neal, Z. Zhu, Z. Luo, X. Xu, D. Tománek, and P. D. Ye. Phosphorene: An unexplored 2D semiconductor with a high hole mobility. *ACS Nano*, 8(4):4033–4041, 2014.

[88] A. Acun, L. Zhang, P. Bampoulis, M. Farmanbar, A. van Houselt, A. N. Rudenko, M. Lingenfelder, G. Brocks, B. Poelsema, M.I. Katsnelson, and H.J.W. Zandvliet. Germanene: the germanium analogue of graphene. *J. Phys.: Condens. Matter*, 27: 443002, 2015.

[89] F-F. Zhu, W-J. Chen, Y. Xu, C-L. Gao, D-D. Guan, C-H. Liu, D. Qian, S-C. Zhang, and J-F. Jia. Epitaxial growth of two-dimensional stanene. *Nat. Mater.*, 14:1020–1025, 2015.

[90] K. S. Novoselov, A. Mishchenko, A. Carvalho, and A. H. Castro Neto. 2D materials and van der Waals heterostructures. *Science*, 353:461, 2016.

[91] S. Das, J.A. Robinson, M. Dubey, H. Terrones, and M. Terrones. Beyond graphene: Progress in novel two-dimensional materials and van der Waals solids. *Annu. Rev. Mater. Res.*, 45:1–27, 2015.

[92] H. Gleiter. Nanostructured materials: Basic concepts and microstructure. *Acta Mater.*, 48:1–29, 2000.

[93] V.V. Pokropivny and V.V. Skorokhod. Classification of nanostructures by dimensionality and concept of surface forms engineering in nanomaterial science. *Mater. Sci. Eng., C*, 27(990–993), 2007.

[94] L. D. Landau. Zur theorie der phasenumwandlungen II. *Phys. Z. Sowjetunion*, 11:26–35, 1937.

[95] R.E. Peierls. Quelques proprietes typiques des corpses solides. *Ann. I. H. Poincare*, 5:177–222, 1935.

[96] N.D. Mermin. Crystalline order in two dimensions. *Phys. Rev.*, 176:250–254, 1968.

[97] J.A. Venables, G.D.T. Spiller, and M. Hanbucken. Nucleation and growth of thin films. *Rep. Prog. Phys.*, 47:399–459, 1984.

[98] K. I. Bolotin, K. J. Sikes, Z. Jiang, M. Klima, G. Fudenberg, J. Hone, P. Kim, and H. L. Stormer. Ultrahigh electron mobility in suspended graphene. *Solid State Commun.*, 146:351–355, 2008.

[99] S.J. Zhang, S.S. Lin, X.Q. Li, X.Y. Liu, H.A. Wu, W.L. Xu, P. Wang, Z.Q. Wu, H.K. Zhong, and Z.J. Xu. Opening the band gap of graphene through silicon doping for the improved performance of graphene GaAs heterojunction solar cells. *Nanoscale*, 8:226–232, 2016.

[100] H. Zhang, E. Bekyarova, J-W. Huang, Z. Zhao, W. Bao, F. Wang, R.C. Haddon, and C.N. Lau. Aryl functionalization as a route to band gap engineering in single layer graphene devices. *Nano Lett.*, 11: 4047–4051, 2011.

[101] S.Y. Zhou, G-H. Gweon, A.V. Fedorov, P.N. First, W.A. de Heer, D-H. Lee, F. Guinea, A.H. Castro Neto, and A.Lanzara. Substrate-induced bandgap opening in epitaxial graphene. *Nat. Mater.*, 6:770–775, 2007.

[102] P. Miro, M. Audiffred, and T. Heine. An atlas of two-dimensional materials. *Chem. Soc. Rev.*, 43:6537, 2014.

[103] B. K. Teo and X.H. Sun. Silicon-based low-dimensional nanomaterials and nanodevices. *Chem. Rev.*, 107:1454–1532, 2007.

[104] L.C. Lew Yan Voon and G.G. Guzman-Verri. Is silicene the next graphene? *arXiv:1404.5691 [cond-mat.mtrl-sci]*, 2014.

[105] P. Vogt, P. De Padova, C. Quaresima, J. Avila, E. Frantzeskakis, M.C. Asensio, A. Resta, B. Ealet, and G. Le Lay. Silicene: Compelling experimental evidence for graphenelike two-dimensional silicon. *Phys. Rev. Lett.*, 108:155501, 2012.

[106] K. Takeda and K. Shiraishi. Theoretical possibility of stage corrugation in Si and Ge analogs of graphite. *Phys. Rev. B*, 50:14916–14922, 1994.

[107] C. Leandri, G. Le Lay, B. Aufray, C. Girardeaux, J. Avila, M.E. Dávila, M.C. Asensio, C. Ottaviani, and A. Cricenti. Self-aligned silicon quantum wires on Ag (110). *Surf. Sci. Lett.*, 574:L9–L15, 2005.

[108] G.G. Guzmán-Verri and L.C. Lew Yan Voon. Electronic structure of silicon-based nanostructures. *Phys. Rev. B*, 76:075131, 2007.

[109] S. Cahangirov, M. Topsakal, E. Aktürk, H. Şahin, and S. Ciraci. Two- and one-dimensional honeycomb structures of silicon and germanium. *Phys. Rev. Lett.*, 102:236804, 2009.

[110] A. Kara, C. Léandri, M.E. Dávila, P. De Padova, B. Ealet, H. Oughaddou, B. Aufray, and G. Le Lay. Physics of silicene stripes. *J. Supercond. Novel Magn.*, 22:259–263, 2009.

[111] G. Le Lay, B. Aufray, C. Léandri, H. Oughaddou, J-P. Biberian, P. De Padova, M.E. Dávila, B. Ealet, and A. Kara. Physics and chemistry of silicene nanoribbons. *Appl. Surf. Sci.*, 256:524–529, 2009.

[112] P. De Padova, C. Quaresima, C. Ottaviani, P. M. Sheverdyaeva, P. Moras, and C. Carbone. Evidence of graphene-like electronic signature in silicene nanoribbons. *Appl. Phys. Lett.*, 96:183102, 2010.

[113] M. Houssa, E. Scalise, K. Sankaran, G. Pourtois, V.V. Afanas'ev, and A. Stesmans. Electronic properties of hydrogenated silicene and germanene. *Appl. Phys. Lett.*, 98:223107, 2011.

[114] Z. Ni, Q. Liu, K. Tang, J. Zheng, J. Zhou, R. Qin, Z. Gao, D. Yu, , and J. Lu. Tunable bandgap in silicene and germanene. *Nano Lett.*, 12:113–118, 2012.

[115] C-C. Liu, W. Feng, and Y. Yao. Quantum spin hall effect in silicene and two-dimensional germanium. *Phys. Rev. Lett.*, 107:076802, 2011.

[116] B. Lalmi, H. Oughaddou, H. Enriquez, A. Kara, S. Vizzini, B. Ealet, and B. Aufray. Epitaxial growth of a silicene sheet. *Appl. Phys. Lett.*, 97:223109, 2010.

[117] B. Feng, Z. Ding, S. Meng, Y. Yao, X. He, P. Cheng, L. Chen, and K. Wu. Evidence of silicene in honeycomb structures of silicon on Ag(111). *Nano Lett.*, 12:3507–3511, 2012.

[118] C-L Lin, R. Arafune, K. Kawahara, N. Tsukahara, E. Minamitani, Y. Kim, N. Takagi, and M. Kawai. Structure of silicene grown on Ag(111). *Appl. Phys. Express*, 5:045802, 2012.

[119] A. Fleurence, R. Friedlein, T. Ozaki, H. Kawai, Y. Wang, and Y. Yamada-Takamura. Experimental evidence for epitaxial silicene on diboride thin films. *Phys. Rev. Lett.*, 108:245501, 2012.

[120] L. Meng, Y. Wang, L. Zhang, S. Du, R. Wu, L. Li, Y. Zhang, G. Li, H. Zhou, W. A. Hofer, and H-J Gao. Buckled silicene formation on Ir(111). *Nano Lett.*, 13:685–690, 2013.

[121] L. Li, S-Z. Lu, J. Pan, Z. Qin, Y. Wang, Y-Q. Wang, G-Y. Cao, S. Du, and H-J. Gao. Buckled germanene formation on Pt(111). *Adv. Mater.*, 26:4820, 2014.

[122] M.E. Dávila, L. Xian, S. Cahangirov, A. Rubio, and G. Le Lay. Germanene: a novel two-dimensional germanium allotrope akin to graphene and silicene. *New J. Phys.*, 16:095002, 2014.

[123] P. Bampoulis, L. Zhang, A. Safaei, R. van Gastel, B. Poelsema, and H.J.W. Zandvliet. Germanene termination of Ge_2Pt crystals on Ge(110). *J. Phys.: Condens. Matter*, 26:442001, 2014.

[124] M. Derivaz, D. Dentel, R. Stephan, M-C. Hanf, A. Mehdaoui, P. Sonnet, and C. Pirri. Continuous germanene layer on Al(111). *Nano Lett.*, 15:2510, 2015.

[125] S. Cahangirov, M. Audiffred, P. Tang, A. Iacomino, W. Duan, G. Merino, and A. Rubio. Electronic structure of silicene on Ag(111): Strong hybridization effects. *Phys. Rev. B*, 88:035432, 2013.

[126] P. Gori, O. Pulci, F. Ronci, S. Colonna, and F. Bechstedt. Origin of Dirac-cone-like features in silicon structures on Ag(111) and Ag(110). *J. Appl. Phys.*, 114:113710, 2013.

[127] Z-X. Guo, S. Furuya, J. Iwata, and A. Oshiyama. Absence and presence of Dirac electrons in silicene on substrates. *Phys. Rev. B*, 87:235435, 2013.

[128] G. Prévot, R. Bernard, H. Cruguel, and Y. Borensztein. Monitoring Si growth on Ag(111) with scanning tunneling microscopy reveals that silicene structure involves silver atoms. *Appl. Phys. Lett.*, 105: 213106, 2014.

[129] M. Satta, S. Colonna, R. Flammini, A. Cricenti, and F. Ronci. Silicon reactivity at the Ag(111) surface. *Phys. Rev. Lett.*, 115:026102, 2015.

[130] F. Ronci, G. Serrano, P. Gori, A. Cricenti, and S. Colonna. Silicon-induced faceting at the Ag(110) surface. *Phys. Rev. B*, 89:115437, 2014.

[131] L. Zhang, P. Bampoulis, A.N. Rudenko, A. van Houselt Q. Yao, B. Poelsema, M.I. Katsnelson, and H.J.W. Zandvliet. Structural and electronic properties of germanene on MoS_2. *Phys. Rev. Lett.*, 116:256804, 2016.

[132] S. Nosé. A unified formulation of the constant temperature molecular dynamics methods. *J. Chem. Phys.*, 81:511–519, 1984.

[133] S. Grimme. Semiempirical gga-type density functional constructed with a long-range dispersion correction. *J. Comp. Chem.*, 27:1787, 2006.

[134] Y. Cai, C-P. Chuu, C.M. Wei, and M.Y. Chou. Stability and electronic properties of two-dimensional silicene and germanene on graphene. *Phys. Rev. B*, 88:245408, 2013.

[135] P. Scheier, B. Marsen, M. Lonfat, W-D. Schneider, and K. Sattler. Growth of silicon nanoclusters on graphite. *Surf. Sci.*, 458:113–122, 2000.

[136] J. Sone, T. Yamagami, K. Nakatsuji, and H. Hirayama. Si growth on graphenen surfaces on 6H-SiC(0001) substrates. *Jpn. J. Appl. Phys.*, 55: 035502, 2016.

[137] M. De Crescenzi and M.N. Piancastelli. *Electron scattering and related spectroscopies*. World Scientific Publishing: Singapore, 1996.

[138] A. Koma. Van der waals epitaxy-anew growth method for a highly lattice-mismatched system. *Thin Solid Films*, 216:72–76, 1992.

[139] Y.J. Hong and T. Fukui. Controlled van der Waals heteroepitaxy of InAs nanowires on carbon honeycomb lattices. *ACS Nano*, 5(9):7576–7584, 2011.

[140] X. Li, S. Wu, S. Zhou, and Z. Zhu. Structural and electronic properties of germanene/MoS_2 monolayer and silicene/MoS_2 monolayer superlattices. *Nanoscale Res. Lett.*, 9:110, 2014.

[141] G. Wang, M. Zhang, Y. Zhu, G. Ding, D. Jiang, Q. Guo, S. Liu, X. Xie, P.K. Chu, Z. Di, and X. Wang. Direct growth of graphene film on germanium substrate. *Sci. Rep.*, 3:2465, 2013.

[142] D.H. Lee, J. Yi, J.M. Lee, S.J. Lee, Y-J. Doh, H.Y. Jeong, Z. Lee, U. Paik, J.A. Rogers, and W. Park. Engineering electronic properties of graphene by coupling with Si-rich, two-dimensional islands. *ACS Nano*, 7:301–307, 2013.

[143] H.S. Wong, C. Durkan, and N. Chandrasekhar. Tailoring the local interaction between graphene layers in graphite at the atomic scale and above using scanning tunneling microscopy. *ACS Nano*, 3(11):3455–3462, 2009.

[144] D. Chiappe, E. Scalise, E. Cinquanta, C. Grazianetti, B. van den Broek, M. Fanciulli, M. Houssa, and A. Molle. Two-dimensional Si nanosheets with local hexagonal structure on a MoS_2 surface. *Adv. Mater.*, 26:2096–2101, 2014.

[145] L. Tao, E. Cinquanta, D. Chiappe, C. Grazianetti, M. Fanciulli, M. Dubey, A. Molle, and A. Akinwande. Silicene field-effect transistors operating at room temperature. *Nat. Nanotechnol.*, 10:227–231, 2015.

[146] G. Pacchioni and J. Koutecky. Silicon and germanium clusters. a theoretical study of their electronic structures and properties. *J. Chem. Phys.*, 84:3301âĹŠ3310, 1986.

[147] R. Iftimie, P. Minary, and M.E. Tuckerman. Ab initio molecular dynamics: Concepts, recent developments, and future trends. *PNAS*, 102:6654–6659, 2005.

[148] M. Born and R. Oppenheimer. Zur quantentheorie der molekeln. *Ann. Phys.*, 84(457), 1927.

[149] P. Hohenberg and W. Kohn. Inhomogeneous electron gas. *Phys. Rev.*, 136:B864, 1964.

[150] W. Kohn and L.J. Sham. Self-consistent equations including exchange and correlation effects. *Phys. Rev.*, 140:A1133, 1965.

[151] J.P. Perdew and W. Yue. Accurate and simple density functional for the electronic exchange energy: Generalized gradient approximation. *Phys. Rev. B*, 33:8800(R), 1986.

[152] J.P. Perdew, J.A. Chevary, S.H. Vosko, K. A. Jackson, M. R. Pederson, D.J. Singh, and C. Fiolhais. Atoms, molecules, solids, and surfaces: Applications of the generalized gradient approximation for exchange and correlation. *Phys. Rev. B*, 46:6671, 1992.

[153] A.D. Becke. Density-functional exchange-energy approximation with correct asymptotic behavior. *Phys. Rev. A*, 38:3098, 1988.

[154] C. Lee, W. Yang, and R.G. Parr. Development of the colle-salvetti correlation-energy formula into a functional of the electron density. *Phys. Rev. B*, 37:785–789, 1988.

[155] J.P. Perdew. Density-functional approximation for the correlation energy of the inhomogeneous electron gas. *Phys. Rev. B*, 33:8822(R), 1986.

[156] S.H. Vosko, L. Wilk, and M. Nusair. Accurate spin-dependent electron liquid correlation energies for local spin density calculations: a critical analysis. *Can. J. Phys.*, 58:1200–1211, 1980.

[157] J.C. Slater. Atomic shielding constants. *Phys. Rev.*, 36:57, 1930.

[158] S. F. Boys. Electronic wave functions. i. a general method of calculation for the stationary states of any molecular system. *Proc. Math. Phys. Eng. Sci.*, 200: 542, 1950.

[159] J.C. Phillips and L. Kleinman. New method for calculating wave functions in crystals and molecules. *Phys. Rev.*, 116:287, 1959.

[160] P.E. Blöchl. Projector augmented-wave method. *Phys. Rev. B*, 50:17953, 1994.

[161] E. Wimmer and A.J. Freeman. *Fundamentals of the electronic structure of surfaces*, volume 2. Elsevier, Amsterdam, 2000.

[162] E. Runge and E.K.U. Gross. Density-functional theory for time-dependent systems. *Phys. Rev. Lett.*, 52:997, 1984.

[163] R. Bauernschmitt and R. Ahlrichs. Treatment of electronic excitations within the adiabatic approximation of time dependent density functional theory. *Chem. Phys. Lett.*, 256:454, 1996.

[164] A. Castro, M.A.L Marques, and A. Rubio. Propagators for the time-dependent kohn-sham equations. *J. Am. Chem. Soc.*, 77:062511, 2004.

[165] F. Nogueira, A. Rubio, K. Burke, E.K.U. Gross, M.A.L. Marques, and C.A. Ulrich. *Time-dependent density-functional theory, Lecture notes in physics*, volume 706. Springer, Berlin/Heidelberg, 2006.

[166] M.E. Casida. *Time-dependent density functional response theory of molecular systems: Theory, computational methods, and functionals*, volume 4. Elsevier Science, Amsterdam, 1996.

[167] R.R. Alfano and S.L. Shapiro. Observation of self-phase modulation and small-scale filaments in crystals and glasses. *Phys. Rev. Lett.*, 24:592, 1970.

[168] R.R. Alfano and S.L. Shapiro. Emission in the region 4000 to 7000 Å via four-photon coupling in glass. *Phys. Rev. Lett.*, 24:584, 1970.

[169] J.M. Dudley and G. Genty. Supercontinuum light. *Phys. Today*, 66:29–33, 2013.

[170] E. Heicht and A. Zajac. *Optics*. Addison-Wiseley, 1979.

[171] A. Yefet and A. Pe'er. A review of cavity design for kerr lens mode-locked solid-state lasers. *Appl. Sci.*, 3:694–724, 2013.

[172] S. Uhlig. *Self-organized surface structures with ultrafast white-light. Chapter 2: Generation of white light supercontinuum*. Springer, 2015.

[173] R.R. Alfano, editor. *The supercontinuum laser source*. Springer, second edition, 2006.

[174] H-S.P. Wong and D. Akinwande. *Carbon Nanotube and Graphene Device Physics:*. Cambridge University Press, 2010.

[175] F. Bloch. Über die quantenmechanik der elektronen in kristallgittern. *Z. Physik*, 52:555, 1929.

[176] N.W. Ashcroft and N.D. Mermin. *Solid State Physics*. Saunders College, Philadelphia, 1976.

[177] H.J. Monkhorst and J.D. Pack. Special points for brillouin-zone integrations. *Phys. Rev. B*, 13:5188, 1976.

[178] G. Binning, H. Rohrer, Ch. Gerber, and E. Weibel. Tunneling through a controllable vacuum gap. *Appl. Phys. Lett.*, 40:178, 1982.

[179] Ø. Fischer, M. Kulger, I. maggio Aprile, C. Berthod, and C. Renner. Scanning tunneling spectroscopy of high-temperature superconductors. *Rev. Mod. Phys.*, 79:353, 2007.

List of Publications

1. M. De Crescenzi, I. Berbezier, M. Scarselli, P. Castrucci, M. Abbarchi, A. Ronda, F. Jardali, J. Park, and H. Vach. "Formation of Silicene Nanosheets on Graphite."
   ACS Nano 10:11163-11171, 2016.

2. L. Persichetti, F. Jardali, H. Vach, A. Sgarlata, I. Berbezier, M. De Crescenzi, and A. Balzarotti. "Van der Waals heteroepitaxy of germanene islands on graphite."
   J. Phys. Chem. Lett. 7: 3246-3251, 2016.

   Highlighted in the March issue of the Journal of the CNRS: "Des composants électroniques en germanène : une réalité."

3. H. Vach, L. V. Ivanova, Q. K. Timerghazin, F. Jardali, H.-L. T. Le. "Metallic-like bonding in plasma-born silicon nanocrystals for nanoscale bandgap engineering."
   Nanoscale 8:18062-18069, 2016.

   Highlighted on the Back Cover page of Nanoscale, volume 8, number 42 (2016).

4. H. Vach, L. V. Ivanova, Q. K. Timerghazin, F. Jardali, H.-L. T. Le "A deeper insight into strain for the sila-bi[6]prismane $Si_{18}H_{12}$ cluster with its endohedrally trapped silicon atom, $Si_{19}H_{12}$."
   J. Comput. Chem. 36: 2089-2094, 2015.

   Highlighted on the Front Cover page of Journal of Computational Chemistry, volume 36, issue 28 (2015).

ÉCOLE DOCTORALE
INTERFACES
Approches Interdisciplinaires : Fondements, Applications et Innovation

Titre : Nouveaux matériaux exotiques nanostructurés : prévisions théoriques et vérifications expérimentales

Mots clefs : silicium, matériaux nanostructurés, aromaticité

Résumé : Cette thèse est consacrée à l'étude approfondie de formes exotiques de matériaux nano-structurés qui pourraient conduire à une avancée significative dans les nano-composants. Deux thèmes distincts ont été ainsi abordés. Dans la première partie, nous démontrons que les plasmas silane/hydrogène à basse température, proches de la formation de particules de poussière, présentent l'environnement idéal pour exploiter la tendance naturelle du silicium à la sur-coordination. Ces nano-clusters de silicium (SiNCs) qui se forment spontanément, ne possèdent pas de structure tétraédrique, sont plus stables que tous les autres SiNCs connus de cette taille et ont de fortes propriétés aromatiques dues à leur forte délocalisation électronique. Les SiNCs tétraédriques de cette taille ne peuvent absorber que dans l'ultraviolet, alors que nos calculs ont montré que des SiNCs purs, mais sur-coordonnés, absorbent dans la région spectrale ultraviolette, mais aussi dans le visible et l?infrarouge. Nous avons mesuré in situ, l'absorption de la lumière visible des SiNCs. De plus, nos mesures réalisées ont prouvées clairement que les SiNCs aromatiques possèdent un moment dipolaire permanent, que nous avons estimé entre 2 et 2,5 Debye. Dans la seconde partie, nous avons entrepris des études théoriques et expérimentales approfondies sur la croissance d'une nouvelle forme allotropique de silicium et de germanium: le silicène et le germanène. Afin d'exclure tout mélange entre les atomes de silicium ou de germanium avec le substrat et de conserver leurs caractéristiques prometteuses comme de nouveaux matériaux de Dirac, nous avons effectué nos dépôts, sur un substrat de graphite chimiquement inerte. Une de nos découvertes cruciales est que les mono-couches de silicène ou de germanène interagissent avec le substrat de graphite uniquement via des forces de van der Waals. Par conséquent, les propriétés électroniques exceptionnelles du silicène et du germanène, tels que les cônes de Dirac, sont préservées même après leur dépôt sur les surfaces de graphite.

Title : New exotic nano-structured materials: theoretical predictions and experimental verifications

Keywords : silicon, nanostructured materials, aromaticity

Abstract : This thesis is devoted to the study of advanced, exotic forms of nanostructured materials that could lead to the next big advance for nanodevices. Two distinct topics have been considered. In the first one, we demonstrate that low-temperature silane/hydrogen plasmas close to dust formation present the ideal environment to exploit the natural tendency of silicon to over-coordination for the construction of structures with electron-deficient bonds. Those silicon nanoclusters (SiNCs) form spontaneously by self assembly, do not possess tetrahedral structures, are more stable than any other known SiNC of this size, and have strong aromatic-like properties due to their high electron delocalization. Standard tetrahedral SiNCs of this size can only absorb in the ultraviolet, while our calculations have shown that pure, but over-coordinated SiNCs absorb light in the ultraviolet, visible, and infrared spectral region. Using incoherent broadband cavity enhanced absorption spectroscopy, we have measured the absorption of SiNCs and found that they do absorb light in the visible region. Our measurements have provided a clear evidence that aromatic SiNCs possess a permanent dipole moment, and it has been measured to be between 2 and 2.5 Debye. In the second part, we have undertaken in-depth theoretical and experimental studies on the growth of a new allotropic form of silicon and germanium: silicene and germanene. In order to rule out any intermixing between silicon or germanium atoms and the underneath substrate atoms, and to maintain their promising features to be new Dirac materials, we have performed our depositions on a chemically inert graphite substrate. One of our crucial findings is that the silicene or germanene monolayers interact with the graphite substrate via van der Waals forces only. Consequently, the outstanding electronic properties of silicene and germanene, such as Dirac cones, are preserved even after their deposition on the graphite surface.

Université Paris-Saclay
Espace Technologique / Immeuble Discovery
Route de l'Orme aux Merisiers RD 128 / 91190 Saint-Aubin, France